

**Ellipsometry study of the c-axis pseudogap in high temperature  
superconductors with Zn and Ni impurities**

von der Fakultät Mathematik und Physik der Universität Stuttgart  
zur Erlangung der Würde eines Doktors der Naturwissenschaften  
(Dr. rer. nat.)  
genehmigte Abhandlung

vorgelegt von

Alexei Pimenov

aus Shelkovo (Russland)

Hauptberichter: Prof. Dr. B. Keimer  
Mitberichter: Prof. Dr. C. Bechinger

Tag der mündlichen Prüfung: 24. August 2005

MAX-PLANK-INSTITUT FÜR FESTKORPERFORSCHUNG  
STUTTGART  
2005

# Zusammenfassung

Die Entdeckung der Hochtemperatur-Supraleitung in der Kupratverbindung  $La_{2-x}Ba_xCuO_4$  mit  $T_c = 35K$  durch Bednorz und Müller im Jahr 1986 war eine sehr große Überraschung. Schon im darauf folgenden Jahr wurde ihnen hierfür der Nobelpreis verliehen. In der Folge entwickelte sich eine enorme Forschungsaktivität mit dem Ziel, (i) neue Verbindungen mit noch höheren kritischen Temperaturen herzustellen, (ii) die Materialien hinsichtlich ihrer maximalen kritischen Ströme zu optimieren, und (iii) den Paarungsmechanismus der Hochtemperatur-Supraleitung zu identifizieren.

Innerhalb weniger Jahre wurde in der Tat eine große Zahl neuer Verbindungen der Kuprat-HTSL entdeckt. Der heutige Rekordwert der kritischen Temperatur wurde bereits im Jahr 1993 erreicht mit  $T_c = 135K$  in der Verbindung  $HgBa_2Cu_3O_{10+\delta}$ . Mittlerweile gibt es auch große Fortschritte in der Herstellung von Kabeln, Bändern und Drähten, die auf den Kuprat-HTSL-Materialien basieren. Hohe kritische Ströme können hier in relativ großen Magnetfeldern sowie bei Kühlung mit flüssigem Stickstoff erreicht werden.

Trotz riesiger Anstrengungen und signifikanter Verbesserungen der theoretischen und experimentellen Techniken gibt es bis zum heutigen Tag aber noch keine Übereinstimmung bezüglich des mikroskopischen Modells zum Paarungsmechanismus im supraleitenden Zustand. Im Falle der konventionellen Supraleiter wurde eine allgemein akzeptierte Theorie bereits im Jahre 1957 durch Bardeen, Cooper und Schrieffer entwickelt, die sogenannte BCS-Theorie. Der supraleitende Paarungsmechanismus basiert hier auf der Elektron-Phonon-Wechselwirkung, die zur Bildung von sogenannten Cooper-Paaren führt, deren Spin und Impuls antiparallel zueinander sind. Diese Elektronenpaare unterliegen der Bose-Statistik und können folglich in einem gemeinsamen Grundzustand kondensieren, der langreichweitige Kohärenz aufweisen kann. Im Falle der Kuprat-Hochtemperatur-Supraleiter ist die Existenz solcher Cooper-Paare ebenfalls etabliert. Die Frage

der Wechselwirkung, die der Paarbildung zugrunde liegt, bleibt aber weiterhin unbeantwortet. Es wurde bereits eine Vielzahl verschiedener Szenarien vorgeschlagen, denen entweder die Wechselwirkung mit Phononen, antiferromagnetischen Spinfluktuationen, Ladungsdichtefluktuationen oder anderen zum Teil recht exotischen Anregungen komplexer Flussphasen oder von Zuständen mit resonierenden Valenzfluktuationen zugrund liegen.

In letzter Zeit hat sich die Erkenntnis durchgesetzt, dass das Problem sogar noch komplizierter ist und einer Klärung der äußerst ungewöhnlichen elektronischen Eigenschaften im Normalzustand bedarf, die nicht im Sinne einer Fermi-Flüssigkeit schwach wechselwirkender elektronischer Quasiteilchen erklärt werden können. Der herausragende Aspekt ist hier die sogenannte Pseudo-Energielücke, die zu einer teilweisen Unterdrückung der niederenergetischen elektronischen und magnetischen Anregungen bereits im Normalzustand, also weit oberhalb der supraleitenden kritischen Temperatur führt. Wiederum wurde eine Vielzahl von Modellen zur Erklärung der Pseudo-Energielücke vorgeschlagen. Einigkeit besteht bislang aber nur im Hinblick auf die Erkenntnis, dass ein besseres Verständnis der ungewöhnlichen Eigenschaften des Normalzustandes unerlässlich ist, um den Ursprung der supraleitenden Paarwechselwirkung ergründen zu können.

Eine weitere entscheidende Frage steht in engem Zusammenhang mit der Schichtstruktur der Kuprat-Hochtemperatursupraleiter, in der die kohärente Bewegung der Ladungsträger auf die quasi-zweidimensionalen  $CuO_2$ -Ebenen beschränkt ist. Der Ladungstransport entlang der  $c$ -Achsenrichtung (senkrecht zu den metallischen und supraleitenden  $CuO_2$ -Ebenen) ist inkohärent und ähnelt eher dem eines Isolators. Es gibt in der Tat zahlreiche Spekulationen, dass diesem inkohärenten Ladungstransport entlang der  $c$ -Achsenrichtung eine entscheidende Rolle in Zusammenhang mit dem Paarungsmechanismus der Hochtemperatur-Supraleitung zukommt.

Die Infrarotspektroskopie hat wichtige Informationen über die ungewöhnlichen elektronischen Eigenschaften der Kuprat-HTSL geliefert, insbesondere bezüglich der Energieskala und der spektralen Form der supraleitenden Energielücke, dem Absolutwert der Dichte des supraleitenden Kondensates und der Stärke der Kopplung der Ladungsträger zu den verschiedenen Arten von Anregungen wie Phononen, antiferromagnetische Spinfluktuationen, etc. Weiterhin ermöglicht sie eine direkte Beobachtung der infrarot-aktiven Phononen und liefert damit wichtige Informationen über die strukturellen und elektronischen Eigenschaften dieser Materialien, insbesondere im Hinblick auf die lokale Variation der internen elektrischen Felder,

die in diesen stark anisotropen Materialien eine wichtige Rolle spielen.

Gegenstand dieser Doktorarbeit ist die Infrarot-Ellipsometrie an den Kuprat-Hochtemperatur-Supraleitern. Die Ellipsometrie ist eine moderne spektroskopische Technik, die eine direkte und besonders genaue Bestimmung der komplexen dielektrischen Funktion verschiedenster Materialien ermöglicht. Gemessen wird die Änderung des Polarisationszustandes des Lichts aufgrund der Reflektion an einer Probenoberfläche. Die signifikanten Vorteile im Vergleich mit der konventionellen Reflektionstechnik sind, dass (i) Real- und Imaginärteil der dielektrischen Funktion direkt gemessen werden, was eine Kramers-Kronig-Transformation erübrigt, und (ii) es eine selbstnormalisierende Technik ist, die keine Referenzmessungen erfordert.

In der vorliegenden Arbeit soll die  $c$ -Achsenleitfähigkeit der Kuprat-Hochtemperatur-Supraleiter im Spektralbereich des fernen und des nahen Infrarot untersucht werden. Die Themen sind (i) die Untersuchung der sogenannten Josephson-Plasmonen in der Dreifach-Schichtverbindung  $d$ -oder  $Bi_2Sr_2CaCu_3O_{10-d}$  und den damit verbundenen Phononenanomalien und (ii) der Einfluss der Substitution von nicht-magnetischen Zn- und von magnetischen Ni- Fehlstellen im Hinblick auf die Pseudoenergielücke im Normalzustand und zugrunde liegenden Korrelationen.

In Kapitel 1 werden die besonderen Aspekte und Anforderungen der Technik der Ellipsometrie vorgestellt. Die experimentellen Aufbauten werden beschrieben, insbesondere das neue Spektrometer am Infrarotstrahlrohr der ANKA-Strahlungsquelle. Die deutlich höhere Brillanz der Synchrotron-Strahlquelle ermöglicht die Durchführung von sehr genauen ellipsometrischen Messungen an vergleichsweise kleinen Proben selbst im langwelligen Spektralbereich des fernen Infrarot. Weiterhin werden auch besondere Aspekte des Laborellipsometers in Stuttgart diskutiert, das für Messungen im Spektralbereich des mittleren und nahen Infrarot optimiert wurde. In der Folge werden mehrere kritische experimentelle Aspekte und insbesondere Fehlerquellen diskutiert wie z.B. (i) Diffraktionseffekte für Messungen an kleinen Proben im fernen Infrarot, (ii) die Präparation von hochwertigen Probenoberflächen und (iii) die Qualität der optischen Komponenten wie Polarisatoren, Kompensator, Kryostatfenster oder Detektor. Kapitel 1 beinhaltet auch die wesentlichen Gleichungen, die die Beziehung zwischen den experimentell gemessenen Größen und der dielektrischen Funktion der untersuchten Materialien herstellen. Ebenfalls kurz dargestellt werden die Grundlagen der allgemeinen Theorie innerhalb des Matrixformalismus der sogenannten Jones- oder

Müller-Matrizen (1.10). Am Ende wird der Einfluss von fehlerhaften optischen Komponenten diskutiert (1.11).

Kapitel 2 gibt einen Überblick über die allgemeinen Eigenschaften der Kuprat-Hochtemperatur-Supraleiter. Einer Beschreibung der strukturellen Eigenschaften folgt eine Darstellung des Phasendiagramms der elektronischen und magnetischen Eigenschaften als Funktion der Ladungsträgerkonzentration der  $CuO_2$ -Ebenen. Insbesondere werden die optischen Eigenschaften dargestellt inklusive der ungewöhnlichen  $c$ -Achsenleitfähigkeit und der Dotierungsabhängigkeit der Pseudoenergielücke im Normalzustand (2.4). Es wird gezeigt, dass die Pseudoenergielücke im sogenannten unterdotierten Bereich des Phasendiagramms dominiert, während sie im Bereich optimaler Dotierung verschwindet und auch im überdotierten Bereich eine spektrale Energielücke nur im supraleitenden Zustand auftritt. In Bezug auf den supraleitenden Zustand konzentriert sich die Diskussion auf die Josephson-Effekte und die zugehörigen Phononenanomalien, die im Sinne einer starken Variation der lokalen elektrischen Felder verstanden werden können.

Kapitel 3 fasst die Ergebnisse der verschiedenen experimentellen Techniken zusammen, die direkte Informationen im Hinblick auf die Pseudo-Energielücke liefern, wie "angle resolved photoemission" (ARPES), "tunnelling spectroscopy", nukleare magnetische Resonanz (NMR), spezifische Wärme und Ramanspektroskopie. Es liefert auch einen Überblick über die populärsten theoretischen Modelle zur Erklärung der Pseudo-Energielücke, wie z.B. die sogenannte Streifen-theorie [135, 136], antiferromagnetische Spinfluktuationen [63], Theorien eines makroskopisch inkohärenten supraleitenden Zustandes [64], Spin-Ladungs-Separation und das Szenario eines quantenkritischen Punktes [67].

Kapitel 4 gibt eine kurze Einführung in die theoretischen Modelle zur Beschreibung von Fehlstellen, wie die sogenannte "effective mass"-Methode oder die allgemeinere "Greens function"-Methode, die eine Berechnung der durch die Fehlstellen induzierten Veränderung der elektronischen Zustandsdichte erlaubt. Es folgt ein Überblick über den Einfluss von magnetischen und nicht-magnetischen Fehlstellen auf den supraleitenden Zustand, wie er in konventionellen Supraleitern sowie in den Kuprat-Hochtemperatur-Supraleitern beobachtet wird. Besonderes Augenmerk gilt dem Einfluss der Fehlstellen auf die Pseudo-Energielücke und den

Vorhersagen der relevanten theoretischen Modelle. Im Mittelpunkt steht der Vergleich zwischen dem Verhalten der supraleitenden Energielücke und der Pseudo-Energielücke in Bezug auf die Fehlstellensubstitution. Das besondere Interesse resultiert aus der Fragestellung, ob die Pseudo-Energielücke im Normalzustand als Vorläufer der supraleitenden Energielücke (in einem makroskopisch inkohärenten Zustand) anzusehen ist oder ob ihr andere, möglicherweise sogar konkurrierende Korrelationen zugrunde liegen.

In Kapitel 5 werden die experimentellen Daten dieser Arbeit vorgestellt. Der erste Abschnitt befasst sich mit der Probenpräparation und Charakterisierung durch SQUID-Magnetometrie zur Bestimmung der supraleitenden Übergangstemperatur, EDX-Analyse zur Messung der Konzentration von Defektatomen, der thermoelektrischen Kraft zur Bestimmung der Ladungs-trägerkonzentration und Messungen der Myon-Spin-Rotation, die Aufschluss über den Verlauf der magnetischen Korrelationen liefern. Der zweite Abschnitt enthält den Hauptteil der ellipsometrischen Daten an den reinen Proben sowie an den Ni- und Zn-substituierten (Sm,Nd)(Zn,Ni)123-Kristallen. Zuerst wird der charakteristische Verlauf der Pseudo-Energielücke in den fehlerstellenfreien Proben untersucht. Hier beobachtet man eine partielle Unterdrückung der c-Achsenleitfähigkeit unterhalb einer Frequenz  $\omega_{pg}$ , welche die charakteristische Energieskala der Pseudo-Energielücke markiert. Es wird auch gezeigt, dass die Pseudo-Energielücke durch anderweitige Substitutionen außerhalb der  $CuO_2$ -Ebenen wie z.B. Y für Nd oder Sm kaum beeinflusst wird. In der Folge werden die ellipsometrischen Spektren der unterdotierten Ni-substituierten Proben im Detail vorgestellt. Aus diesen Spektren lässt sich ein starkes Anwachsen der Energieskala der Pseudo-Energielücke als Funktion der Ni-Substitution ableiten. Diese führt zu dem überraschenden Ergebnis, dass die magnetischen Ni-Fehlstellen eine komplette Unterdrückung der supraleitenden Übergangstemperatur und damit auch der supraleitenden Energielücke verursachen, während sie einen sehr positiven Einfluss auf die Pseudo-Energielücke haben, d.h. deren Energieskala ist nahezu verdoppelt. Diese Beobachtung stellt in der Tat das wichtigste experimentelle Ergebnis dieser Arbeit dar. In der Folge wird der Verlauf dieser Ni-induzierten Verstärkung der Pseudo-Energielücke als Funktion der Ladungsträgerkonzentration in den  $CuO_2$ -Ebenen untersucht. Es wird gezeigt, dass sich durch Ni eine Pseudo-Energielücke selbst in optimal dotierten Kristallen induzieren lässt, wo im reinen Fall (ohne Ni-Fehlstellen) keine Energielücke im Normalzustand beobachtet wird. Bereits für

eine leicht überdotierte Probe jedoch schwächt sich dieser Effekt der Ni-Fehlstellen deutlich ab in dem Sinne, dass die Ni-induzierte Pseudo-Energielücke nicht mehr komplett ist und ihre Energieskala steil abfällt. Das Phasendiagramm der Ni-induzierten oder Ni-verstärkten Energieskala der Pseudo-Energielücke als Funktion der Dotierung kann im Sinne des Szenarios eines quantenkritischen Punktes verstanden werden. Dieser Punkt liegt im leicht überdotierten Bereich, also innerhalb des Bereiches der supraleitenden Phase in den reinen Proben.

Ein grundlegend anderes Verhalten wird für die Kristalle beobachtet, bei denen die Supraleitung durch nicht-magnetische Zn-Fehlstellen unterdrückt wird. Offensichtlich sind die Zn-Fehlstellen nicht nur schädlich für die Supraleitung, sondern auch für die Korrelationen, die der Pseudo-Energielücke zugrunde liegen. Während die Energieskala der Pseudo-Energielücke bei sehr kleinen Zn-Konzentrationen vielleicht sogar ein wenig anwächst, nimmt sie hin zu höheren Zn-Konzentrationen (die die Supraleitung bereits völlig unterdrücken) ebenfalls merklich ab. Zusätzlich wird ein Einfüllen der Energielücke beobachtet, das im Sinne einer lokalen (also räumlich inhomogenen) Unterdrückung der Pseudo-Energielücke im Bereich der Zn-Fehlstellen verstanden werden kann. Im letzten Abschnitt wird die Bedeutung unserer experimentellen Daten im Zusammenhang mit den verschiedenen Szenarien zur Erklärung der Pseudo-Energielücke diskutiert. Insbesondere die große Ni-induzierte Verstärkung der Energieskala bei gleichzeitiger vollständiger Unterdrückung der Supraleitung ist nur schwer mit dem Szenario in Einklang zu bringen, in dem die Pseudo-Energielücke als Vorläufer der supraleitenden Energielücke in einer makroskopisch inkohärenten Phase interpretiert wird. Die magnetischen Ni-Fehlstellen wie auch die nicht magnetischen Zn-Fehlstellen innerhalb der  $CuO_2$ -Ebenen führen bekanntermaßen zu starker Potentialstreuung. Aufgrund der d-Wellensymmetrie des supraleitenden Ordnungsparameters führt diese Potentialstreuung zu destruktiven Interferenzeffekten, die zwangsläufig eine Unterdrückung des Ordnungsparameters und damit auch der zugehörigen Energielücke zur Folge haben. Die gleichen Argumente gelten auch im Falle einiger der alternativen Modelle der Pseudo-Energielücke, bei denen der zugehörige komplexe Ordnungsparameter stark anfällig für solche destruktiven Interferenzeffekte wäre wie etwa die d-Dichtewelle oder chirale Phasen. Aus unseren Daten lässt sich vielmehr ein deutlicher Hinweis darauf ableiten, dass kurz-reich-weitigen antiferromagnetischen Korrelationen eine entscheidende Rolle im Zusammenhang mit der Pseudo-Energielücke zukommt. Das wichtigste Argument betrifft den

grundlegend verschiedenen Einfluss von magnetischen Ni- und nicht-magnetischen Zn-Fehlstellen auf die Pseudo-Energielücke. Unterstützt wird diese Vermutung durch die mit der Myon-Spin-Rotation beobachtete Verstärkung der kurz-reichweitigen statischen magnetischen Korrelationen in den Ni-substituierten Proben.

Zusammenfassend lässt sich sagen, dass die vorliegende experimentelle Arbeit einen grundlegenden Unterschied zwischen der supraleitenden Energielücke und der Pseudo-Energielücke aufgedeckt hat, der einen gemeinsamen Ursprung beider Phänomene unwahrscheinlich macht. Die experimentellen Daten weisen vielmehr auf eine bedeutsame Rolle der lokalen magnetischen Korrelationen als Ursache der Pseudo-Energielücke hin. Die letztendliche Identifizierung und Spezifizierung der zugrunde liegenden Korrelationen bleibt zukünftigen Untersuchungen vorbehalten. Die Hauptaussage, die als Motivation für zukünftige Experimente dienen sollte, ist, dass der Einbau von Ni-Fehlstellen es ermöglicht, den supraleitenden Zustand vollständig zu unterdrücken, während die Pseudo-Energielücke gleichzeitig verstärkt wird (und sogar zu einer vollständigen Energielücke wird). Zukünftige Untersuchungen an solchen Ni-substituierten Proben mittels Techniken wie ARPES und STM, die räumlich aufgelöste bzw.  $k$ -Raum-aufgelöste Informationen liefern, erscheinen besonders viel versprechend. Auch weitere optische Untersuchungen an vergleichbaren Kristallen mit anderen magnetischen Fehlstellen wie Co oder Fe könnten weitere interessante Aufschlüsse über die Rolle der magnetischen Korrelationen liefern.



# Summary

The discovery by Bednorz and Müller of high temperature superconductivity in the cuprate compound  $La_{2-x}Ba_xCuO_4$  with  $T_c = 35$  K in 1986 came as a big surprise and was awarded the Nobel prize already in the following year. This discovery initiated a tremendous amount of activities towards the search for (i) new compounds with even higher critical temperatures, (ii) technological aspects and optimization of material aspects like critical currents, and (iii) the identification of the underlying interaction that gives rise to the large pairing strength. In the following years a large number of additional HTSC compounds was discovered, and the record superconductive critical temperature was raised to today's record of 135 K in the  $HgBa_2Cu_3O_{10+\delta}$  compound already back in 1993. Also, meanwhile there has been tremendous progress in the fabrication of HTSC based cables, tapes and wires that can carry high critical currents in relatively large magnetic fields by using liquid nitrogen as a coolant. Despite of the tremendous efforts and improvement in theoretical and experimental techniques to date no consensus has been reached as to origin of the superconductive pairing mechanism in the HTSC cuprates. For the conventional superconductors there exists a well accepted theory that was developed by Bardeen, Cooper and Schrieffer in 1957, the so-called BCS theory. The superconductive pairing mechanism is based here on the electron-phonon interaction which gives rise to the formation of so-called Cooper pairs that have antiparallel momentum and spin. These electron pairs obey the Bose-statistics and thus can condense in a common ground state that exhibits long range macroscopic coherence. In the case of the cuprate HTSC the presence of Cooper-pairs is meanwhile well established. However, one of the important remaining questions concerns the interaction which leads to the formation and the condensation of these Cooper-pairs. A vast number of different scenarios have been predicted which are based on phonons, anti-ferromagnetic spin-fluctuations, charge density fluctuations, and even more exotic states like

the resonance valence bond state or complex flux phases. Meanwhile it has been realized that the problem is even more complicated and starts already with the highly unusual normal state electronic properties that cannot be accounted for in terms of a Fermi-liquid type theory of weakly interacting electronic quasiparticles. The most prominent feature is the so-called pseudogap which gives rise to an incomplete suppression of the low-energy charge and spin excitations that occurs already in the normal state, i.e. well above the superconductive critical temperature. While a vast number of models have been proposed in order to account for this pseudogap phenomenon, it is still the subject of ongoing debate and controversy. General agreement has only been reached in that the understanding of this phenomenon and thus of the unusual normal state electronic properties may be a prerequisite for developing a successful theory of the superconductive pairing mechanism. Another important question concerns the unusual layered structure of the cuprate HTSC where the charge carriers are confined to the  $CuO_2$  layers. Despite the apparently metallic and superconductive transport properties along these  $CuO_2$  layer, the charge transport in the perpendicular  $c$ -axis direction is incoherent and resembles the one of an insulator. This has raised the question about the role of charge confinement for the mechanism of HTSC in the cuprates.

Among the experimental techniques, infrared spectroscopy has provided valuable information about the unusual electronic properties of the cuprate HTSC superconductors. In particular, it has yielded detailed information about the energy scale and the spectral shape of the superconductive energy gap, about the magnitude of the superconductive condensate density and about the coupling of the charge carriers to defects or various kinds of excitations like phonons, spin-fluctuations etc. In addition, it allows one to access the infrared-active phonon modes which provide valuable information about the structural and electronic properties of these materials and in particular about the local-electric field effects which appear to be rather dominant in these highly anisotropic layered materials.

This thesis reports on infrared ellipsometric studies of the dielectric properties of cuprate high temperature superconductors. Ellipsometry is an advanced spectroscopy technique that allows one to measure directly and with high precision the complex dielectric function of a given material by analyzing the change of the polarization state of light upon reflection on the sample. It has significant advantages with respect to conventional reflection techniques in that no

Kramers-Kronig transformation and related extrapolation of the experimental data to zero and infinite frequency nor reference measurements are required. The subject of the present work are studies of the *c*-axis dielectric response of the cuprate high  $T_c$  superconductors in the far- and mid-infrared spectral ranges. The main topics are (i) the investigation of the Josephson plasma resonances in the so-called three-layer compound  $Bi_2Sr_2CaCu_3O_{10-d}$  and the related phonon anomalies which can be described in term of local electric field effects and (ii) the influence of the substitution of non-magnetic Zn and magnetic Ni-impurities on the normal state pseudogap in order to obtain more information about the underlying correlations.

Chapter 1 presents details of the ellipsometry technique. It provides a description of the experimental setups with special emphasis on the new spectrometer that has been installed at the synchrotron light source at the ANKA Strahlquelle at Forschungszentrum Karlsruhe and the laboratory-based setup that has been optimized for measurements in the mid-infrared spectral range. The much higher brilliance of the synchrotron source enables accurate ellipsometric experiments even on very small samples. A discussion of several critical aspects is provided that can give rise to severe experimental errors such as (i) diffraction effects for small samples, (ii) the preparation of a high quality sample surface, and (iii) the quality of the optical elements in the setup like polarizers, compensator, cryostat windows, and detector. Chapter 1 also contains the basic equations which allow one to extract the dielectric constants from the ellipsometric data. Aspects of the more advanced, generalized theory are briefly presented in section 1.10. This description includes two matrix formalisms operating with so-called Jones and Müller matrices. Finally, the influence of non-perfect components is considered in section 1.11.

Chapter 2 provides an overview of the generic features of the HTSC. Following a description of the common structural properties the phase diagram of the HTSC is presented in terms of the evolution of the electronic and magnetic properties as a function of the hole doping of the  $CuO_2$  layers. Special emphasis is given to the infrared optical properties. The fundamentally different behavior of the electronic transport parallel and perpendicular to the metallic  $CuO_2$  layers is discussed and special emphasis is given to the very unusual response along the *c*-axis direction where a partial gap-like suppression of the conductivity occurs already in the normal state, the so-called pseudogap phenomenon. The doping

dependence of the  $c$ -axis conductivity is discussed in section 2.4. It is shown that the pseudogap persists only in the underdoped regime, while in optimally doped and overdoped samples a spectral gap develops only in the superconductive state. Concerning the superconductive state the discussion is focused on the Josephson effect and related phonon anomalies which can be accounted for in the context of a local-field-effect model.

Chapter 3 provides a summary of the different experimental observations of the pseudogap in HTSC by means of angle resolved photoemission (ARPES), tunnelling spectroscopy, nuclear magnetic resonance (NMR), specific heat, and Raman spectroscopy. It also gives an account of the basic concepts of the most popular theoretical models that have been proposed to explain the pseudogap phenomenon. These include the stripe theory [135, 136], anti-ferromagnetic spin fluctuations [63], precursor superconductive pairing scenario [64], spin charge separation scenario, and quantum critical point scenario [67].

Chapter 4 contains an outline of the general theoretical approaches for modelling impurities, like the so-called effective mass method or the more generic Green function method which allows to calculate the density of states in different systems with impurities. Following an outline of the effect of magnetic and non-magnetic impurities on the superconductive state in conventional superconductors and cuprate HTSC, the focus is put on the issue how the normal state pseudogap is affected by the defects. In particular, the expected differences between the various theoretical proposals are discussed. The main issue is whether the superconductive gap and the normal state pseudogap are affected in a similar manner by the various kinds of impurities. A very important open question that motivated part of the present thesis work is whether the pseudogap is related to some kind of a precursor superconductive state or rather needs to be described in terms of different kinds of correlations which may even be competing with the superconductive state.

In chapter 5 the main experimental results are present. The first section is dedicated to the sample preparation and characterization by means of SQUID magnetometry to determine the superconductive transition temperatures, EDX analysis to measure the impurity content, thermo-electric power measurements to determine the hole doping state and muon-spin-rotation measurements that provide information on the evolution of the magnetic correlations upon impurity substitution. The following section contains the main part of the ellipsometric

data on the pure, Ni and Zn substituted (Sm,Nd)(Zn,Ni)123 crystals. First, it is shown that in pure samples the pseudogap corresponds to a partial suppression of the  $c$ -axis conductivity below a frequency  $\omega_{pg}$  that marks the energy scale of the gap. It is also demonstrated that the pseudogap is not strongly affected by substitution of Y ion with rare earth Nd or Sm. Subsequently, the spectra of underdoped NdNi123 samples are considered in detail. These spectra establish a dramatic enhancement of the pseudogap energy scale upon substitution of magnetic Ni impurities which at the same time give rise to a complete suppression of superconductivity. This Ni induced enhancement of the pseudogap energy scale is the major result of the present thesis work. Following up on this dramatic effect the evolution of the Ni-enhanced pseudogap is shown as a function of the hole content. It is shown that the Ni substitution allows one to restore a normal state pseudogap even in optimally doped samples where it is entirely absent for the pure case. To the contrary for a slightly overdoped crystal we find only a very weak Ni-induced enhancement of the pseudogap correlations. The observed phase diagram as a function of doping is suggestive of a critical point that marks the onset of the correlations that are responsible for the pseudogap effect. Interestingly, this onset is located in the overdoped regime slightly past optimum doping, i.e. within the region of the superconductive dome. An entirely different behavior is observed for the corresponding crystals where superconductivity is suppressed by means of non-magnetic Zn impurities (instead of the magnetic Ni impurities). It appears that the Zn impurities are deleterious not only for the superconductive correlations but also for the pseudogap phenomenon, albeit superconductivity is destroyed at a much faster rate. While the energy scale of the pseudogap appears to be slightly increased at first for samples with a very low Zn content, the pseudogap energy scale decreases at higher Zn content. In addition, the gap apparently fills in and becomes less pronounced in good agreement with a spatially inhomogeneous scenario where the gap becomes fully suppressed in the vicinity of the Zn impurities while it persists in the remote areas. In the last paragraph the implications of the experimental data in the context of the various theoretical concepts are discussed. In particular, it is outlined that the apparent Ni-induced enhancement of the pseudogap energy scale, despite the strong suppression of superconductivity cannot be reconciled with models where the pseudogap has the same origin as the superconductive one. Within the various models of a precursor superconductive state it is very difficult to understand that the pseudogap energy

scale is strongly enhanced by Ni impurities which give rise to magnetic as well as potential scattering. In particular, the d-wave nature of the SC order parameter dictates that potential scattering gives rise to destructive interference effects and thus to a suppression of the characteristic gap energy scale. The same arguments apply to various alternative models that associate the pseudogap with some kind of competing state that has a complex order parameter which is prone to destructive interference effects from potential scattering such as d-density-wave state or chiral states. Finally, we discuss the evidence that short range AF correlations may play an important role in the pseudogap phenomenon. The most important argument in favor of this possibility are the drastically different response of the normal state pseudogap to magnetic Ni and non-magnetic Zn impurities as well as the enhancement of the short range AF correlations upon Ni substitution as observed by muon spin rotation measurements.

In summary, the present work provides clear evidence that the pseudogap state has a distinctively different origin than the superconductive one. Magnetic correlations apparently are playing an important role. Nevertheless, the identification of the underlying correlations has to await future experiments. The main message and motivation for future experiments might be that Ni-substitution allows one to fully suppress superconductivity while the pseudogap becomes even enhanced or restored (it actually becomes a real gap). Hopefully this will motivate future studies on heavily Ni doped samples by means of other spectroscopic techniques like ARPES and STM that can provide real space and k-space resolved information. Furthermore, optical studies of samples with other kinds of magnetic impurities like Co or Fe could be useful to learn more about the role of magnetic correlations.

# Contents

<b>Zusammenfassung</b>	<b>1</b>
<b>Summary</b>	<b>8</b>
<b>1 Ellipsometry</b>	<b>18</b>
1.1 Basic ideas . . . . .	18
1.2 Analysis of ellipsometric equations . . . . .	20
1.3 Basic setup for ellipsometry . . . . .	21
1.4 Requirements to an ellipsometer . . . . .	23
1.4.1 Assumptions of ellipsometry theory . . . . .	23
1.4.2 List of requirements . . . . .	24
1.5 Principles of Fourier-transform spectroscopy (FTS) . . . . .	24
1.6 Ellipsometry with FTS . . . . .	27
1.7 Experimental setup in MPI Stuttgart . . . . .	28
1.8 Setup in Karlsruhe. Ellipsometry with a synchrotron source . . . . .	30
1.9 Sample preparation . . . . .	31
1.10 Generalized ellipsometry . . . . .	32
1.10.1 General description of dielectric constant extraction from ellipsometric parameters . . . . .	32
1.10.2 Conclusions and summary . . . . .	40
1.11 Ellipsometry with imperfect components . . . . .	43
1.12 Leak of polarizers and depolarization of compensators . . . . .	43
1.12.1 Polarizer imperfection . . . . .	43
1.12.2 Depolarization of compensator . . . . .	43
1.12.3 Müller matrix theory with imperfections . . . . .	44
1.12.4 Method to measure polarizer imperfections using a totally depolarized source . . . . .	49

<i>CONTENTS</i>	15
1.12.5 Measurement of depolarization parameter . . . . .	51
1.13 Analysis of ellipsometric data . . . . .	53
1.13.1 Anisotropy correction . . . . .	53
1.13.2 Diffraction correction . . . . .	54
1.13.3 Properties of optical conductivity . . . . .	55
1.13.4 Drude-Lorentz model of optical conductivity . . . . .	56
1.14 Summary . . . . .	57
<b>2 Infrared properties of HTSC</b>	<b>58</b>
2.1 Introduction . . . . .	58
2.2 Structure and phase diagram of HTSC . . . . .	59
2.3 In-plane infrared properties . . . . .	63
2.4 C-axis infrared properties . . . . .	68
2.5 Josephson resonance and phonon anomalies in $Bi_2Sr_2Ca_2Cu_3O_{10}$	75
2.5.1 Introduction . . . . .	75
2.5.2 C-axis spectra of Bi2223 . . . . .	75
2.5.3 Josephson superlattice model and transverse plasmon . . .	78
2.5.4 Phonon anomalies . . . . .	80
2.5.5 Spectral weight transfer and sum rule . . . . .	82
2.5.6 Summary . . . . .	83
<b>3 Pseudogap</b>	<b>84</b>
3.1 Introduction . . . . .	84
3.2 Angle resolved photoemission . . . . .	85
3.3 Scanning tunnelling spectroscopy and microscopy . . . . .	89
3.4 Nuclear magnetic resonance NMR . . . . .	93
3.5 Raman scattering . . . . .	96
3.6 Specific heat measurements . . . . .	97
3.7 Other techniques . . . . .	99
3.7.1 Andreev reflection spectroscopy . . . . .	99
3.7.2 DC resistivity . . . . .	100
3.8 Interpretations of pseudogap . . . . .	100
<b>4 Impurities</b>	<b>103</b>
4.1 Introduction . . . . .	103
4.2 Theoretical background . . . . .	104



4.2.1	Effective mass method . . . . .	105
4.2.2	Green function method . . . . .	107
4.2.3	Some theoretical results . . . . .	108
4.3	Impurities in ordinary superconductors . . . . .	109
4.4	Magnetic and non-magnetic impurities in HTSC . . . . .	111
4.4.1	Reduction of $T_c$ . . . . .	111
4.4.2	Tunnelling spectroscopy results . . . . .	112
4.4.3	NMR results . . . . .	116
<b>5</b>	<b>Influence of impurities on the pseudogap</b>	<b>122</b>
5.1	Introduction . . . . .	122
5.2	Sample characterization by SQUID and EDX . . . . .	123
5.2.1	$T_c$ measurements by SQUID . . . . .	123
5.2.2	Measurements of impurity content by EDX . . . . .	125
5.3	Thermoelectric power measurements . . . . .	126
5.4	$\mu SR$ measurements . . . . .	128
5.4.1	Introduction to $\mu SR$ . . . . .	128
5.4.2	$\mu SR$ measurements on $Eu_{0.85}Ca_{0.15}Ba_2Cu_{3-y}(Zn, Ni)_yO_{7-\delta}$ . . . . .	130
5.5	Pure samples . . . . .	131
5.5.1	Identification of pseudogap in c-axis optical conductivity . . . . .	131
5.5.2	Effect of substitution on the rare earth site: differences between Y123 and Nd123 . . . . .	133
5.6	Pseudogap in Ni doped $(Sm, Nd)Ba_2Cu_{3-y}Ni_yO_{7-\delta}$ samples . . . . .	136
5.6.1	Introduction . . . . .	136
5.6.2	Dependence of pseudogap frequency on Ni content . . . . .	136
5.6.3	In-plane conductivity of Ni-doped samples . . . . .	138
5.6.4	Pseudogap in optimally doped and overdoped Ni substituted samples . . . . .	139
5.7	IR spectra of Zn substituted samples for different hole doping . . . . .	141
5.8	Discussion . . . . .	144
5.8.1	Discussion and Conclusions . . . . .	144
5.8.2	Precursor superconductive fluctuations and preformed Cooper pairs . . . . .	144
5.8.3	Exotic Flux-phase or density wave theories . . . . .	145
5.8.4	Anti-ferromagnetic fluctuations . . . . .	145
5.8.5	Stripe theory of pseudogap . . . . .	146

<i>CONTENTS</i>	17
5.8.6 Spin charge separation scenario . . . . .	147
5.8.7 Quantum critical point scenario . . . . .	148
5.8.8 Ideas for future projects . . . . .	148
<b>Bibliography</b>	<b>153</b>
<b>Acknowledgements</b>	<b>160</b>
<b>Copyrights and terms of use</b>	<b>162</b>

# Chapter 1

## Ellipsometry

### 1.1 Basic ideas

Optical spectroscopy is a very useful and powerful method for studying electronic and lattice vibrational properties of different kinds of materials, including crystals and films of superconducting materials like the cuprate HTSC. One specification of this class of techniques is ellipsometry which measures the change of the polarization state of light upon grazing reflection. It overcomes two major problems of conventional spectroscopy or reflectivity: the phase problem (in ellipsometry the phase is measured and does not have to be calculated by Kramers-Kronig transform) and the reference problem (ellipsometry requires relative, not absolute, intensities). Paul Drude was the first to study optical properties using the ellipsometry technique. He published the equation of ellipsometry in 1887 [1], and his experimental results in 1888 [2]. Generally, after reflection on a sample the polarization state of the light is elliptical, fig. 1.1. The electrical field components parallel and perpendicular (in German "senkrecht"),  $E_{ip}$  and  $E_{is}$ , with respect to the plane of incidence change their amplitude and phases due to reflection upon the sample. This reflection is described by two complex reflection coefficients  $r_p = |r_p|e^{i\delta_p}$  and  $r_s = |r_s|e^{i\delta_s}$ . Ellipsometry operates with the ratio of intensities of two electrical field components  $E_{ip}/E_{is} = r_p/r_s = \tan \Psi e^{i\Delta}$ , where the ellipsometric parameters  $\Psi$  and  $\Delta$  are  $\tan \Psi = |r_p|/|r_s|$ ,  $\Delta = \delta_p - \delta_s$ . On the other hand, these parameters are functions of the dielectric constants of the sample:

$$\Delta = \Delta(\varepsilon, \sigma, \omega), \tag{1.1}$$

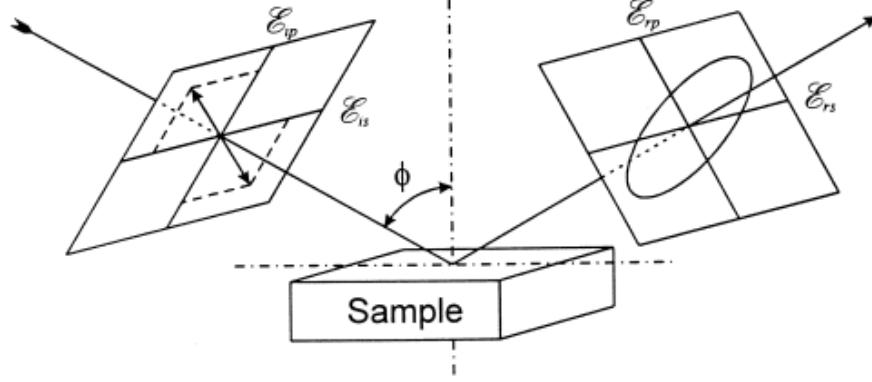


Figure 1.1: Light reflecting from a sample at angle  $\Phi$ . The linearly polarized incident light has two electric field components  $E_{ip}$  and  $E_{is}$  in the directions parallel and perpendicular to the propagation plane, respectively. The reflected light has elliptical polarization.

$$\Psi = \Psi(\varepsilon, \sigma, \omega), \quad (1.2)$$

where  $\varepsilon$  is the real part of dielectric function,  $\sigma$  is the real part of conductivity, and  $\omega$  is the frequency.

There are two equivalent descriptions: the first one operates with real and imaginary parts of the dielectric function  $\varepsilon_1, \varepsilon_2$ , the second one operates with the real part of dielectric function and the real part of the conductivity. The ratio between conductivity and dielectric function  $\sigma \propto \omega \varepsilon$  makes these descriptions equivalent.

By solving equations 1.1, 1.2 one can obtain the values of  $\varepsilon$  and  $\sigma$  at a frequency  $\omega$ . The specific form of the equations 1.1, 1.2 depends on the sample type. For the simplest case of an isotropic medium, the solution has the following form:

$$\varepsilon \propto \sin^2 \Phi \left( 1 + \frac{\tan^2 \phi (\cos^2 2\Psi - \sin^2 2\Psi \sin \Delta)}{(1 + \sin 2\Psi \cos \Delta)^2} \right), \quad (1.3)$$

$$\sigma \propto \omega \frac{\sin^2 \phi \tan^2 \phi \sin 4\Psi \sin \Delta}{(1 + \sin 2\Psi \cos \Delta)^2}, \quad (1.4)$$

$\phi$  is the angle of incidence. The coefficients of proportionality depend on the unit

system used.

## 1.2 Analysis of ellipsometric equations

According to equations 1.1, 1.2 the deduced values of the dielectric constants are very sensitive to small errors in the angle of incidence. Therefore, the surface of the sample should be rather well defined and flat, and one should use a collimated incident beam. Significant errors in the angle of incidence ultimately will lead to corresponding distortions of the deduced dielectric function. The ellipsometric parameters themselves depend on the angle of incidence  $\phi$  (see fig. 1.2). In the vicinity of the Brewster angle the ellipsometric parameters, especially  $\Delta$ , are changing most rapidly. For the ellipsometric measurements to be most sensitive and accurate one thus needs to choose an angle of incidence that is rather close to Brewster's angle of the material. Brewster's angle itself depends on the dielectric properties of the material. For example, in the far infrared it is close to 74 degree for Si and almost 90 degree for metallic or superconductive samples.

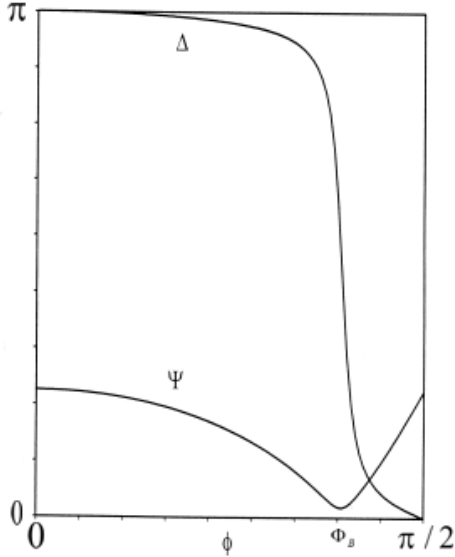


Figure 1.2: Ellipsometric parameters versus the angle of incidence.

One can conveniently characterize the elliptically polarized light with the parameters  $\Psi$  and  $\Delta$  (see fig. 1.3).  $\Psi$  is the azimuth angle and  $|\tan \Delta|$  is the ratio of the ellipse axes.  $\Psi$  varies from zero to  $\pi/4$ , but for  $\Delta$  there are different conventions using either the range  $-\pi/2 < \Delta < \pi/2$  or else  $0 < \Delta < \pi$ . Both conventions are equivalent since  $\Delta$  is defined as a phase difference and equations 1.3 and 1.4 only contain  $\cos(\Delta)$ . Originally  $\Psi$  and  $\Delta$  were chosen because they are the output of the original null-ellipsometer. They also have an important physical meaning.  $\Psi$  is sensitive to the angle of incidence as compared to Brewster's angle (the angle of minimum intensity of  $p$  polarized light), and is minimum at this angle. Therefore,  $\Psi$  is equal to  $\pi/4$  for

$\phi = \pi/2$  and  $\phi = 0$ .  $\Delta$  is related to absorption of the sample. So, for a transparent sample  $\Delta$  is either  $\pi$  (below Brewster angle) or 0 (above Brewster angle). In

the case of absorption  $\Delta$  will be between these values and will tend to  $\pi/2$  as the absorption increases. The rapid decline in  $\Delta$  near the Brewster angle indicates that the sample is not very absorptive, smoother decline corresponds to a higher absorption.

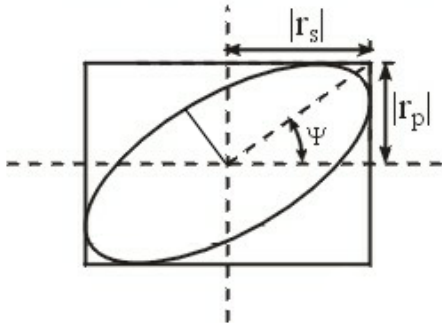


Figure 1.3: Polarization ellipse of the reflected light.

Formulas 1.1, 1.2 illustrate the simplest way of evaluating the dielectric constants of a sample. In general, one may have to take into account the anisotropy of a material (as is the case for HTSC), imperfections of optical elements in the experimental setup, diffraction effects, depolarization of light, and nonlinear effects. After all, one has to find a good compromise between the complicity of the formalism, the accuracy of the measurement, and the number of effects that need and can be corrected for.

### 1.3 Basic setup for ellipsometry

The sketch of a simple ellipsometric setup is depicted in fig. 1.4. One needs to measure the parameters  $\Psi$  and  $\Delta$  in order to calculate the dielectric constants of a sample using the equations in 1.1, 1.2. There are several different kinds of ellipsometric setups. The present experiments have been performed with a so-called rotating analyzer ellipsometer where the sample is placed between two polarizers one of which is rotated while the other one is kept fixed as sketched in figure 1.4.

The components are a monochromatic light source, an ideal polarizer oriented at the angle  $\alpha_1$ , the reflection at angle  $\phi$  upon the ideal sample which is described by the parameters  $\Psi$  and  $\Delta$ , a second rotating ideal polarizer (the so-called analyzer) placed behind the sample, and an ideal detector that measures the intensity depending on the analyzer angle. The detector sensitivity must be independent from the polarization state of the incoming light. In this ideal case the relative intensity will have the form:

$$J(\alpha_2)/J_0 = 1 + A \cos 2\alpha_2 + B \sin 2\alpha_2, \quad (1.5)$$

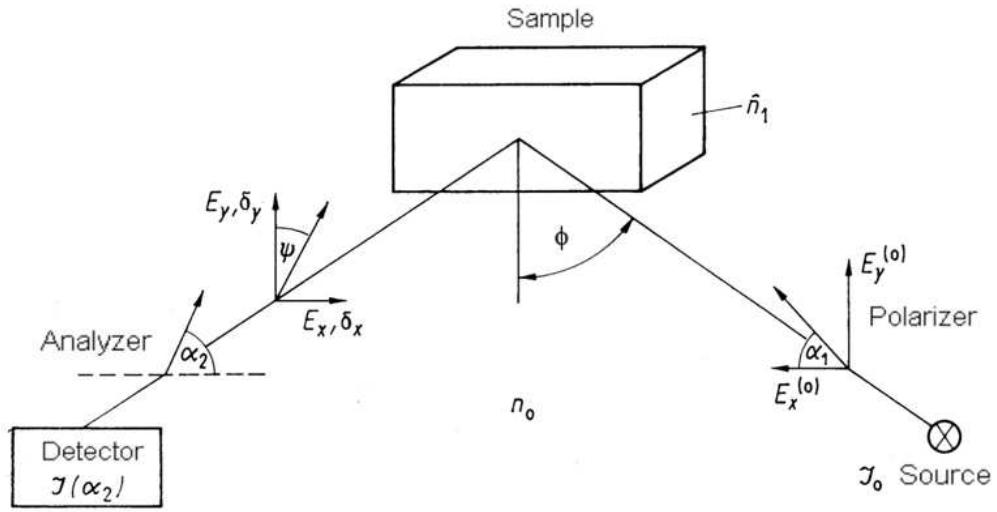


Figure 1.4: Sketch of ellipsometric setup with rotating analyzer [8].

where  $A = (\cos 2\alpha_1 - \cos 2\Psi) / (1 - \cos 2\Psi \cos 2\alpha_1)$ ,  
 $B = \sin 2\Psi \sin 2\alpha_1 \cos \Delta / (\cos 2\alpha_1 - \cos 2\Psi)$ . From the measured dependence  $J(\alpha_2)$  the coefficients  $A$  and  $B$  can be obtained by performing a fit to the experimental data in form of 1.5. Accordingly  $\Psi$  and  $\Delta$  are

$$\tan \Psi = \tan \alpha_1 \sqrt{\frac{1-A}{1+A}}, \quad \cos \Delta = \frac{B}{\sqrt{1-A^2}} \quad (1.6)$$

Eventually, from  $\Psi$  and  $\Delta$  one obtains the dielectric constants by using equations 1.1, 1.2. The extension of ellipsometry to a wide spectral range requires either the use of a monochromator (typically based on gratings) or a so-called Fourier-transform interferometer. The former is most commonly used in the visible and ultraviolet spectral range while the latter is more advantageous in the far-infrared to mid-infrared spectral range. This thesis mostly contains the description of infrared experiments, and, thus, the infrared ellipsometry will be described in more detail.

To have the option to measure the temperature dependence of the dielectric constants one also has to incorporate a cryostat into the ellipsometer. This requires the use of optical windows that are located in between the polarizer and analyzer. The properties of these windows are rather crucial since they can give rise to rather large errors in the ellipsometric measurements.

## 1.4 Requirements to an ellipsometer

### 1.4.1 Assumptions of ellipsometry theory

Most important are nearly perfect polarizers which allow one to apply the equations of ellipsometry. Furthermore, the infrared beam (which is invisible to the human eye) must be well aligned so that the angle of incidence is well defined and the beam passes through the center of both polarizers. Otherwise, the dependence  $J(\alpha_2)$  will be different from 1.5. Namely, it will contain terms proportional to  $\sin 4\alpha_2$ , and  $\cos 4\alpha_2$  and to higher harmonics of the analyzer angle. The quality of the alignment can be tested by studying the higher harmonics in 1.5 (see fig. 1.5). For the case of a good alignment the average value of  $a_4$ , and  $b_4$  must be zero and frequency independent (except for the statistical noise). In the opposite case, the fourth harmonic becomes finite which indicates that the conditions for the application of 1.5 may not be fulfilled anymore. The second crucial assumption for

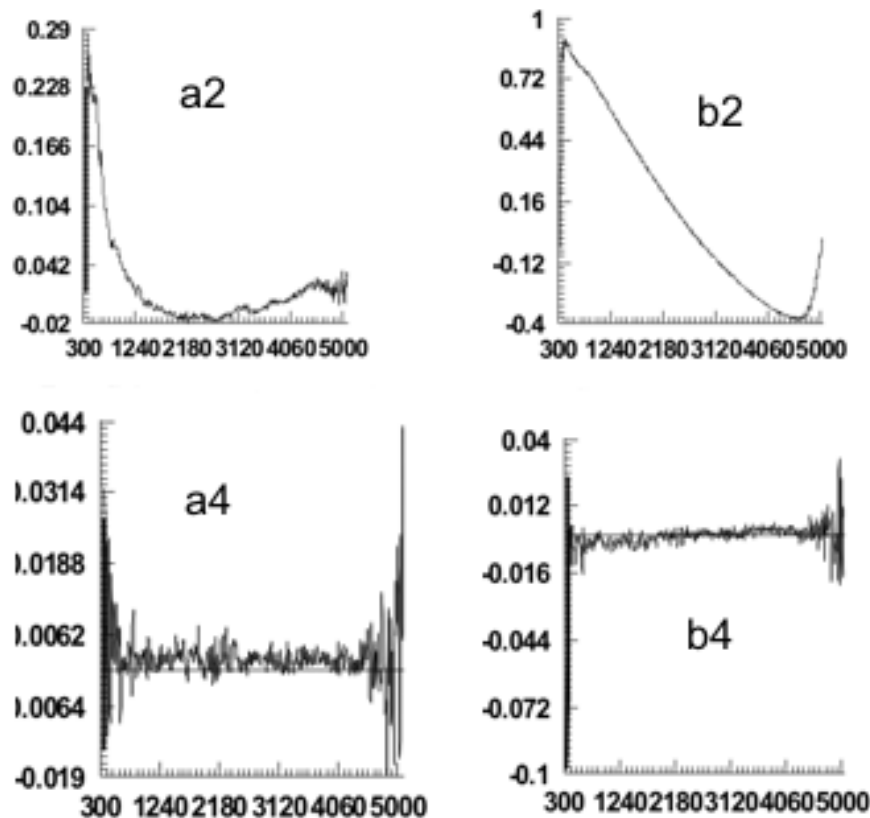


Figure 1.5: Fourier coefficients for second ( $a_2$ ,  $b_2$ ) and fourth ( $a_4$ ,  $b_4$ ) harmonics of analyzer angle  $\alpha_2$ .



the ellipsometric equations is an ideal sample, which has a flat surface that does not depolarize the light, and which does not give rise to diffraction effects (due to its finite size). In a real experiment, the "sample" actually is represented by a combination of a compensator (phase retarder), the real sample (crystal), spatial filters, and the cryostat windows. All these parts should not depolarize the light. In the case of depolarization the amplitudes  $a_2$ ,  $b_2$  in the fit 1.5 will decrease, and this consequently distorts the deduced dielectric constants of the sample. Third, the formula for  $J(\alpha_2)$  does not take into account the polarization dependence of the detector sensitivity. Therefore the detector must show the same intensity for different polarizations of the incoming beam. Finally, all elements should have close to linear infrared response, so that nonlinear effects can be neglected.

### 1.4.2 List of requirements

Summarizing these requirements one can make the following list:

1. Polarizers with extremely small imperfection
2. Non-depolarizing compensator with low absorption
3. Non-depolarizing cryostat windows
4. Polarization independent detector with linear response
5. The sample big enough to neglect the diffraction effects
6. The possibility to set the angle of incidence with good accuracy
7. The possibility to change the angle of incidence

Finally, it is necessary to remark that all items of the list should be fulfilled over the whole frequency range used for a measurement.

## 1.5 Principles of Fourier-transform spectroscopy (FTS)

As it was mentioned before, there are two possible realizations to measure frequency dependence: the conventional way - monochromators, and the Fourier

transform spectroscopy (FTS) method, which became available since the development of computers. Before the computer age, calculation problems prevented realization of the FTS. Nowadays, FTS is the most convenient way to quickly measure dielectric constants over a broad frequency range. Commercial FTS setups presently available from Bruker. The first Bruker setup was designed and proposed by L. Genzel[3].

FTS is based on an interferometer with two arms, one of which is periodically moving. A classical example is the Michelson interferometer with a moving mirror in one of its arms (see fig. 1.6). If we introduce the coordinate of the moving

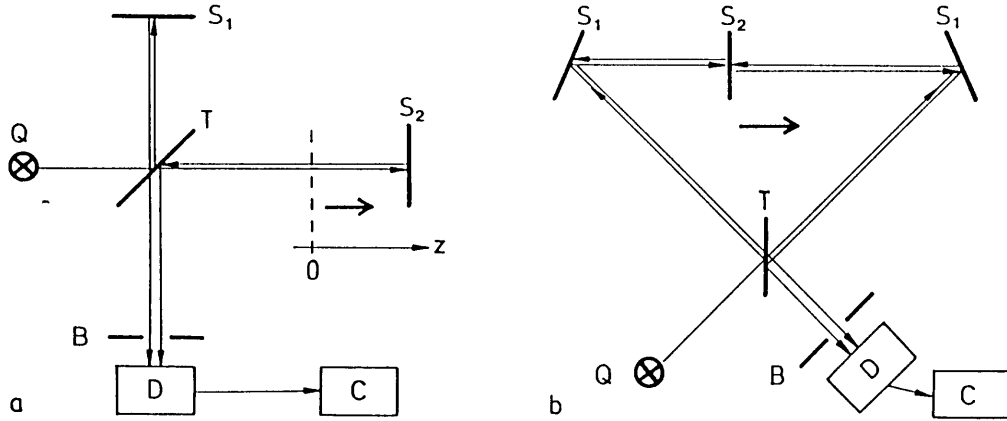


Figure 1.6: Michelson interferometer (a); basic elements of Bruker interferometer (b). [3]

mirror  $z$ , and the intensity  $I(z)$ , then the complex spectrum  $F_c(\omega)$  will be given by the Fourier transform:  $F_c(\omega) \propto \int_{-\infty}^{+\infty} I(z) \exp(-i\omega z) dz$ , where  $\omega$  is the frequency ( $\omega = 2\pi\nu$ ). For non-dispersive media inside interferometer, that is the general assumption, the spectrum is a real quantity and can be given by the following formula:

$$F(\omega) \propto \int_0^{+\infty} I(z) \cos(\omega z) dz. \tag{1.7}$$

The realization of any interferometer does not allow to measure intensity  $I(z)$  in infinite range. Therefore, the integral 1.7 is taken only up to final value of  $z$ . This is the so called apodisation problem [3], which can be solved by a properly chosen apodisation function  $S(z)$ . Then the real observed spectrum is the following integral  $F_{obs}(\omega) \propto \int_0^{z_{max}} I_{obs}(z) \cos(\omega z) dz$ , where  $I_{obs}(z) = I(z)S(z)$ . Our Bruker setup can be configured to use the following apodisation functions: Happ-Genzel, Black-Harris, and Norton-Beer. The first two functions are plotted in fig 1.7 and

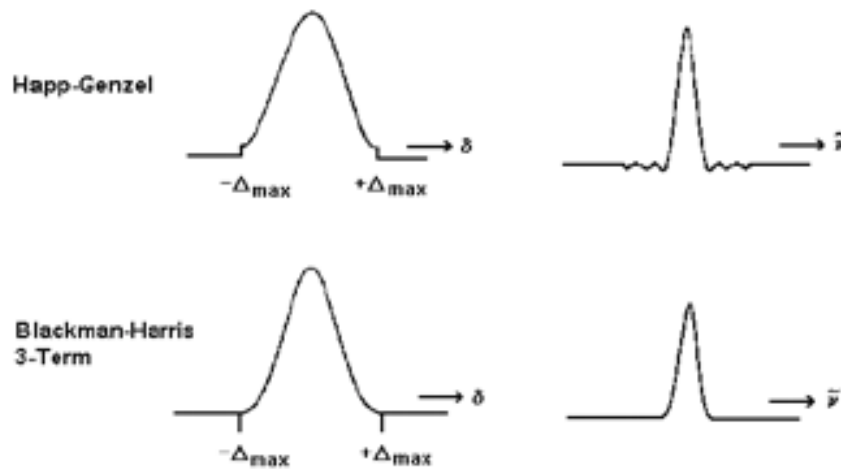


Figure 1.7: Apodisation functions for FTS

the last one is described in detail in [4]. Classical apodisation functions are also listed in [5].

As it was mentioned already, another problem coming from the equation 1.7 is the assumption of a non-dispersive media inside an interferometer. In practice, the complex spectrum is not absolutely symmetric due to errors in the estimation of the mirror position  $\Delta z$  as well as due to dissipation effects, and some correction has to be introduced before using of the equation 1.7. The complex spectrum can be presented in the form:  $F_c(\omega) = F(\omega) \exp(-i\theta(\omega))$ , where  $\theta(\omega)$  is the complex phase. In this case of asymmetric interferogram,  $F_c(\omega)$  is multiplied by some phase correction function, which makes the spectrum closer to symmetric. In a Bruker interferometer two correction functions can be selected: Mertz correction (multiplication to the phase with opposite sign), and Power corrections (using the ratio of actual real intensity and the calculated intensity).

A beam-splitter is one of the most important elements of a FTS spectrometer. It should have very good quality and its working band should be as wide as possible. The most widely used Bruker FTS spectrometer contains a set of several beam-splitters each of which covers either mid-infrared or far-infrared spectral range. The alignment of the interferometer is also a critical factor since even small misalignment can introduce large phase errors in the interferogram. All these problems were mainly solved in the commercial Bruker setups, and this is the main reason of popularity of these spectrometers.

## 1.6 Ellipsometry with FTS

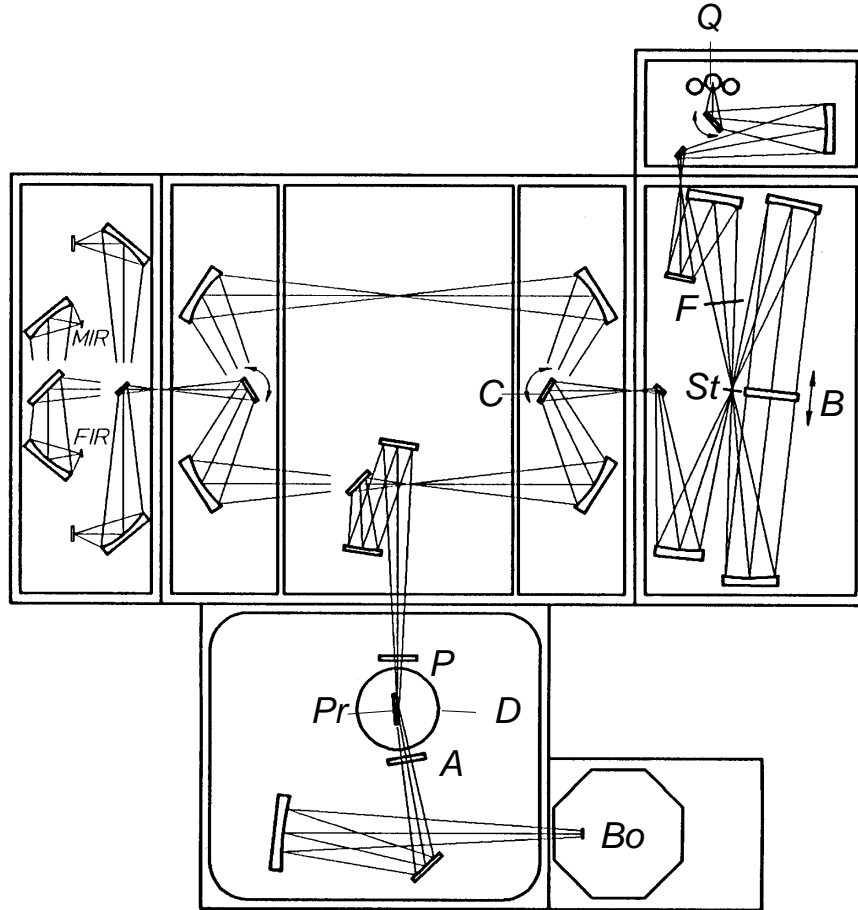


Figure 1.8: Ellipsometer in Stuttgart.

An appealing idea is combining ellipsometry with FTS and thus to use the advantages of both techniques at the same time. In practice, an ellipsometer is attached to a FTS spectrometer, and the signal from the ellipsometer detector is used as an input into the signal box of the FTS system. In this case the intensity is a function of the analyzer angle and the mirror coordinate  $J = J(\alpha_2, z)$  of the FTS. This dependence demands a high stability of the analyzer angle which is very difficult to achieve in practice. Most of the infrared polarizers are based on thin films which easily vibrate and thus introduce time dependent intensity changes that affect the data analysis of the FTS system. If the vibration can not be eliminated one can shift the vibrational noise by changing the velocity of the moving mirror. The second problem of such setups is their complexity: the setup contains lots of mirrors and other elements. In particular, the interferometer

itself leads to a slow drift of parameters with time, which can not be neglected in some cases. In the case of an ellipsometric measurement this puts a limit on maximum amount of time that is available for taking a single spectrum. The detector should be also fast enough for FTS. Normally, the amplitude of the signal decreases as the moving mirror velocity increases. Eventually, all of these problems can be resolved by tuning the setup and by proper selection of elements for the ellipsometer.

## 1.7 Experimental setup in MPI Stuttgart

Our setup in Stuttgart consists of a Bruker-IFS113V FTS and a home-made ellipsometer [6]. The infrared ellipsometer including spectrometer is plotted in fig. 1.8 The ellipsometer covers the spectral range from 30 to 5000  $cm^{-1}$  divided in three bands: very far infrared (below 100  $cm^{-1}$ ), far-infrared (100-700  $cm^{-1}$ ) and mid-infrared (700-5000 $cm^{-1}$ ). The Bruker contains three sources of radiation (Q), far-infrared(mercury lamp), mid-infrared(globar), and not used near visible(tungsten). At the entry of the interferometer a variable aperture is placed to regulate the size of the spot. The interferometer contains a rotating drum with a set of beam-splitters (St). We use KBr beam-splitter in mid-infrared, and coated mylar in far-infrared. The beam-splitters are made by Bruker. The ellipsometer is attached to the Bruker by introducing several mirrors in the Bruker sample chamber, and the light beam directly goes from the Bruker toward a polarizer. We use FIR polarizers from Russia (General Physics Institute) and MIR polarizer from Infraspets [9]. These two sets of polarizers cover the spectral range from 20 to 5000  $cm^{-1}$ . The imperfections of the polarizers are less than 0.1% in the working frequency band. The polarizers are grid type and free-standing or evaporated on a mylar film. The orientation of both polarizers is electronically controlled to maintain a high angular accuracy. Our compensator units are based on Si prism in the FIR, and SeZn ones in the MIR. Generally, a compensator (phase retarder) enables accurate ellipsometric measurements of samples with high reflection coefficient, since an additional phase shift is introduced by the compensator, and, consequently, the ellipsometric parameter  $\Delta$  is shifted away from 0. The commercial cryostat from CryoVac allows to measure the temperature dependence in the range of 4K to 450K. The cryostat windows are made of 3 $\mu m$  mylar for FIR and KBr for MIR. We also use diamond windows, which are applicable in

total spectral range but lead to significant reflection losses due to their relatively high index of refraction. The detector is based on a standard Si bolometer from Infrared Laboratories Inc. It is operated either at 4.5K or at 1.7K to obtain higher sensitivity in the FIR range. The detector response needs to be polarization independent. We therefore use a special detector window made either of wedged CVD diamond (MIR) or polyethylene (FIR). The bolometer contains a set of polyethylene(FIR) or germanium(MIR) cold filters. Some of them contain diamond powder with different grain diameters. They are needed to prevent the bolometer element from being heated up by unwanted infrared or visible radiation. The focusing system of the bolometer is also a critical part. In the original bolometer it is a cone that guides the light to the element. We introduced small apertures in front of the window in order to define and reduce the beam size so that there are no grazing-angle reflections inside the cone. Recently, we have replaced the cone with a special focusing optics, which improved the sensitivity of the detector and strongly reduces polarization effects. Briefly, the setup elements are described in table 1.1.

Element	Manufacturer	Remarks
FT spectrometer IFS113v	Bruker Optics	
MIR Polarizers	Infraspecs	700-5000 $cm^{-1}$
FIR Polarizers	Gen.Phys.Inst. (Moscow)	20-700 $cm^{-1}$
Cryostat and temperature controller	Cryovac Inc	4-450K
Bolometer	Infrared Labs Inc.	
Compensators	MPI Stuttgart	

Table 1.1: Elements of the ellipsometer in MPI Stuttgart

The setup is mostly automatic and controlled by a PC. First of all one makes the alignment of the optics using the visible light coming from the mercury lamp, and CaF beam-splitter which transmits in visible range and has the same optical width as our IR beam-splitters, so that the beam goes almost the same way with the CaF and the IR beam-splitters. Subsequently, a visible layer beam is used for further alignment. The laser should be aligned collinear with the visible beam from the mercury lamp. The angle of incidence can be set to 85, 80, and 75 degrees. After the sample has been mounted, one does two test measurements with and without the cryostat lids (which also contain the windows). The coincidence of the results of these two measurements means that the cryostat window does not change the polarization state of the light and that additional or multiple

reflection from parts of the cryostat (mostly the sample holder) have been successfully avoided. If the window changes the polarization one can use the simple correction which is based on the relation  $\rho_{sample+window} = \rho_{window}\rho_{sample}$ , where  $\rho = \tan \Psi \exp i\Delta$ . Then one has to wait until the cryostat is pumped to  $10^{-6}mbar$  or  $10^{-4}Pa$ . This high vacuum is required to prevent formation of an ice on a sample at low temperature. Then the temperature dependence of dielectric constants is measured. The experimental run at a fixed temperature goes automatically, but the changing of temperatures is manual. After the temperature dependence has been measured, one needs to do the ellipsometric calibration to determine the exact zero positions of the analyzer and the polarizer. This calibration procedure uses results measured at few (usually 2 or 3) polarizer angles and the fact that the spectrum should be independent of the polarizer angle. This turns out as a classical mathematical problem of function minimization. Eventually, one finds corrections for the analyzer and polarizer angles. We have a special computer program to do all calculations related to the calibration procedure. Samples with thickness down to 0.1mm can be measured using our setup. However, one needs special diffraction correction procedures for such a small samples as described in [131].

## 1.8 Setup in Karlsruhe. Ellipsometry with a synchrotron source

Using a synchrotron as a source for FT ellipsometry gives a big advantage as compared with conventional IR sources like a mercury lamp. The synchrotron beam is about 100-1000 times more brilliant than the beam from conventional lamps. The entire intensity is contained here in a nearly collimated beam which is perfectly suited for ellipsometric measurements. Accordingly, the use of a synchrotron light source provides significant advantages for ellipsometric measurements, in particular, towards the far-infrared spectral range and for the investigation of very small samples. However, synchrotron radiation also has its specific features that one has to take into account in doing ellipsometry. The most important feature is that the radiation is polarized, see fig. 1.9. For instance, this affects the choice of the proper polarizer angle. In this case, one has to find the compromise between the intensity and the average value of  $\Psi$ . With ordinary sources one only needs to consider the second factor. Our second ellipsometric setup is located at

the ANKA synchrotron at the Forschungszentrum Karlsruhe. This synchrotron has an energy 2.5GeV and the IR radiation is produced in the range from 4 to  $10000\text{cm}^{-1}$ . The setup consists of a Bruker IFS-66v spectrometer and a home-built ellipsometer which is more advanced than the ellipsometer in Stuttgart [130]. This setup allows for an extended range of the angle of incidence varying from 65 to 90 degrees. The sample alignment procedure can be done here without using a laser because the synchrotron intensity in the visible range is sufficiently high. When measuring with a synchrotron, one has to take into account the decay of the electron current with time which changes the beam intensity during the experimental run. We have implemented a system that monitors and reads to beam current and thus allows for a correction of the ellipsometric spectra. In the particular case of the ANKA synchrotron the beam decays very slowly such that the correction procedure is not required unless extremely long scans are performed.

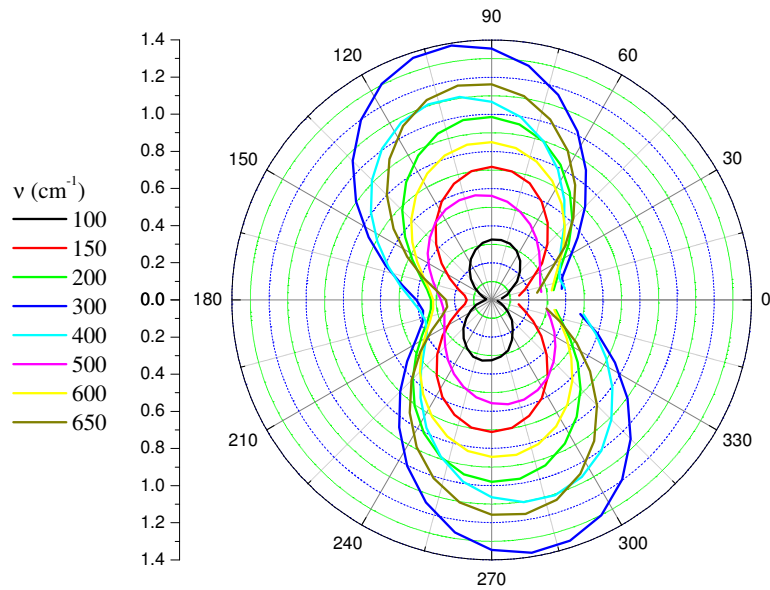


Figure 1.9: Polarization of synchrotron radiation at ANKA.

## 1.9 Sample preparation

A very important issue for accurate ellipsometric measurements concerns the quality of the sample surface. The sample preparation is thus a very important experimental aspect. Firstly, the size of the sample surface should be as large as



possible. A large surface results in a higher signal and thus minimizes the ratio of signal to noise. In addition, the large surface allows one to minimize diffraction effects which can become rather severe at the relatively high angles of incidence required in ellipsometry. Unfortunately, in case of the HTSC it is generally rather difficult to obtain sufficiently large single crystals due to problems in the crystal growth.

Given a sufficient size of the crystal the second important requirement concerns the quality of the surface. It should be absolutely flat and clean in order to apply the equations of ellipsometry. For a real crystal the surface usually is polished by using special polishing oil with  $1 \mu m$  grain size for IR ellipsometry and  $0.25 \mu m$  for visible range. The surface quality can in fact be inferred from the ellipsometric spectra. For instance, the presence of a decomposed surface layer is evident in most cases from the occurrence of characteristic defect modes (see discussion in chapter 2).

Finally, the correct mounting of the sample inside the cryostat is also an important issue. A good thermal contact to the sample holder is crucial for studying reliably the temperature dependence of the optical response. The orientation of the crystal axes of an anisotropic sample should also be in good coincidence with the plane of incidence and the polarization state of the incoming light. No intensity reflected from the sample holder should reach the detector. To solve this problem special filters are applied. They are made from the material with high absorption in the IR range.

## 1.10 Generalized ellipsometry

### 1.10.1 General description of dielectric constant extraction from ellipsometric parameters

There are two common ways to determine the influence of linear optical elements on light. Using these methods one can find relations between ellipsometric parameters, detected intensity and parameters of a setup. These two methods are called the Müller matrix formalism and the Jones matrix formalism. The advantage of a matrix formalism is that each element of an ellipsometer can be considered separately, then matrices multiplied to obtain the complete relationship between the incoming light and the detected intensity for the cases of different samples

and different ellipsometric configurations. The Jones matrix formalism uses  $2 \times 2$  complex matrices and is the simplest of these two methods. The Müller matrix formalism operates with  $4 \times 4$  matrices and is necessary to consider partially polarized light. More detailed description of the Jones and Müller formalisms can be found in the works of Azzam and Bashara [7] and Röseler [8].

### Brief Overview of Polarization States of Light

In this section, basic parameters of polarized light are considered. So, completely polarized light can be represented as

$$\vec{E} = \Re \left[ \vec{\mathcal{E}} e^{i\vec{k}^L \vec{r} - i\omega t} \right] \quad (1.8)$$

where  $\vec{\mathcal{E}}$  is the complex amplitude of the light,  $\omega$  is the angular frequency,  $\vec{k}^L$  is the wave vector,  $t$  is time, and  $\vec{r}$  is the position vector,  $\Re$  is the real part function. The equation (1.8) can be broken into two components as:

$$\vec{E} = \Re \left\{ \begin{bmatrix} \vec{\mathcal{E}}_p \\ \vec{\mathcal{E}}_s \end{bmatrix} e^{i\vec{k}^L \vec{r} - i\omega t} \right\} = \Re \left\{ \begin{bmatrix} |\vec{\mathcal{E}}_p| \vec{e}_p e^{i\delta_p^L} \\ |\vec{\mathcal{E}}_s| \vec{e}_s e^{i\delta_s^L} \end{bmatrix} e^{i\vec{k}^L \vec{r} - i\omega t} \right\} \quad (1.9)$$

here  $\mathcal{E}_p$ ,  $\mathcal{E}_s$ ,  $\delta_p^L$ ,  $\delta_s^L$  are amplitudes and phases of the electric field components that are parallel ( $p$  polarization) and perpendicular ( $s$  polarization) to the plane of incidence, respectively. As a result, we have the electric field tracing out an ellipse as a function of time. To connect it with ellipsometry one defines the parameters  $\psi$  and  $\Delta$  as

$$\tan \psi^L = \frac{|\mathcal{E}_p|}{|\mathcal{E}_s|} \quad (1.10)$$

$$\Delta^L = \delta_p^L - \delta_s^L \quad (1.11)$$

$\psi^L$  is related to the tilt of the ellipse, and  $\Delta^L$  is related to the eccentricity of the ellipse, being 0 or  $\pi$  for circular polarization when  $\mathcal{E}_p = \mathcal{E}_s$ . If a sample is described in terms of  $\psi$  and  $\Delta$  defined through the reflective index then the light reflected from the sample will have  $\psi^L = \psi$  and  $\Delta^L = \Delta$ .

### Müller matrix formalism

The Müller matrix formalism is associated with the Stokes parameters of light. For a completely polarized wave, these parameters are defined as:

$$s_0 = |\mathcal{E}_p|^2 + |\mathcal{E}_s|^2 \quad (1.12)$$

$$s_1 = |\mathcal{E}_p|^2 - |\mathcal{E}_s|^2 \quad (1.13)$$

$$s_2 = 2|\mathcal{E}_p||\mathcal{E}_s| \cos \Delta^L \quad (1.14)$$

$$s_3 = 2|\mathcal{E}_p||\mathcal{E}_s| \sin \Delta^L. \quad (1.15)$$

These quantities have the dimensions of intensity and represent the different possible states of polarization of a quasi-monochromatic electromagnetic wave. Partially polarized and unpolarized light is included by the use of Stokes parameters. The value  $s_0$  is proportional to the energy of a light wave,  $s_1$  adds information about its polarization ellipse, while  $s_2$  and  $s_3$  contain information about the eccentricity of the ellipse. Using Stokes parameters, we can obtain the following relations for the ellipsometric angles:

$$s_1/s_0 = -\cos 2\psi^L \quad (1.16)$$

$$s_2/s_0 = \sin 2\psi^L \cos \Delta^L \quad (1.17)$$

$$s_3/s_0 = \sin 2\psi^L \sin \Delta^L. \quad (1.18)$$

Following from (1.16 - 1.18) the four Stokes parameters are not independent for the case of completely polarized light since:

$$s_0^2 = s_1^2 + s_2^2 + s_3^2. \quad (1.19)$$

In the opposite case of unpolarized light  $\mathcal{E}_p = \mathcal{E}_s$ , and  $\Delta^L$  is a rapidly varying random function ( $\cos \Delta^L = \sin \Delta^L = 0$  on average), so that  $s_0 > 0$  and  $s_1 = s_2 = s_3 = 0$ . Partially polarized light can be presented as the sum of completely polarized and unpolarized components, and we have another relation instead of (1.19), namely:

$$s_0 = s_{0u} + s_{0p} = s_{0u} + \sqrt{s_1^2 + s_2^2 + s_3^2} \quad (1.20)$$

where  $s_{0u}$ ,  $s_{0p}$  are the intensities of unpolarized and polarized parts of the light, correspondingly. The degree of polarization is the ratio of the intensity of the

polarized component to the one of the total wave:

$$P_{0l} = \frac{s_{0p}}{s_0} = \frac{\sqrt{s_1^2 + s_2^2 + s_3^2}}{s_0} \leq 1. \quad (1.21)$$

This formula has a simple geometric interpretation. Since  $P_{0l} = 0$  is unpolarized light, each point on the surface of the unit sphere,  $P_{0l} = 1$ , represents a distinct totally polarized state. Excluding the origin, a point inside the unit sphere,  $0 < P_{0l} < 1$  represents a partially polarized wave. The equality holding for the case of totally polarized light, where equations (1.16 - 1.18) are valid.

The transformations of the Stokes parameters are carried out by the 4x4 Müller matrix. The processing of the light wave by the optical system is calculable from the premultiplication of an incident Stokes vector by the system of Müller matrix to produce the Stokes vector of the outgoing wave. Note that the elements of the Müller matrix are real. So we have:

$$\vec{S}_e = \mathbf{M}\vec{S}_i \quad (1.22)$$

where  $\mathbf{M}$  is the Müller matrix, and  $S_e$  and  $S_i$  are the Stokes vectors of the final and initial polarization states, respectively. These vectors are of the form:

$$\vec{S} = \begin{pmatrix} s_0 \\ s_1 \\ s_2 \\ s_3 \end{pmatrix}. \quad (1.23)$$

The important property of the Müller matrix is that one can compute the matrix of a cascaded optical system by multiplication

$$\mathbf{M} = \mathbf{M}_N \mathbf{M}_{N-1} \mathbf{M}_{N-2} \dots \mathbf{M}_1 = \prod_{i=1}^N \mathbf{M}_i. \quad (1.24)$$

This allows one to calculate an intensity at a detector as the final result of all multiplications of an initial Stokes vector to Müller matrices of each optical element of the system. The necessary matrices are as follows: the Müller matrix for

ideal polarizer with orientation  $\alpha$ :

$$\mathbf{M} = \frac{1}{2} \begin{pmatrix} 1 & \cos 2\alpha & \sin 2\alpha & 0 \\ \cos 2\alpha & \cos^2 2\alpha & \sin 2\alpha \cos 2\alpha & 0 \\ \sin 2\alpha & \sin 2\alpha \cos 2\alpha & \sin^2 2\alpha & 0 \\ 0 & 0 & 0 & 0 \end{pmatrix} \quad (1.25)$$

the retarder with retardation  $\delta$ :

$$\mathbf{M} = \begin{pmatrix} 1 & 0 & 0 & 0 \\ 0 & 1 & 0 & 0 \\ 0 & 0 & \cos \delta & \sin \delta \\ 0 & 0 & -\sin \delta & \cos \delta \end{pmatrix} \quad (1.26)$$

the reflecting surface with the ellipsometric parameters  $\psi$ ,  $\Delta$  and the reflection coefficients  $r_x$  and  $r_y$ :

$$\mathbf{M} = \frac{|r_x|^2 + |r_y|^2}{2} \begin{pmatrix} 1 & -\cos 2\psi & 0 & 0 \\ -\cos 2\psi & 1 & 0 & 0 \\ 0 & 0 & \sin 2\psi \cos \Delta & \sin 2\psi \sin \Delta \\ 0 & 0 & -\sin 2\psi \sin \Delta & \sin 2\psi \cos \Delta \end{pmatrix} \quad (1.27)$$

the partial linear polarizer with the maximum and minimum transmittances  $\tau_M$  and  $\tau_m$ :

$$\mathbf{M} = \frac{1}{2} \begin{pmatrix} \tau_M + \tau_m & \tau_M - \tau_m & 0 & 0 \\ \tau_M - \tau_m & \tau_M + \tau_m & 0 & 0 \\ 0 & 0 & 2\sqrt{\tau_M \tau_m} & 0 \\ 0 & 0 & 0 & 2\sqrt{\tau_M \tau_m} \end{pmatrix}. \quad (1.28)$$

The matrix (1.28) is similar to (1.27) with ellipsometric parameters  $\psi = \Delta = 0$ .

Now we consider the transformations of Stokes vector and Müller matrix under rotation of a Cartesian coordinate system. Let  $\vec{S}'$  and  $\mathbf{M}'$  be the Stokes vector and Müller matrix in the system having been rotated to the angle  $\alpha$ , and  $\vec{S}$  and  $\mathbf{M}$  represent these quantities in the original system. Then the transformation laws from  $\mathbf{M}$  to  $\mathbf{M}'$  and from  $\vec{S}$  to  $\vec{S}'$  are follows:

$$\vec{S}' = \mathbf{R}(\alpha)\vec{S} \quad (1.29)$$

$$\mathbf{M}' = \mathbf{R}(\alpha)\mathbf{M}\mathbf{R}(-\alpha) \quad (1.30)$$

where  $\mathbf{R}$  is the rotator matrix given by

$$\mathbf{R}(\alpha) = \begin{pmatrix} 1 & 0 & 0 & 0 \\ 0 & \cos 2\alpha & \sin 2\alpha & 0 \\ 0 & -\sin 2\alpha & \cos 2\alpha & 0 \\ 0 & 0 & 0 & 1 \end{pmatrix} \quad (1.31)$$

Thus, using Müller matrices, one obtains the Stokes vector for the light passing through a polarizer, bouncing off the sample, passing through an analyzer and finally incidenting on the detector  $\vec{S}_d$  as:

$$\vec{S}_d = \mathbf{M}_A \mathbf{M}_S \mathbf{M}_R \mathbf{M}_P \begin{pmatrix} I_0 \\ 0 \\ 0 \\ 0 \end{pmatrix} \quad (1.32)$$

here  $I_0$  is the intensity of the beam in front of a polarizer. The element  $S_{d0}$  is the intensity in front of the detector  $I_d$ . Looking at the representations of Müller matrices for the work elements of the device, one can conclude that the ratio of intensities  $I_d/I_0$  is a function of the analyzer angle, the polarizer angle, the angle of incidence, and the ellipsometric parameters  $\psi$  and  $\Delta$  of a sample. These conclusions are also valid for the remaining parameters of the Stokes vector  $s_1$ ,  $s_2$ ,  $s_3$ . Since characteristics of the analyzer and the polarizer are known, one can obtain the values of  $\psi$  and  $\Delta$ , and afterwards, the dielectric function of the sample. The specific realization and accuracy depends on the approach and Müller matrices used for the description of known elements of the optical system.

### Jones matrix formalism

We consider the propagation of a uniform monochromatic plane wave  $\vec{E}(x, y, z, t) = \vec{\mathcal{E}}(x, y, t) e^{ikz}$ . The electric field of this wave can be represented as a  $2 \times 1$  vector, the so-called Jones vector:

$$\vec{\mathcal{E}} = \begin{pmatrix} \mathcal{E}_x \\ \mathcal{E}_y \end{pmatrix}. \quad (1.33)$$

For ellipsometry it is convenient to direct the axes  $x$  and  $y$  along  $p$  and  $s$  polarizations respectively, then  $\mathcal{E}_x = \mathcal{E}_p$  and  $\mathcal{E}_y = \mathcal{E}_s$ . From this time dependent  $2 \times 1$  Cartesian Jones vector the  $2 \times 2$  coherency matrix can be constructed by

the direct multiplication of  $\vec{\mathcal{E}}$  to its Hermitian adjoint<sup>1</sup>:

$$\mathbf{J} = \langle \vec{\mathcal{E}}(t) \times \vec{\mathcal{E}}^\dagger(t) \rangle = \begin{pmatrix} \langle \mathcal{E}_x \mathcal{E}_x^* \rangle & \langle \mathcal{E}_x \mathcal{E}_y^* \rangle \\ \langle \mathcal{E}_y \mathcal{E}_x^* \rangle & \langle \mathcal{E}_y \mathcal{E}_y^* \rangle \end{pmatrix}. \quad (1.34)$$

The brackets  $\langle \dots \rangle$  denote the time averaging. Eventually, we have obtained  $2 \times 2$  time independent coherence matrix, which is also called Jones matrix. The elements  $J_{xx}$ ,  $J_{yy}$  present the intensities of the  $x$  and  $y$  wave components, and total intensity can be calculated as the trace of this matrix. For a monochromatic wave, products  $\mathcal{E}^*$  appear to be time independent, and the Jones matrix assumes the form:

$$\mathbf{J} = \begin{pmatrix} a_x^2 & a_x a_y e^{i\Delta} \\ a_y a_x e^{-i\Delta} & a_y^2 \end{pmatrix} \quad (1.35)$$

where  $a_x = |\mathcal{E}_x|$ ,  $a_y = |\mathcal{E}_y|$  are the magnitudes of the wave components,  $\Delta = \delta_x - \delta_y$  is the ellipsometric parameter of the wave. By virtue of the definition of Stokes parameters (see formulae 1.12-1.12 on the page 34), they can be presented as functions of Jones matrix elements and vice versa:

$$s_0 = a_x^2 + a_y^2 = J_{xx} + J_{yy} \quad (1.36)$$

$$s_1 = a_x^2 - a_y^2 = J_{xx} - J_{yy} \quad (1.37)$$

$$s_2 = 2a_x a_y \cos \Delta = J_{xy} + J_{yx} \quad (1.38)$$

$$s_3 = 2a_x a_y \sin \Delta = -i(J_{xy} - J_{yx}) \quad (1.39)$$

$$J_{xx} = \frac{1}{2}(s_0 + s_1) \quad (1.40)$$

$$J_{yy} = \frac{1}{2}(s_0 - s_1) \quad (1.41)$$

$$J_{xy} = \frac{1}{2}(s_2 + i s_3) \quad (1.42)$$

$$J_{yx} = \frac{1}{2}(s_2 - i s_3). \quad (1.43)$$

---

<sup>1</sup>The Hermitian adjoint is defined as complex conjugate of transpose of the matrix.

The relations between Stokes vector and Jones matrix elements can be rewritten in the matrix form:

$$\begin{pmatrix} s_0 \\ s_1 \\ s_2 \\ s_3 \end{pmatrix} = \begin{pmatrix} 1 & 0 & 0 & 1 \\ 1 & 0 & 0 & -1 \\ 0 & 1 & 1 & 0 \\ 0 & -i & i & 0 \end{pmatrix} \begin{pmatrix} J_{xx} \\ J_{xy} \\ J_{yx} \\ J_{yy} \end{pmatrix}. \quad (1.44)$$

Coordinate transformations that transform Jones vector with the transforming matrix  $\mathbf{R}$  change the Jones matrix  $\mathbf{J}$  according to the following law:

$$\mathbf{J}' = \mathbf{R}\mathbf{J}\mathbf{R}^\dagger. \quad (1.45)$$

Note, that under unitary transformations the determinant and the trace of a Jones matrix remain invariant.

Let us assume that in front of a linear optical element, we have the Jones vector  $\vec{\mathcal{E}}$ , and  $\vec{\mathcal{E}}'$  on the output of the element. Due to linearity,  $\vec{\mathcal{E}}'$  and  $\vec{\mathcal{E}}$  are coupled by a linear transformation which is denoted as a matrix  $\mathbf{T}$ . Then, by virtue of (1.33), one has obtained the Jones matrix transformation caused by this optical element:

$$\mathbf{J}' = \mathbf{T}\mathbf{J}\mathbf{T}^\dagger. \quad (1.46)$$

The matrix  $\mathbf{T}$  is called the Jones matrix of the element, and can be applied for both transformations: of Jones vectors and of Jones matrices. The relation (1.46) can be easily extended to a cascade of consistent linear elements, and the resulting Jones matrix will be the product of Jones matrices of all elements composing the device. Jones matrices for devices used in the ellipsometry have been calculated and are known. So, a linear polarizer oriented at the angle  $\alpha$  has Jones matrix:

$$\mathbf{T}(\alpha) = \begin{pmatrix} \cos^2 \alpha & \sin \alpha \cos \alpha \\ \sin \alpha \cos \alpha & \sin^2 \alpha \end{pmatrix}. \quad (1.47)$$

A retarder with the azimuth  $\alpha$  and relative retardation  $\delta$ :

$$\mathbf{T}(\alpha, \delta) = \begin{pmatrix} \cos \frac{\delta}{2} + i \cos 2\alpha \sin \frac{\delta}{2} & i \sin 2\alpha \sin \frac{\delta}{2} \\ i \sin 2\alpha \sin \frac{\delta}{2} & \cos \frac{\delta}{2} - i \cos 2\alpha \sin \frac{\delta}{2} \end{pmatrix} \quad (1.48)$$

A reflecting surface with reflection coefficients  $r_p e^{i\delta_p}$  and  $r_s e^{i\delta_s}$  ( $r_p, r_s, \delta_p, \delta_s \in \Re$ )



to be responsible the amplitude and phase changes.):

$$\mathbf{T} = \begin{pmatrix} r_p e^{i\delta_p} & 0 \\ 0 & r_s e^{i\delta_s} \end{pmatrix} \quad (1.49)$$

Now apply the Jones matrices formalism described above to the ellipsometry device the scheme of which is depicted in Fig. 1.4 (see page 22). Let  $\vec{\mathcal{E}}$  be the electric field of the wave in front of the polarizer. Further, the wave reflects on the sample and comes through the analyzer, and the field  $\vec{\mathcal{E}}'$  in front of a detector can be presented according to the relation (1.46) as

$$\vec{\mathcal{E}}' = \mathbf{T}_A \mathbf{T}_S \mathbf{T}_R \mathbf{T}_P \vec{\mathcal{E}} \quad (1.50)$$

where  $\mathbf{T}_A$ ,  $\mathbf{T}_S$ ,  $\mathbf{T}_R$ ,  $\mathbf{T}_P$  represent the Jones matrices of the analyzer, the reflecting surface, the retarder, and the polarizer respectively. The relation (1.50) can be also presented as the evolution of the Jones matrix:

$$\mathbf{J}' = \mathbf{T}_A \mathbf{T}_S \mathbf{T}_R \mathbf{T}_P \mathbf{J} \mathbf{T}_A^\dagger \mathbf{T}_S^\dagger \mathbf{T}_R^\dagger \mathbf{T}_P^\dagger \quad (1.51)$$

where  $\mathbf{J}'$  and  $\mathbf{J}$  are the coherency matrices of the light on the detector and on the polarizer correspondingly. To calculate the intensity on the detector, one should take the trace of  $\mathbf{J}'$  or calculate  $|\mathcal{E}'|^2$  using (1.50). As the result, we will have an intensity depending on the analyzer angle that makes possible to calculate reflective coefficients of the material the sample is made of, and afterwards the dielectric function of this material at the frequency of the incident wave.

### 1.10.2 Conclusions and summary

As it is detailed above, to calculate a dielectric function of a material one should perform the following steps:

1. To choose a mathematical model to describe wave propagation.
2. To choose proper models to describe a polarizer, an analyzer, a retarder, a detector and, probably, other additional elements of ellipsometric device.
3. To choose a correct model to describe a sample structure and a reflection process correctly.

4. To make the choice between Jones and Müller matrices.
5. Using Jones or Müller matrix, to obtain the equations coupling the ellipsometric parameters of detected signal with dielectric constant of the sample.
6. Solving the equations, to obtain a desirable dielectric constant with error bars.

To describe an electromagnetic wave, one can use the Jones vector, coherency matrix, or Stokes parameters of the light. The Jones vector provides the basic framework within which one can adequately describe the propagation of totally-polarized quasi-monochromatic light through non-depolarizing optical systems. However, with partially polarized light the statistical description is required, because of the stochastic nature of the time variation of the field components. In this case, the Stokes vector and coherency matrix offer two equivalent alternative representations, and the choice of specific model is the preference of an experimenter and often results from additional considerations. Note, that this choice of light description also predetermines the formalism in the item 4.

The modern optical elements are close enough to ideal. Nevertheless, taking into account their real properties can reduce the errors in final dielectric constant if the main part of these errors is caused by an imperfection of some specific element. In the opposite case, if there is another source of most substantial errors the application of special formalism dealing with imperfections is not necessary, since it does not considerably improve the accuracy of an experiment. A convenient way of handling a real component with a small imperfection is to replace it by a combination of the two elements: its ideal counterpart and the imperfection plate. Such considerations produce the Jones and Müller matrices for imperfect elements, and further description is similar to the ideal case. The second important thing associated with optical elements is their linearity. They should be very close to linear, because, otherwise, the Matrix formalism becomes inapplicable, and it makes the problem of dielectric constant determination very complex. Nowadays, ellipsometry is exclusively based on linear formulae.

To select a correct model of the sample structure requires the additional considerations that can be obtained by other techniques. So, for the newest materials the structure of which is not studied very well, the selection of a correct model is a very difficult task. In this case, one should assume some model based on personal intuition and experience, that makes reliability of results sufficiently doubtful and

questionable. These results and assumptions have to be confirmed. The conventional models are the isotropic reflecting surface described by Fresnel formula, an anisotropic reflection surface, a plane thin plate and others. In general, the problem of reflection on a sample can be described in the frame of classical electrodynamics on the base of Maxwell's equations. This method allows to express the ellipsometric parameters of the sample through its dielectric properties.

It was mentioned above, that Jones vectors completely describe totally polarized light. Therefore, the use of Jones matrices is more appropriate and reasonable for this case since all calculations are presently performed by computers, and  $2 \times 2$  matrices operations generate lesser rounding-off errors than  $4 \times 4$  ones. Furthermore, only two parameters of Stokes vectors and coherency matrix appear to be independent for totally polarized light that makes light description by them oversaturated. If the description of partially polarized light is required, one can use Müller matrices with Stokes vector, or Jones matrices with coherency matrix. These methods are equivalent to each other, and the specific choice comes from additional criteria associated with the specific realization of an experiment.

The items (5), (6) summarize results achieved in previous items and present themselves exclusively as the mathematical problem which can be sufficiently easy solved by methods of linear algebra operates with Jones or Müller matrices. As the result, the real and imaginary part of the dielectric constant of material will be obtained at the frequency of incident light. Errors of this determination can be distinguished to randomized statistical errors that can be reduced by increasing the number of measurements, and model and systematical errors that can not be reduced without a perfection of mathematical model or characteristic of optical elements. The detailed analysis of errors depends on the specific situation and will be considered below for some particular cases.

The last remark I want to mention here is about another condition under which the matrix formalisms can be applied. The restrictions of these methods coincides with limitations of geometry optics that are well known, namely: the beam must be ideally collimated (the beam width much larger than the diffraction length), and the sizes of optical elements must be also much larger than the diffraction length. Furthermore, the media must be homogeneous without spatial and frequency dispersions. If these conditions are not satisfied, one should solve the wave equation for each particular case. For very small samples one should also take into account diffraction coming from wave optics. Under small diffraction

it is possible to introduce first order corrections to the Müller or Jones matrix formalism.

## 1.11 Ellipsometry with imperfect components

## 1.12 Leak of polarizers and depolarization of compensators

### 1.12.1 Polarizer imperfection

A non-ideal polarizer has non-zero transmissions in both straight and perpendicular directions. This imperfection can be characterized by the ratio of minimum and maximum transmissions:

$$\chi = \frac{T_{min}}{T_{max}} \quad (1.52)$$

Using  $\chi$  coefficient in the matrix formalism is the first approximation on the way to describe a real polarizer. It is also possible to introduce the coefficient that response for a phase shift between the two components passed through a polarizer. One can also describe theoretically the heterogeneity of a polarizer structure etc. However, in practice we have always a question how to measure all these coefficients. This limits the number of coefficients that can be introduced. Therefore, in most number of cases one has only one  $\chi$  coefficient to describe the imperfect polarizer. Sometimes, the phase shift coefficient is also applied. This means that all other effects should be much less pronounced with respect to polarizer leak, and this requires the polarizer must be close enough to ideal. For modern polarizers this condition is generally satisfied.

### 1.12.2 Depolarization of compensator

Depolarization effect appears mostly due to light scattering and multiple reflections in a compensator and its heterogeneity. The first approximation in description of these effects is the using the depolarization coefficient:

$$D = \Delta P, \quad (1.53)$$

where  $\Delta P$  is the change of the polarization degree produced by a compensator. This coefficient can be measured quite easily, however it does not describe the depolarization process in details, therefore it can be used just for estimation of this effect. General theory of depolarization is quite complex, and includes so-called depolarization matrix. If the compensator is characterized this way, the complex  $3 \times 3$  matrix must be introduced, and there are no easy ways to measure all elements of this matrix, that limits its application in practice. If depolarization is small that we can virtually broke the compensator to ideal compensator and the virtual element that isotropically depolarizes the light. Then, the depolarization can be described in terms of  $D$  coefficient. Even in this simple case we have 2 compensator parameters  $D$ , and retardation  $\delta$ . Fortunately, they can be calculated with ellipsometry since it has eventually leads to two equations which describes the change of polarization state. Note also, that depolarization can be only described with Müller matrix formalism.

### 1.12.3 Müller matrix theory with imperfections

#### Definition of matrices

Consider the following system of optical elements: the incoming light with degree of polarization  $P_s$  and its polarization state  $(\psi_s, \delta_s)$ ; the polarizer with fixed angle  $\alpha_p$ , transmissions  $A_p, a_p$  and its imperfection  $\chi_p = a_p/A_p$ ; the sample surface with parameters  $\Psi$  and  $\Delta$  and reflectivity  $A_s$ ; the compensator with retardation  $\delta$ , transmission  $A_c$  and depolarization  $D$ ; and the analyzer with transmissions  $A_a, a_a$  imperfection  $\chi_a = a_a/A_a$ . Now, trace out the Müller matrices for these elements. So, the Müller matrix for rotator to the angle  $\alpha$  has the form:

$$\mathbf{M}_{rot} = \begin{pmatrix} 1 & 0 & 0 & 0 \\ 0 & \cos(2\alpha) & \sin(2\alpha) & 0 \\ 0 & -\sin(2\alpha) & \cos(2\alpha) & 0 \\ 0 & 0 & 0 & 1 \end{pmatrix} \quad (1.54)$$

The Müller matrix for partial polarizer with maximum and minimum transmissions  $A$  and  $a$ , and oriented at the angle  $\alpha$ :

$$\mathbf{M}_{par} = \frac{1}{2} \begin{pmatrix} A+a & A-a & 0 & 0 \\ A-a & A+a & 0 & 0 \\ 0 & 0 & 2\sqrt{Aa} & 0 \\ 0 & 0 & 0 & 2\sqrt{Aa} \end{pmatrix} \quad (1.55)$$

Thus, the total matrix for polarizer is  $\mathbf{M}_p = \mathbf{M}_{rot}(\alpha_p)\mathbf{M}_{par}(a_p, A_p)\mathbf{M}_{rot}(-\alpha_p)$  and the similar matrix for the analyzer, with substituted  $A_p \iff A_a$ ,  $a_p \iff a_a$ ,  $\alpha_p \iff \alpha_a$ . The retarder unit is virtually broken to ideal retarder with retardation  $\delta$  and to depolarizing element with depolarization  $D$ . Denote the degree of polarization after compensator as  $P_c = 1 - D$ . The matrix for ideal retarder has a form:

$$\mathbf{M}_{ret} = \begin{pmatrix} 1 & 0 & 0 & 0 \\ 0 & 1 & 0 & 0 \\ 0 & 0 & \cos \delta & \sin \delta \\ 0 & 0 & -\sin \delta & \cos \delta \end{pmatrix}, \quad (1.56)$$

and the matrix of virtual depolarizing element:

$$\mathbf{M}_D = \begin{pmatrix} 1 & 0 & 0 & 0 \\ 0 & P_c & 0 & 0 \\ 0 & 0 & P_c & 0 \\ 0 & 0 & 0 & P_c \end{pmatrix}. \quad (1.57)$$

And the Müller matrix for the sample surface has the following form:

$$\mathbf{M}_{sam} = \frac{1}{2} (r_x^2 + r_y^2) \begin{pmatrix} 1 & -\cos(2\Psi) & 0 & 0 \\ -\cos(2\Psi) & 1 & 0 & 0 \\ 0 & 0 & \sin(2\Psi) \cos \Delta & \sin(2\Psi) \sin \Delta \\ 0 & 0 & -\sin(2\Psi) \sin \Delta & -\sin(2\Psi) \cos \Delta \end{pmatrix} \quad (1.58)$$

### Evaluation of intensity on the detector

Consider the evolution of the Stokes vector using the Müller matrices (1.54, 1.55, 1.56, 1.57, 1.58). The incoming light is generally characterized by the following Stokes vector:

$$\vec{S}_0 = s_0 \begin{pmatrix} 1 - P_s \\ 0 \\ 0 \\ 0 \end{pmatrix} + s_0 P_s \begin{pmatrix} 1 \\ -\cos(2\psi_s) \\ \sin(2\psi_s) \cos \Delta_s \\ -\sin(2\psi_s) \cos \Delta_s \end{pmatrix} \quad (1.59)$$

Then after polarizer we will have the vector  $\vec{S}_1 = \mathbf{M}_{pola} \times \vec{S}_0$ , where  $\mathbf{M}_{pola} = \mathbf{M}_{rot}(\alpha_p) \mathbf{M}_{par}(A_p, a_p) \mathbf{M}_{rot}(-\alpha)$ . Then, after retarder we have  $\vec{S}_2 = \mathbf{M}_D \times \mathbf{M}_{ret} \times \vec{S}_1$ . Then, after the light has reflected upon the sample, its Stokes vector assumes the form  $\vec{S}_3 = \mathbf{M}_{sam} \times \vec{S}_2$ . Further, multiplying to the analyzer matrix  $\mathbf{M}_{ana} = \mathbf{M}_{rot}(\alpha_a) \times \mathbf{M}_{par}(A_a, a_a) \times \mathbf{M}_{rot}(-\alpha_a)$ , we obtain the Stokes vector characterizing the light on the detector. The next step is to extract the intensity of the wave as the first element of the Stokes vector. All these bulky calculations were done with Mathematica 4.1 Software, and eventually the following expression for the intensity has been obtained:

$$J = J_0 (A + B \cos(2\alpha_a) + C \sin(2\alpha_a)), \quad (1.60)$$

where  $J_0 = \frac{1}{4} A_{pola} A_{ret} A_{ana} \sqrt{r_x^2 + r_y^2}$  is the general pre-factor depending on the transmissions  $A_{pol}$ ,  $A_{ret}$ ,  $A_{ana}$ , reflection of a sample  $A_{sam}$ , and the incident light intensity  $s_0$ . Coefficient  $A$ ,  $B$ ,  $C$  are dependent on polarizer angle, imperfections of polarizer and analyzer, depolarization and retardation of the compensator, and  $\Psi$  and  $\Delta$  of the sample. Let us compare the expression (1.60) with the one for ideal case (1.5). Generally, we have the same expression if we take out the factor  $A$  from (1.60). The difference is that  $A$ ,  $B$  and  $C$  are dependent on more number of parameters, namely, there are three additional parameters  $\chi_a$ ,  $\chi_p$  and  $D$ . Since the values  $\chi_a$ ,  $\chi_p$  and  $D$  supposed to be quite small, it was discussed above, we can take into account only first order terms.

**The structure of the free term  $A$  parameter.**

The  $A$  term can be presented as the following sum:

$$A = L_{(a0)} + L_{(aP0)}\sqrt{\chi_p}P_s + L_{(aD)}D + L_{(aPa)}\chi_a + L_{(aPp)}\chi_p, \quad (1.61)$$

where

$$\begin{aligned} L_{(a0)} = & 1 - \cos(2\Psi) \cos(2\alpha_p) + P_s \left[ \cos 2\Psi \cos^2(2\alpha_p) \cos(2\psi_s) - \right. \\ & - \cos \Delta_s \sin(2\alpha_p) \sin(2\psi_s) - \\ & - \cos(2\alpha_p) \cos(2\psi_s) + \\ & \left. + \cos(2\alpha_p) \cos(2\Psi) \cos \Delta_s \sin(2\alpha_p) \sin(2\psi_s) \right], \end{aligned} \quad (1.62)$$

$$L_{(aD)} = \cos(2\Psi) \cos(2\alpha_p) [1 - (\cos(2\alpha_p) \cos(2\psi_s) + \cos \Delta_s \sin(2\alpha_p) \sin(2\psi_s)) P_s], \quad (1.63)$$

$$L_{(aPa)} = 1 - \cos(2\Psi) \cos(2\alpha_p) \quad (1.64)$$

$$L_{(aP0)} = 2 \cos(2\Psi) \sin(2\alpha_p) (\cos(2\psi_s) \sin(2\alpha_p) - \cos(2\alpha_p) \cos \Delta_s \sin(2\psi_s)) \quad (1.65)$$

$$L_{(aPp)} = 1 + \cos(2\Psi) \cos(2\alpha_p) \quad (1.66)$$

**The structure of  $B$  cos term parameter**

This coefficient can also be presented the same way:

$$B = L_{(b0)} + DL_{(bD)} + P_s\sqrt{\chi_p}L_{(bP0)} + \chi_a L_{(bPa)} + \chi_p L_{(bPb)}. \quad (1.67)$$

here

$$\begin{aligned} L_{(b0)} = & \cos(2\alpha_p) - \cos(2\Psi) + P_s [\cos(2\Psi) \cos(2\alpha_p) \cos(2\psi_s) + \\ & + \cos \Delta_s \sin(2\alpha_p) \sin(2\psi_s) \cos(2\Psi) - \cos^2(2\alpha_p) \cos(2\psi_s) - \\ & - \cos(2\alpha_p) \sin(2\alpha_p) \cos \Delta_s \sin(2\psi_s)], \end{aligned} \quad (1.68)$$

$$L_{(bD)} = \cos(2\alpha_p) (-1 + P_s (\cos(2\alpha_p) \cos(2\psi_s) + \cos \Delta_s \sin(2\alpha_p) \sin(2\psi_s))), \quad (1.69)$$

$$L_{(bP0)} = 2 \sin(2\alpha_p) (\cos(2\alpha_p) \cos \Delta_s \sin(2\psi_s) - \cos(2\psi_s) \sin(2\alpha_p)) \quad (1.70)$$

$$L_{(bPa)} = \cos(2\Psi) - \cos(2\alpha_p) \quad (1.71)$$



$$L_{(bPp)} = -(\cos(2\Psi) - \cos(2\alpha_p)) \quad (1.72)$$

### The structure of $C$ sin term

General structure is the same:

$$C = L_{(c0)} + DL_{(cD)} + P_s\sqrt{\chi_p}L_{(cP0)} + L_{(cPa)}\chi_a + L_{(cPp)}\chi_p \quad (1.73)$$

the structure of  $L$  coefficients is follows:

$$\begin{aligned} L_{(c0)} = & \sin(2\Psi) \sin(2\alpha_p) [\cos \delta \cos \Delta - \sin \delta \sin \Delta - \\ & - P_s \cos \delta \cos \Delta (\cos(2\alpha_p) \cos(2\psi_s) + \cos \Delta_s \sin(2\alpha_p) \sin(2\psi_s)) + \\ & + P_s \sin \delta \sin \Delta (\cos(2\alpha_p) \cos(2\psi_s) + \cos \Delta_s \sin(2\alpha_p) \sin(2\psi_s))] \end{aligned} \quad (1.74)$$

$$\begin{aligned} L_{(cD)} = & \cos(\delta + \Delta) \sin(2\Psi) \sin(2\alpha_p) (-1 + P_s \cos(2\alpha_p) \cos(2\psi_s) + \\ & + P_s \cos \Delta_s \sin(2\alpha_p) \sin(2\psi_s)) \end{aligned} \quad (1.75)$$

$$\begin{aligned} L_{(cP0)} = & 2 \sin(2\Psi) \cos \Delta_s \sin(\delta + \Delta) \sin(2\psi_s) + 2 \sin(2\Psi) \cos(\delta + \Delta) \cos(2\alpha_p) \times \\ & \times (\cos(2\psi_s) \sin(2\alpha_p) - \cos(2\alpha_p) \cos(\Delta_s) \sin(2\psi_s)) \end{aligned} \quad (1.76)$$

$$L_{(cPa)} = -\cos(\delta + \Delta) \sin(2\Psi) \sin(2\alpha_p) \quad (1.77)$$

$$L_{(cPp)} = -\cos(\delta + \Delta) \sin(2\Psi) \sin(2\alpha_p) \quad (1.78)$$

### Analysis of term structure

The  $A$ ,  $B$  and  $C$  terms have the similar structures expressed by formulae (1.61), (1.67), (1.73), i.e. there is a free term independent on an imperfection coefficient, there is also the term proportional to the square root of polarizer imperfection  $\chi_p$  times to polarization degree of the source  $P_s$ , the next term is proportional to depolarization of a compensator  $D$ , and the last two terms are proportional to polarizer and analyzer imperfections  $\chi_p$  and  $\chi_a$  correspondingly. If any term is much less the other terms, it can be excluded from consideration. So if  $P_s\sqrt{\chi_p} \ll \chi_p$ , the term proportional to  $P_s\sqrt{\chi_p}$  can be neglected, and we can exclude polarization of the source in that way. The condition can be rewritten in the form:

$$P_s \ll \sqrt{\chi_p} \quad (1.79)$$

Thus, if the incoming light is depolarized enough to satisfy 1.79, one can leave only terms proportional to  $\chi_a$ ,  $\chi_p$ . In the other case, if the degree of polarization

of incoming light is high, one can leave only the term proportional to  $\sqrt{\chi_p}$ . Furthermore, if the imperfections  $\chi_p$  and  $\chi_a$  are in the same order of magnitude, the parameter  $\chi_a$  is completely excluded from the consideration.

The second important conclusion, that follows from formulae (1.61), (1.67), (1.73), is that the effects coming from depolarization can be considered independently on the effects associated with polarizers, since the term with depolarization  $D$  contains no polarizer leak parameters  $\chi_a$  and  $\chi_b$ .

#### 1.12.4 Method to measure polarizer imperfections using a totally depolarized source

Let a polarizer and an analyzer have approximately the same leak parameter  $\chi$ . Dispose these elements straight forward as shown in Fig. 1.12.4: Now, confront

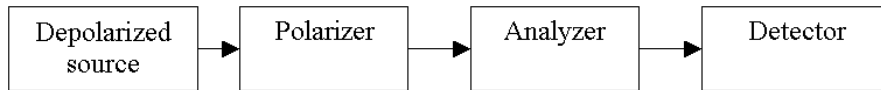


Figure 1.10: Optical scheme to measure  $\chi$  coefficient.

the polarizers to their Müller matrices according to 1.55, i.e the matrices will have the form:

$$\mathbf{M}_{par} = \frac{1}{2}A \begin{pmatrix} 1 + \chi & 1 - \chi & 0 & 0 \\ 1 - \chi & 1 + \chi & 0 & 0 \\ 0 & 0 & 2\sqrt{\chi} & 0 \\ 0 & 0 & 0 & 2\sqrt{\chi} \end{pmatrix}, \quad (1.80)$$

where  $A$  is the transmission of polarizer. The Stokes vector on a detector is given by the formula:

$$\vec{S} = \mathbf{M}_{rot}(\alpha_p) \times \mathbf{M}_{par} \times \mathbf{M}_{rot}(-\alpha_p) \times \mathbf{M}_{rot}(\alpha_a) \times \mathbf{M}_{par} \times \mathbf{M}_{rot}(-\alpha_a) \times \vec{S}_0,$$

where  $\mathbf{M}_{rot}(\alpha)$  is the Müller matrix for rotator given by 1.54,  $\alpha_p$ ,  $\alpha_a$  are respectively the angles of the polarizer and analyzer, and  $\vec{S}_0 = \{J_0, 0, 0, 0\}$  is the Stokes vector of the totally depolarized incoming light. If one has completed this

calculation, the following formula for relative intensity is obtained:

$$J/J_0 = 1 + \frac{(\chi - 1)^2}{(\chi + 1)^2} \cos \{2(\alpha_a - \alpha_p)\} \quad (1.81)$$

Note, that the power series of this formula is  $\frac{(\chi-1)^2}{(\chi+1)^2} = 1 - 4\chi + O[\chi^2]$ . It allows to estimate the error due to linear approximations:

$$\epsilon = \frac{A_{nl} - A_{ln}}{A_{nl}} \simeq 8\chi^2, \quad (1.82)$$

where  $A_{nl} = \frac{(\chi-1)^2}{(\chi+1)^2}$ , and  $A_{ln} = 1 - 4\chi$ . So, if the value of  $\chi$  is about 1%, that formulae (1.61), (1.67), (1.73) contains the model error about 0.1%, for  $\chi = 5\%$  - the error is 2%. It means that linear approximation works only for small  $\chi$ . This error is equal to  $\chi$  at  $\chi = 12.5\%$ .

### Estimation of minimal value is possible to measure with this method

Take the  $\chi$  derivative of the (1.81):

$$\frac{d(J/J_0)}{d\chi} = \frac{4(\chi - 1) \cos [2(\alpha_a - \alpha_p)]}{(1 + \chi)^3} \quad (1.83)$$

The absolute value of the derivative (1.83) is maximal at  $\cos [2(\alpha_a - \alpha_p)] = \pm 1$ . Then the (1.81) assumes the form:

$$J/J_0 = 1 + \frac{(\chi - 1)^2}{(\chi + 1)^2} \quad (1.84)$$

Now, make the Taylor expansion and take into account noise  $N$ :

$$J/J_0 = 1 - 2\chi + N + O[\chi^2] \quad (1.85)$$

Looking at (1.85), the criteria for minimal  $\chi$  can be obtained:

$$\chi \geq N/2 \quad (1.86)$$

### 1.12.5 Measurement of depolarization parameter

#### Formulation of the problem

Consider the set of optical elements schematically presented in Fig. 1.12.5. There

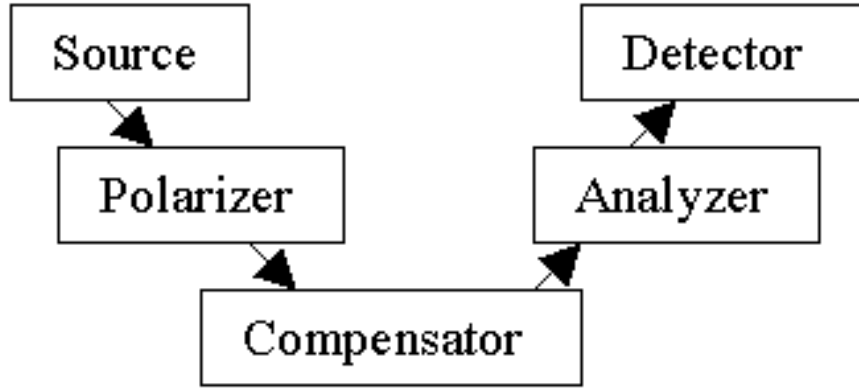


Figure 1.11: Optical scheme to measure depolarization of the compensator.

is a source (exactly the light before polarizer) characterized by its degree of polarization  $P_s$ , and by  $\Psi_s, \Delta_s$  which characterize the polarization ellipse. Then, there is a polarizer with the leak coefficient  $\chi_p$ , oriented at the angle  $\alpha_p$ . Next element is a compensator. Consider it more detail. In fact, the compensator represents itself a prism plus some mirrors for alignment the beam. As generally known, the reflection upon a mirror change the polarization state of light, therefore we should introduce the Müller matrix to describe these features of our compensator as well as the depolarization of the prism. One option to do it is to substitute the compensator with mirrors to virtual sample. It extends the concept of compensator. Now, the compensator is not only the prism, but also the mirrors. To take into account the depolarization, one should mathematically multiply the Müller matrix for a sample with parameters  $\Psi_{com}$  and  $\Delta$  (see formula 1.58) to the Müller matrix for depolarizing element see formula 1.57). Eventually, the matrix for compensator  $\mathbf{M}_{com}$  has the following form:

$$\begin{pmatrix} 1 & -\cos(2\Psi_{com}) & 0 & 0 \\ -\cos(2\Psi_{com}) & 1 - D_{com} & 0 & 0 \\ 0 & 0 & (1 - D_{com}) \sin(2\Psi_{com}) \cos(\Delta_{com}) & \sin(2\Psi_{com}) \sin(\Delta_{com}) \\ 0 & 0 & -\sin(2\Psi_{com}) \sin(\Delta_{com}) & (D_{com} - 1) \sin(2\Psi_{com}) \cos(\Delta_{com}) \end{pmatrix}$$

After the compensator, there is an unperfect analyzer characterized by the leak  $\chi_a$ , and the angle  $\alpha_a$ .

### Detected intensity in general case

As usual, the relative intensity can be written as follows:

$$J/J_0 = A + B \cos(2\alpha_a) + C \sin(2\alpha_a), \quad (1.87)$$

where all coefficients has the similar structure, namely:

$$A = A_0(\Psi_{com}, \Delta_{com}, D_{com}, \alpha_p) + A_1(\Psi_{com}, \Delta_{com}, \alpha_p, D_{com}, \chi_a, \chi_p) + \\ + P_s A_2(\Psi_{com}, \Delta_{com}, \alpha_p, D_{com}, \chi_a, \chi_p, \Psi_s, \Delta_s) \quad (1.88)$$

### The case of depolarized incoming light

For depolarized source, the coefficients  $A$ ,  $B$ ,  $C$  assume the form:

$$A = (1 + \chi_a)(1 - \cos(2\alpha_p) \cos(2\Psi_{com}) + \chi_p(1 + \cos(2\alpha_p) \cos(2\Psi_{com}))) \quad (1.89)$$

$$B = (\chi_a - 1)(\cos(2\alpha_p) - \cos(2\Psi_{com})) + \\ + D_{com}(\chi_p - 1)\cos(2\alpha_p) - \chi_p(\cos(2\alpha_p) + \cos(2\Psi_{com})) \quad (1.90)$$

$$C = (D_{com} - 1)(\chi_a - 1)(\chi_p - 1)\cos(\Delta_{com})\sin(2\alpha_p)\sin(2\Psi_{com}) \quad (1.91)$$

### The case of ideal polarizers

In this case, the coefficients assume simplest form:

$$A = 1 - \cos(2\alpha_p) \cos(2\Psi_{com}) \quad (1.92)$$

$$B = (1 - D_{com}) \cos(2\alpha_p) - \cos(2\Psi_{com}) \quad (1.93)$$

$$C = (D_{com} - 1) \cos \Delta_{com} \sin(2\alpha_p) \sin(2\Psi_{com}) \quad (1.94)$$

The important thing is to estimate the minimal possible value of  $D_{com}$  which is possible to detect. First, set approximate values of  $\Delta_{com} \approx 0$ , and  $\Psi_{comp} \approx \pi/4$ . These are the typical values for compensators used in our ellipsometry setup. Then  $D_{com}$  derivative of (1.87) assumes the following form:

$$\frac{d(J/J_0)}{dD_{com}} = -\cos[2(\alpha_a + \alpha_p)] \quad (1.95)$$

It has maximum absolute value 1. Then, at  $\alpha_a = \alpha_p = 0$  (1.87) has the form:

$$J/J_0 = 1 - \frac{1}{2}D_{com} + N, \quad (1.96)$$

where  $N$  is the noise term. And the criteria for  $D_{com}$  is follows:

$$D_{com} \geq 2N \quad (1.97)$$

## 1.13 Analysis of ellipsometric data

### 1.13.1 Anisotropy correction

High temperature superconductors (HTSC) are anisotropic materials where optical conductivity in CuO planes is much higher than along c-axis perpendicular to the planes. In this case the dielectric constants given by 1.4 are, so called, pseudo-dielectric constants and to obtain the real constants one has to apply so-called anisotropy correction. In the case of anisotropic media the complex refractive indexes are given by the formulas:

$$r_{pi} = \frac{\sqrt{\varepsilon_k \varepsilon_i} \cos \Phi - \sqrt{\varepsilon_k - \sin^2 \phi}}{\sqrt{\varepsilon_k \varepsilon_i} \cos \Phi + \sqrt{\varepsilon_k - \sin^2 \phi}}, \quad (1.98)$$

$$r_{si} = \frac{\cos \Phi - \sqrt{\varepsilon_j - \sin^2 \phi}}{\cos \Phi + \sqrt{\varepsilon_j - \sin^2 \phi}}, \quad (1.99)$$

where  $i, j, k = abc$  index the axes of a crystal. In the case of uniaxial crystals two axes are equal, for biaxial crystals all three axes are different. On the other hand the ellipsometry measures the complex ratio of  $r_p/r_s$  for different crystal orientation. After that one can make a fit of ellipsometric data with 1.99 and obtain the real dielectric constants for anisotropic material. This fit is very complex, can not be analytically solved, and has multiply solutions. The choice of real solution is often made by the intuition of an experimentalist. In the figure 1.12 the corrected and uncorrected spectra are presented. For most of HTSC their c-axis spectrum is not changed to much by the correction procedure. However, changes of in-plane spectra are significant, and the correction must be obligatorily applied. The reason for that is that the in plane conductivity is many times larger than the c-axis one.

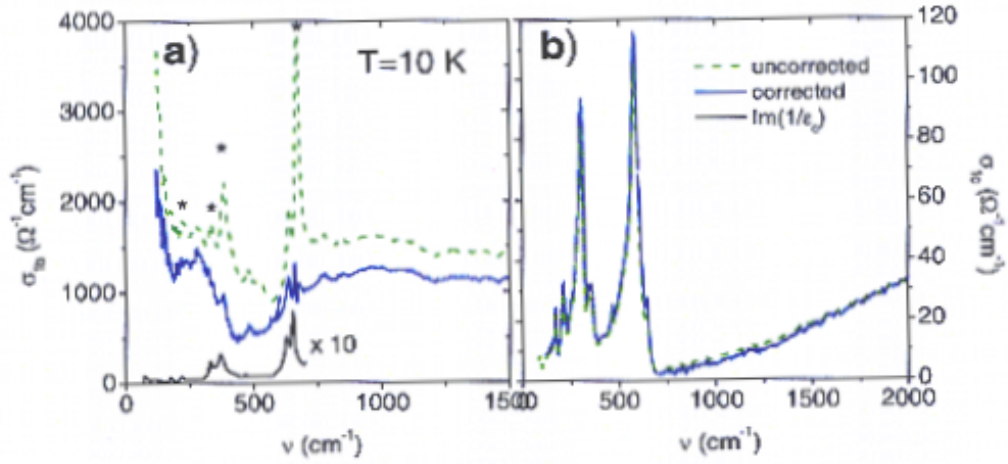


Figure 1.12: Effect of anisotropy correction on the b-axis (fig a) and c-axis (fig b) spectrum of a  $Bi_2Sr_2CaCu_2O_{8+\delta}$  single crystal.[10]

### 1.13.2 Diffraction correction

Diffraction effects become important if the wavelength is comparable with the cross-section of a sample. If one measures a sample about  $0.1mm$  size at an angle of incidence of 85 degrees the diffraction has to be taken into account below  $100\text{ cm}^{-1}$ . To correct our data we use the correction based on the classical problem of reflection from a half-plane. The contributions from the front sample side and from the flanks are taken into account. As was shown in [11] the classical problem of the diffraction on the half-plane has the approximate solution, which can be represented by the Hankel functions, and close to numerical solution of Maxwell's equations for this case. The contribution of the diffraction from the sample surface to s and p-polarized field components is plotted in fig. 1.13 for the angle of incidence 85 degrees. It is necessary to note that these calculations were made for the a case of perfect conductor. The correction we use is still quite approximate and needs to be improved in future. It does not take into account the contribution from the flank sides of the sample properly. So far it is done phenomenologically and the results has to be checked after applying the correction. The program algorithm is follows: first the ratio of an effective sample size to the wavelength is calculated. Then, the program reads numerical solution for the diffraction upon the half-plane at the angle of incidence 85 degrees. After that, this solution is

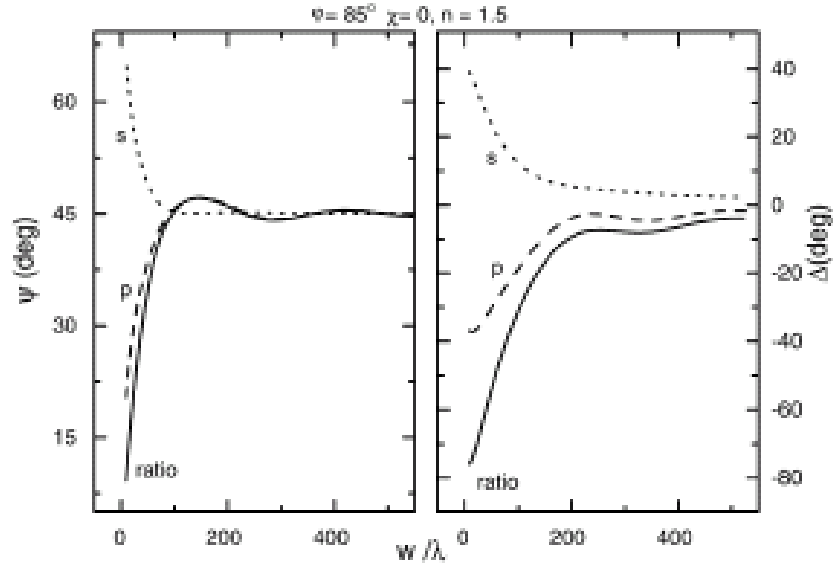


Figure 1.13: Effect of anisotropy correction on the b-axis (fig a) and c-axis (fig b) spectrum of a  $Bi_2Sr_2CaCu_2O_{8+\delta}$  single crystal.[10]

corrected for another angle of incidence using phenomenological formula. Finally, the ellipsometric parameters  $\Psi$  and  $\Delta$  are corrected.

### 1.13.3 Properties of optical conductivity

Consider the complex conductivity  $\sigma(\omega) = \sigma_1 + i\sigma_2$ . First, the conductivity is a response function, therefore:

$$\sigma(-\omega) = \sigma^*(\omega). \quad (1.100)$$

Second, from the causality principle we have the Kramers-Kronig (KK) relations:

$$\sigma_1(\omega) = \frac{2}{\pi} P \int_0^\infty \frac{\omega' \sigma_2(\omega')}{\omega'^2 - \omega^2} d\omega' \quad \sigma_2(\omega) = -\frac{2\omega}{\pi} P \int_0^\infty \frac{\sigma_1(\omega')}{\omega'^2 - \omega^2} d\omega' \quad (1.101)$$

The combination of KK relations with physical arguments about the behavior of optical conductivity conducts us to the sum-rule expression. Although the sum rule expression is general, the most widely used form of it is based on the Drude model and can be written in the form:

$$\int_0^\infty \sigma_1(\omega) d\omega = \frac{\pi N e^2}{2m} = \frac{\omega_p^2}{8}, \quad (1.102)$$



where  $N$  is the number of electrons per unit volume,  $e$  and  $m$  are the charge and the mass of electron,  $\omega_p$  is the plasma frequency of the Drude model. Normally the integration is taken to a final frequency and we can introduce the quantity:  $N_{eff}(\omega) = \frac{2mV}{\pi e^2} \int_0^\omega \sigma_1(\omega) d\omega$ . The upper integration limit is usually taken between the plasma frequency and the inter-band transition frequencies. At the end, note the basic properties of real conductivity, which come from its definition:

$$\sigma_1(\omega) > 0, \quad \lim_{\omega \rightarrow 0} \sigma_1(\omega) = \sigma_{DC}. \quad (1.103)$$

### 1.13.4 Drude-Lorentz model of optical conductivity

In Drude-Lorentz model it is assumed that an electron bound with the nucleus as a harmonic oscillator. The equation of motion is  $m\ddot{\vec{r}} + m\Gamma\dot{\vec{r}} + m\omega_0\vec{r} = -e\vec{E}$ . Starting from here one can derive the following formulae for the optical conductivity:

$$\sigma(\omega) = \frac{\omega_p^2}{4\pi} \frac{\omega}{i(\omega_0^2 - \omega^2) + \Gamma\omega} \quad (1.104)$$

For free electrons  $\omega_0 = 0$  since they are not bound. For fitting of complex dielectric function the following expression is normally used:

$$\varepsilon(\omega) = \varepsilon_\infty - \frac{\omega_p^2}{\omega(\omega + i\Gamma)} + \sum_j \frac{\omega_{p,j}^2}{(\omega_{0,j}^2 - \omega^2) - i\omega\Gamma_j}, \quad (1.105)$$

where  $\varepsilon_\infty$  is the value of the dielectric function at  $\omega \rightarrow \infty$ . In two particular cases the Drude contribution can be asymptotically simplified: if  $\omega \ll \Gamma$  then  $\sigma_1 \simeq \omega_p^2/4\pi\Gamma$ ,  $\varepsilon_1 \rightarrow -\infty$ ; if  $\Gamma \ll \omega \ll \omega_p$  then  $\sigma_1 \simeq \omega_p^2\Gamma/4\pi\omega^2$ ,  $\varepsilon_1 \simeq -\omega_p^2/\omega^2$ . For many practical cases the Drude-Lorentz model is not good enough to fit experimental data. Therefore, several extensions of this model have been introduced. The first of them was proposed by D. van der Marel [12]:

$$\sigma(\omega) = \frac{\omega_p^2}{4\pi} \frac{i}{(\omega + i\gamma)^{1-2\nu}(\omega + i\Gamma)^{2\nu}} \quad (1.106)$$

The second possible extension of Drude model is the introduction of a frequency dependent scattering rate  $\Gamma(\omega)$  in ordinary Drude-Lorentz formula 1.105. To fit asymmetric phonon modes one uses a modified Lorentzian, which is a mixture of

the real and the imaginary parts of the ordinary Lorentzian:

$$\varepsilon(\omega) = S \frac{\omega_0^2 + i\Gamma Q}{(\omega_0^2 - \omega^2) - i\omega\Gamma}, \quad (1.107)$$

where  $Q$  is the, so-called, asymmetry factor.

All of these formulas, which are used for fitting raw experimental data, should satisfy the KK relations in order to represent the dielectric constants. With ellipsometry data one can use both the real and imaginary parts of dielectric constant as the input data for a fit procedure. Results of the fit are strongly dependent on the seed value selected for the fit algorithm. The proper choice of the seed can be taken mostly intuitively after several attempts. The criteria of correct choice is, for example, the fact that asymmetry factor should be small enough, because a large factor has no physical meaning. The second problem with fitting is that for some materials it is difficult to describe the electronic background with a formula, and the data include this background. This fact introduces some uncertainties in separating phonons from the background.

## 1.14 Summary

In conclusion, ellipsometry has an advantage in the accuracy of the measured dielectric constant, compared with conventional spectroscopy. However, it requires additional complexity of the setup and requires more perfect optical elements than ordinary spectroscopy. Therefore, both techniques have their own areas of application. Ellipsometry is needed for high accuracy measurements, and the ordinary spectroscopy is better to solve problems, which do not require such a high accuracy.

# Chapter 2

## Infrared properties of HTSC

### 2.1 Introduction

Infrared spectroscopy has provided valuable information about the electronic properties of conventional superconductors, which are described by the BCS theory [13]. It is known that a superconductor behaves like a perfect conductor (and thus reflector) at frequencies below about twice the superconductive energy gap,  $\Delta$ . At higher frequencies the reflectivity closely resembles the one in the normal metallic state. Infrared and microwave spectroscopy thus allow one to identify the energy scale of the superconductive gap [14]. The second very successful application of infrared spectroscopy for the case of conventional superconductors concerns the study of the Gamma-point phonon modes which reveal information about the lattice vibrations and their coupling to the electrons which mediates the pairing in these conventional superconductors [120, 121].

The high temperature superconductors (HTSC) exhibit a number of properties that make them rather different from the conventional superconductors. One characteristic feature is their pronounced structural anisotropy which is reflected in a corresponding anisotropy of most of their physical properties. For instance the conductivity along the metallic quasi-two-dimensional  $CuO_2$  layers can be orders of magnitude higher (depending on the particular compound) than the one in the perpendicular direction (the c-axis).

The in-plane resistivity of HTSC is linear over a large temperature interval. The linearity is often taken as a measure of good sample quality. The out-of plane resistivity is also linear at high temperature while towards low temperature it often exhibits a steep upturn and thus has a tendency toward semiconducting

like behavior. In YBCO the T-dependence of the c-axis conductivity strongly varies as a function of the oxygen concentration. The c-axis resistivity is very high and semiconductor like in deoxygenated samples while it decreases and acquires a metallic T-dependence in fully oxygenated ones. The order of magnitude of the c-axis resistivity strongly varies from compound to compound which indicates that it strongly depends on the properties of the insulating blocking layer. In contrast, the magnitude and the metallic T-dependence of the in-plane resistivity compare rather well for the various HTSC compounds. This has led to the suggestion that they are governed by the metallic  $CuO_2$  planes which are the common structural element of all the cuprate HTSC compounds.

Infrared spectroscopy once more has proven to be a suitable technique that yields information about the charge dynamics in the cuprate HTSC. The experimental spectra contain clear signatures of spectral gap features in the superconductive as well as in the normal state. The latter is commonly associated with the so called pseudo-gap (PG) effect that is discussed in more detail later on. The infrared studies also have provided clear evidence for pronounced phonon anomalies in the vicinity of the SC transition. Furthermore, the infrared spectra contain sharp features which can be associated with the onset of Josephson currents between the weakly coupled superconductive  $CuO_2$  layers. As discussed in detail in section 2.4 these effects are particularly pronounced in compounds that contain more than one  $CuO_2$  layer per unit cell. Finally, by combining IR spectroscopy with optical spectroscopy in the visible range one can obtain valuable information about the T-dependence of the free carrier spectral weight and thus on the variation of the quasi-particle kinetic energy using the ratio:  $SW = \pi e^2 a^2 \langle -K \rangle / 2\hbar^2 V_a$ , where  $SW$  is the spectral weight,  $V_a$  is the unit cell volume,  $a$  is the lattice constant,  $K$  is the kinetic energy.

## 2.2 Structure and phase diagram of HTSC

A characteristic feature of the cuprate HTSC is their pronounced structural anisotropy. Their layered structure is comprised of quasi-two dimensional  $CuO_2$  layers that are separated by various kinds of mostly insulating metal-oxide layers. All cuprate HTSC compounds contain at least one  $CuO_2$  plane per unit cell. According to the number of closely spaced  $CuO_2$  layers per unit cell they are termed

as single, double, triple, layer compounds, etc. The metallic  $CuO_2$  layers are often called conduction layers whereas the blocks in between them mostly act like insulating spacer layers and charge reservoirs. In fact, a suitable charge transfer from the charge reservoir layer to the  $CuO_2$  planes is required for high  $T_c$  superconductivity to occur in these cuprate compounds (see phase diagram in fig. 2.2).

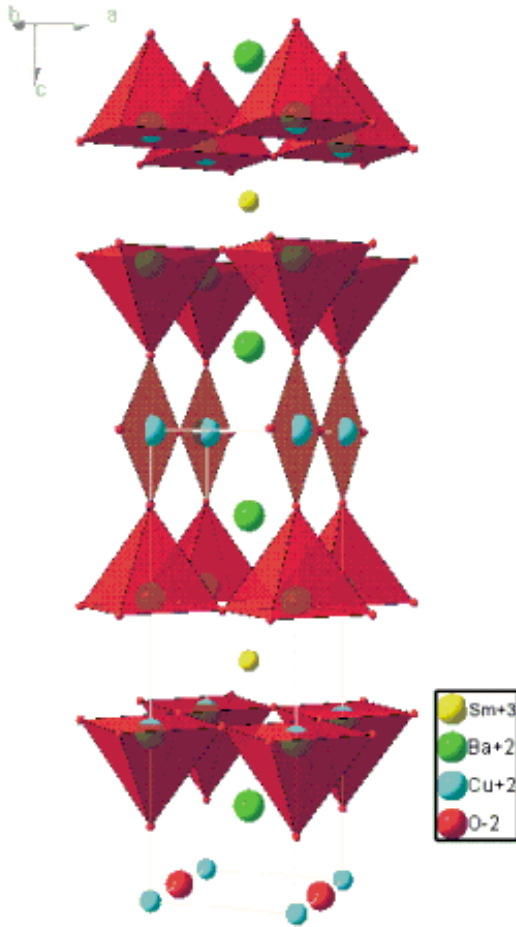


Figure 2.1: Structure of  $Sm123$ .

The 123 compounds as shown in fig. 2.1 exhibits an additional structural feature which is the so-called  $Cu - O$  chains that extend along the b-axis direction. These  $CuO$  chains not only lead to an in-plane orthorhombic structural distortion but also give rise to a pronounced electronic and magnetic in-plane anisotropy. The  $CuO_2$  planes consist of  $CuO_5$  pyramids whose bases are connected via their corner oxygens to form the  $CuO_2$  planes. Via the so-called apical oxygens, they are connected with the  $CuO$  chains that extend along the b-axis direction. Our flux-grown crystals [51] exhibit in the as-grown state extensive twin domains where the direction of the elongated b-axis rotates by 90 degree in the domain walls. It means that  $a$  and  $b$  directions are not ordered in the whole crystal and one measures an average response from the  $ab$  plane.

To measure the individual response of the  $a$  or  $b$  axes the crystal, therefore, must be de-twined. De-twinning can be achieved by simultaneous application of heat and uniaxial stress [15].

In the course of this thesis we will present experimental data on various modifications of the 123 compounds where particular cations have been fully or partially replaced by others. For instance, the Y123, Sm123, and Nd123 compounds differ only concerning the RE-ions at the Y-site which is located in between the two

closely spaced  $CuO_2$  layers (see fig. 2.1). The slightly different ionic radius of the rare earth, RE+3 ions gives rise to slight differences in the spacing between the  $CuO_2$  layers as well as in the charge transfer between the CuO chains and  $CuO_2$  planes. Thus a somewhat higher oxygen content in the CuO chains is required for Nd-123 as compared to Y123 in order to obtain the same hole doping state within the  $CuO_2$  planes. While these variations are rather small and hardly influence the characteristic electronic properties that will be reported in this thesis, there are two major effects that turn out to be relevant. Firstly, the larger RE ions like Nd and Sm slightly expand the  $CuO_2$  planes and thus enable the incorporation of a much higher concentration of substitutional impurities into the  $CuO_2$  planes like Zn and Ni. This effect turns out to be very important in the context of the present work. The second important feature concerns the value of the Josephson-plasma frequency corresponding to the closely spaced  $CuO_2$  layers which is considerably lower (at a corresponding doping state) for Nd-123 and Sm-123.

The hole concentration of the  $CuO_2$  planes can be altered by various means. For instance, by annealing a crystal in a defined oxygen atmosphere and temperature (with subsequent rapid quenching) one can vary the oxygen content in the chains over the range of  $\delta$  from 0 to 1. Such a change in the oxygen content leads to a corresponding change of the hole content in  $CuO_2$  plane. A second possibility to change the hole content is the partial substitution of  $Y^{3+}$  with  $Ca^{2+}$  which will increase the hole content in CuO planes. Extensive studies of the variation of the electronic properties have resulted in an empiric formula that connects the hole content with the value of  $T_c$  in the framework of a parabolic law [122, 124, 123].

The phase diagram as a function of the hole content of the  $CuO_2$  planes is sketched in fig. 2.2. In the non-doped state, e.g. in  $YBa_2Cu_3O_6$ , the material is a Mott-insulator with an anti-ferromagnetic ground state. The Néel temperature is in excess of 300K. Already a hole content of around 2-3% is sufficient to break the long-range anti-ferromagnetic order, and a transition to a so-called spin glass state occurs. This can be interpreted in terms of a quantum phase transition[18]. Above a hole concentration of about 6% superconductivity first appears. The critical temperature first increases with hole content in the underdoped regime before it saturates at the maximum transition temperature  $T_c$  at optimum doping of around 15 – 20%. Towards even higher hole content the critical temperature decreases again. Accordingly, this is called the overdoped

region of the phase diagram. While the SC dome appears to be rather symmetric with respect to optimum doping, the normal state electronic properties differ dramatically between the underdoped and the overdoped side of the phase diagram. The normal state properties above  $T_c$  in the under-doped compounds are dominated by the so called pseudo-gap (PG) phenomenon whose origin is presently unknown and the subject of intense studies. The PG transition manifests itself as a gradual suppression of the low energy spin and charge excitation spectrum. The (usually rather ill-defined) onset temperature is denoted as  $T^*$ .

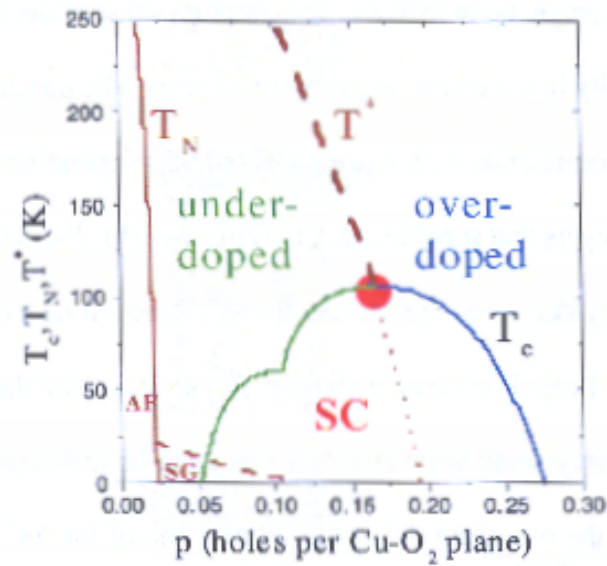


Figure 2.2: Phase diagram of Y123[10].

The presence of a phase transition at  $T^*$  is still under controversial discussion. To the contrary, on the overdoped side of the phase diagram, the normal state properties can be rather well described in the framework of a Fermi liquid model. The crossover occurs near optimum doping where the linear  $T$  dependency of the resistivity is observed that extends over an extremely wide  $T$ -range. Various theoretical models have been proposed in order to account for this transition from a Fermi-liquid like state on the overdoped side, to the underdoped state with a normal state pseudogap. The scenario of a quantum critical point, probably corresponding to a superconductor to metal phase transition, was proposed to explain the rather rapid and unusual changes near optimum doping [18]. Others have proposed a so-called stripe phase model, where the mobile charge carriers segregate forming quasi-one dimensional hole rich stripes that are separated by hole poor regions where AF correlations are restored. The characteristic size of these regions is a few lattice constants [20]. Amongst many other discussed issues are the existence of charge- or spin density wave phases (CDW and SDW) [21, 22]. Most of the properties in the superconductive state can be understood in the framework of the BCS theory with singlet pairing and with a  $d_{x^2-y^2}$  symmetry of the order

parameter and thus of the energy gap[19] in k-space. However, the mechanism mediating the pairing is still not established. Due to the d-wave symmetry where the order parameters changes its sign in k-space at the so-called nodes, the SC state is rather sensitive to structural defects that give rise to potential scattering. The subsequent mixing of states in k-space leads to destructive interference effects in the vicinity of the gap nodes which correspondingly give rise to strong pair-breaking effects even in the presence of non-magnetic impurities. Additional dramatic effects thus occur when the  $Cu^{2+}$  ions are partially substituted by different kind of impurities  $Ni$ ,  $Zn$ , or  $Co$ . These impurities within the  $CuO_2$  planes give rise to strong potential scattering of the charge carriers and a subsequent strong suppression of superconductivity. The effect of these impurities on the superconductive properties is the subject of intensive studies and also the main subject of the present thesis.

## 2.3 In-plane infrared properties

The in-plane dielectric constants of a slightly overdoped ( $T_c = 91K$ ) de-twinned Y123 crystal are plotted in fig 2.3.

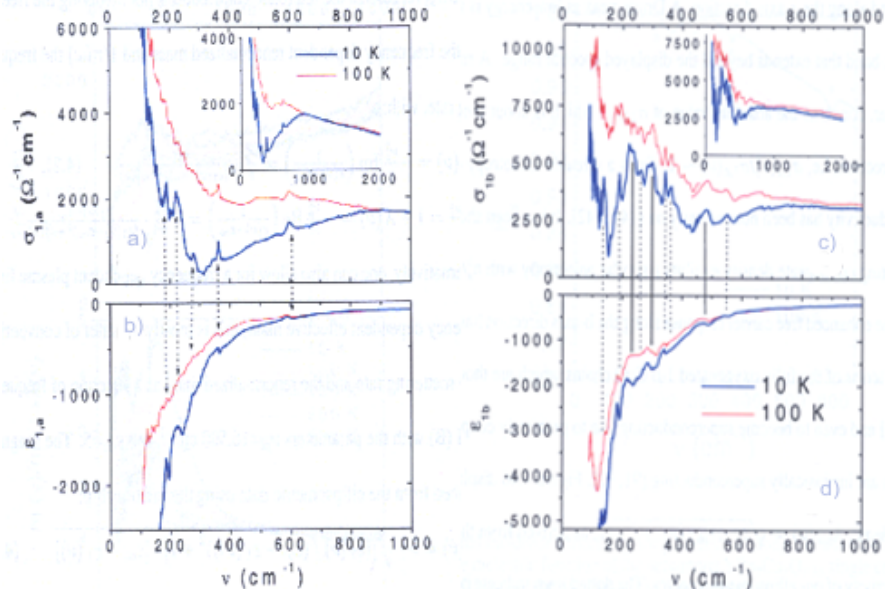


Figure 2.3: In-plane dielectric constants of detwinned  $YBa_2Cu_3O_{6.95}$  (close to optimally doped  $T_c = 91.5K$ ); a-axis (fig. a, b), b-axis (fig. c, d).[10]



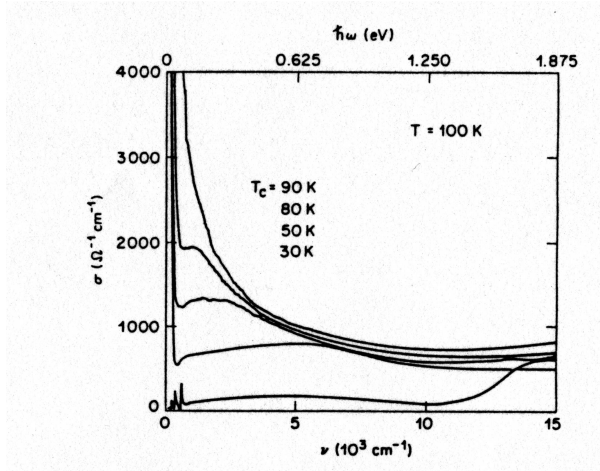


Figure 2.4: Optical inplane conductivity of five twinned  $YBa_2Cu_3O_{7-\delta}$  crystals measured by reflectivity [23].  $\delta$  varies from 0.8 for the lowest curve to 0 for the highest.

First, we consider the spectrum of the a-axis conductivity which contains several characteristic features. In the normal state, there is a pronounced Drude peak near the origin which evolves continuously into a broad so-called MIR band that extends to much higher energy as high as 1 eV. Both of these features have been seen with conventional reflectivity technique as well [23, 24], and several models have been proposed [25] which can be divided into two classes: in the context of the so called one component approach it is assumed that

both the Drude peak and the MIR band arise from the same kind of excitation due to charge carriers that experience strong inelastic scattering due to the interaction with some other kind of excitations like magnons or phonons. The two component approach assumes that the Drude-peak and the MIR band arise from different kinds of excitations of the charge carriers. The MIR band for example has been assigned to polaronic effects. For more details we refer to [10, 25, 26]. The ellipsometric spectra also reveal several weak phonon features in the normal state that are nevertheless well resolved in the real and imaginary parts of the dielectric function. In the superconductive state the spectra exhibit a number of characteristic changes. The most pronounced one in the a-axis spectrum is the broad dip with a minimum in the conductivity around  $350\text{cm}^{-1}$ . When first observed, this dip feature was associated with the superconductive energy gap, i.e. it was interpreted in the framework of the so-called dirty limit for  $\Gamma \gg 2\Delta$ , where  $\Gamma$  is the scattering rate of the free carriers, and  $\Delta$  is the superconductive gap. However, later on it was realized that the in-plane response of the HTSC corresponds to the opposite case of the so-called clean limit [27], i.e. the SC coherence length of about  $25\text{\AA}$  is significantly shorter than the mean free path of the carriers of about  $100\text{\AA}$  as deduced from the dc conductivity above  $T_c$ . Since then, two other interpretations have been suggested. Within two component model it

was suggested that the dip feature is not related to the superconductivity directly. Simply, the onset of the MIR band becomes visible when the Drude-peak collapses below  $T_c$  its SW being transferred to the delta function at the origin. Within the one component approach the dip feature has been interpreted in terms of inelastic scattering on some kind of bosonic mode like for instance the spin fluctuations [28].

The main electronic features in the b-axis spectra for the IR range are similar to the a-axis ones except for the absolute value of the conductivity which is about two times higher, and the broad electronic mode around  $260\text{cm}^{-1}$  which has a very large spectral weight. The origin of this broad mode is not established yet. Some interpretation of this mode can be found in [29]. It was claimed that this mode is resulting from some kind of bridging effect either between planes and chains or between chains [29]. Meanwhile, a similar feature around  $270\text{cm}^{-1}$  has been observed also in the  $\text{Bi}_2\text{Sr}_2\text{CaCu}_2\text{O}_{8+\delta}$  compound, which contains no  $\text{CuO}$  chains [10]. In addition to the broad electronic features, the ellipsometric b-axis spectra also contain a surprisingly large number of narrow peaks, which correspond to IR-active phonon modes. Note that these modes are very difficult to detect in conventional reflectivity measurements, since the reflectivity is close to unity.

The doping dependence of the b-axis conductivity is summarized in figures 2.5, 2.4. At very low doping, i.e. in the insulating phase, the electronic conductivity is very small and the FIR range is dominated by narrow features corresponding to IR active phonon modes. The electronic conductivity rapidly increases with hole doping. Already for the strongly underdoped samples the above described features become apparent such as the SC-induced dip feature in the a-axis response. Also the broad electronic mode in the b-axis response is very pronounced and located around  $260\text{cm}^{-1}$ . With increasing doping the conductivity increases, and the specific features mentioned above are resolved even in the strongly overdoped samples although they become much weaker and thus hard to detect. For instance, the weak contribution from the  $260\text{cm}^{-1}$  mode is still resolved in the b-axis conductivity of the over-doped sample in Fig. 2.5 e and f.

One of the most important applications of the IR data is the study of the superconductive condensation process. According to BCS theory the spectral weight is transferred from the Drude peak to the delta function at the origin. In classical BCS superconductors the signatures of the superconductive gap are

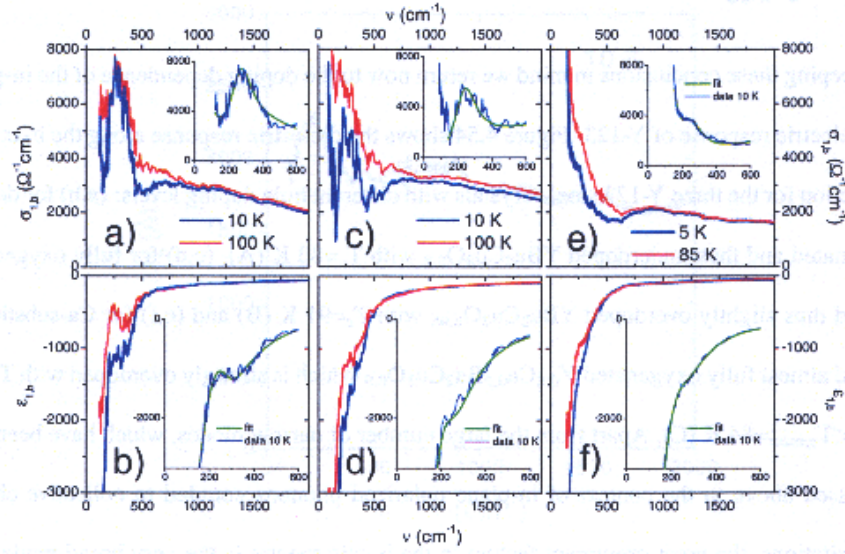


Figure 2.5: Doping dependence of the b axis real part of the conductivity and dielectric function for de-twinned  $YBa_2Cu_3O_{7-\delta}$  crystals as measured by ellipsometry[10]: fig. a, b correspond to  $\delta = 0.2$ ; c,d -  $\delta = 0.05$ ; e,f is strongly over-doped  $Y_{0.8}Ca_{0.2}Ba_2Cu_3O_{6.9}$ . Inset shows the result of a Lorentzian fit (green line) for the 10K spectra (blue line).

clearly resolved in the conductivity spectra. As was mentioned already, in the clean limit the normal state Drude peak is narrower than the superconductive gap, while in the dirty limit it is much wider than the gap (see fig. 2.6). In high

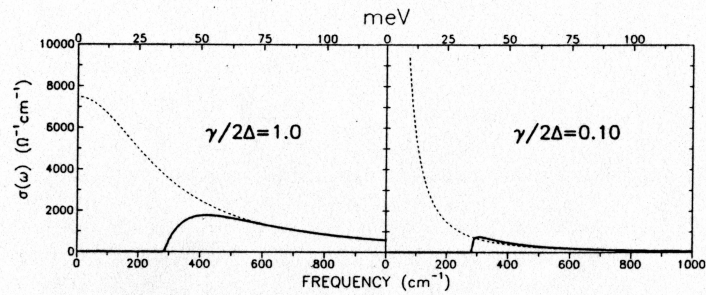


Figure 2.6: Conductivity of a classical BCS superconductor in dirty (a) and clean (b) limits [25].

temperature superconductors it has been concluded that the SC-induced spectral feature can not be directly associated with the superconductive gap. The debate about the correct interpretation is ongoing. Nevertheless, the fact that there is a delta function at zero frequency is established also for the HTSC. Therefore, one can apply similar so-called sum-rule arguments as was successfully done in

the case of the conventional superconductors. The spectral weight (SW) sum rule states that the integrated conductivity remains unaffected by the superconductive transition. This can be expressed as:

$$\int_0^{\infty} (\sigma_{1n}(\omega) - \sigma_{1s}(\omega)) d\omega = 0, \quad (2.1)$$

where  $\sigma_{1n}$  is the normal state conductivity, and  $\sigma_{1s}$  is the conductivity in the superconductive state. If the upper integration limit is set to  $6\Delta$ , formula gives the Ferrel-Glover-Tinkham sum rule, which claims that the normal state spectral weight from the region below  $6\Delta$  goes into delta function in the superconductive state. The delta function can not be measured directly by spectroscopic techniques which are limited to the finite frequency range. Nevertheless, it can be derived from the inductive response which is contained in the real part of the dielectric function. Generally, the complex conductivity due to the superfluid is:

$$\sigma(\omega) = \frac{\omega_p^2}{8}\delta(\omega) + i\frac{\omega_p^2}{4\pi\omega}, \quad (2.2)$$

where  $\omega_p$  is the plasma frequency of the Drude model. This formula was derived from the Drude formalism with the assumption that  $\Gamma \ll \omega \ll \omega_p$ . For conventional superconductors the plasma frequency can be calculated using the relation  $\varepsilon_1(\omega) = 1 - \omega_p^2/\omega^2$ , which follows from 2.2. The experimental data demonstrate that  $\varepsilon_1$  closely follows a  $\omega^{-2}$  dependence. Furthermore, for conventional superconductors the slope of  $\varepsilon_1$  determines the London penetration depth  $\lambda_L$ . The sum rule also provides access to the quasi-particle kinetic energy as was mentioned already in the introduction. However, it is necessary to note that this relation between the spectral weight and the kinetic energy is strictly valid only for model Hamiltonians whose single particle part is of the nearest neighbor tight binding form[34]. The application of this spectral weight formalism to HTSC differs a bit from the case of conventional superconductors. One of the problems is the precise determination of the frequency, which corresponds to the upper integration limit in 2.3. Ellipsometry provides direct information about  $\varepsilon_1$ , and thus the plasma frequency can be determined more accurately than from reflectivity data, where it is calculated indirectly using model assumptions. In ellipsometry the plasma frequency is a function of both real and imaginary parts of dielectric function, and it is frequency dependent because there is no assumption of  $\omega^{-2}$  dependence

2.2:

$$\omega_p(\omega) = \omega \sqrt{\frac{\varepsilon_2(\omega) + (\varepsilon_\infty - \varepsilon_1(\omega))^2}{\varepsilon_\infty - \varepsilon_1(\omega)}} \quad (2.3)$$

In the latest investigation made by our group[30], it is found that the SC-induced spectral changes extend to a very high energy scale of the order of 2 eV. Therefore, it is incorrect to say that all spectral weight from the Drude peak goes into the delta function like it is for the case of conventional superconductors. Already in the normal state there is a characteristic redistribution of the spectral weight from very high to low-energy which is well accounted for by a so-called extended Drude-like model that includes inelastic scattering of the charge carriers. The observed SW redistribution thus corresponds to a decrease in the inelastic scattering rate that is further enhanced in the SC state. A detailed analysis of the related SC-induced changes in the free carrier kinetic energy are not in contradiction with the predictions of the BCS model and thus give no direct evidence that an unconventional pairing mechanism is at work in the cuprate HTSC. [10].

## 2.4 C-axis infrared properties

The c axis response of the HTSC exhibits a very strong and characteristic variation as a function of carrier doping. Once more, the phase diagram falls into three regions corresponding to the underdoped, optimally doped and the overdoped regimes. A representative example for the c-axis response of an underdoped Y123 crystal is shown in fig. 2.7 The spectrum consists of a very broad electronic background on which seven phonon modes at 155, 190, 285, 320, 570, 620, 630  $cm^{-1}$ , plus a broad peak below  $T_c$  around  $500cm^{-1}$  are superimposed. In the context of this thesis we are mainly concerned with the electronic background which is shown in Fig. 2.7 after subtraction of the phonons. The electronic background can be seen to undergo characteristic changes as the temperature is successively lowered starting from room temperature. Most importantly, the signatures of a gap-like suppression of the low frequency electronic conductivity with an onset around  $750cm^{-1}$  occurs already well within the normal state, i.e. around  $T^* = 150 \gg T_c = 80K$ . It is this partial normal state gap like feature in the c-axis conductivity spectra that has previously been associated with the pseudo-gap phenomenon which is also seen by a number of other spectroscopic techniques such as tunnelling, ARPES, and Raman.

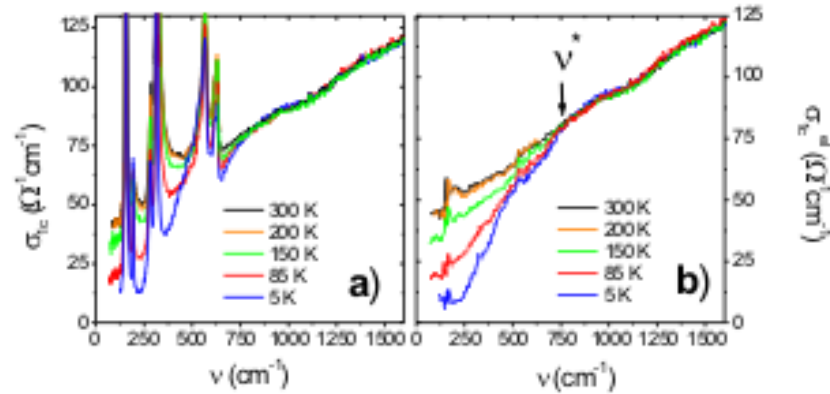


Figure 2.7: C axis conductivity of under-doped  $YBa_2Cu_3O_{6.8}$  crystal with  $T_c = 80K$  (a); the conductivity after subtraction of the phonon contributions and the Josephson plasmon mode (b) [10].

We start the discussion by first considering the assignment of the phonon modes. Group theory predicts 7 IR-active  $c$ -axis phonon modes (see fig. 2.8). The mode at  $570cm^{-1}$  is associated with the vibration of the apical oxygens against the copper in the filled Cu-O chains. In oxygen deficient samples there are two additional modes at 620 and 530  $cm^{-1}$  that arise from apical oxygens adjacent to half empty chain fragments. The weight ratio of the higher to the lower apical modes in return can be used to obtain an estimate of the oxygen content of the CuO chains in these 123 compounds. The next lowest mode is the so-called bond-bending mode at  $320cm^{-1}$  which involves the in-phase vibrations of the in-plane O against the Y ions. The mode at  $285cm^{-1}$  corresponds to the vibrations of Cu ions against oxygen in the chains, and thus is often called the chain mode. The mode at  $190cm^{-1}$  corresponds to vibration of the Y ions against Cu in the chains. At last the  $150cm^{-1}$  mode involves vibrations of the heavy Ba ions against Cu in the chains.

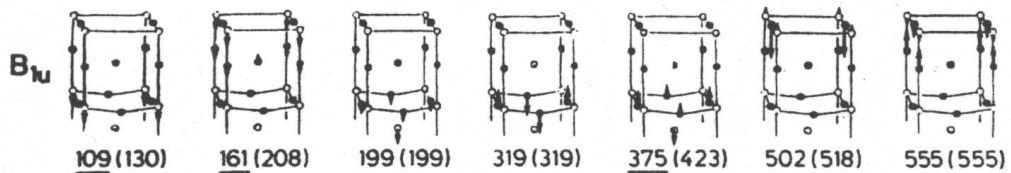


Figure 2.8: Eigenvectors of  $c$ -axis phonons of Y123. Filled circles-O; open circles-Cu; hatched circles-Ba; dotted circles-Y.

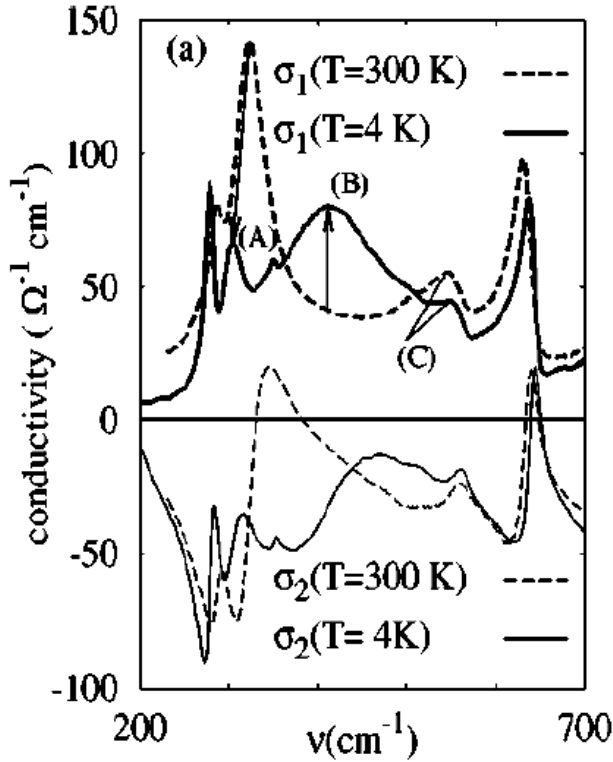


Figure 2.9: Spectra of  $c$ -axis conductivity of underdoped Y123 with  $T_c = 53K$ . The symbols (A) (B) (C) indicate most pronounced anomalies. It is modified figure from [31].

Some of the phonon modes exhibit a very anomalous  $T$ -dependence in the vicinity of the SC transition that is their frequencies increase with increasing temperature. It contradicts the simple theory that with increasing temperature the phonon modes become softer since the average distances between ions in the lattice increases. The most pronounced anomalies involve the bond bending mode at  $320\text{cm}^{-1}$ . In some underdoped Y123 crystals (with  $T_c$  around 50 to 60 K), this bond-bending mode loses most of its spectral weight and its center frequency is red-shifted by about  $20\text{cm}^{-1}$  below  $T_c$ . The spectral weight of the  $570\text{cm}^{-1}$  mode also decreases below  $T_c$ . At the same time, the additional broad electronic peak appears below  $T_c$ .

This additional mode has been associated with a so-called transverse Josephson plasma mode. This model was first introduced by van der Marel and Tsvetkov[32]. It approximates the 123 structure in terms of a stack of two kinds of Josephson-junctions, the so-called intra-bilayer one involving tunnelling currents across the Y-layer, and the inter-bilayer one due to the blocking layer consisting of BaO and CuO chain layers. These two kinds of Josephson-junctions exhibits rather different Josephson-plasma frequencies. The broad mode forming below  $T_c$  arises here from the out-of-phase oscillation of the Josephson-currents in the two kinds of junctions in response to an electric field whose frequency is in between the eigenfrequencies of the respective Josephson junctions. These two kinds of Josephson junctions have their own plasma frequencies  $\omega_{pbl}$  and  $\omega_{pint}$  assigned to them. After that, from the boundary conditions of the Maxwell's equations one can obtain

the dielectric function  $\varepsilon(\omega)$ :

$$\varepsilon(\omega) = \frac{(d_{bl} + d_{int}) \varepsilon_{bl}(\omega) \varepsilon_{int}(\omega)}{d_{bl} \varepsilon_{int}(\omega) + d_{int} \varepsilon_{bl}(\omega)} \quad (2.4)$$

which has a pole at  $\omega_{jp}$  corresponding the Josephson plasmon in IR spectrum:

$$\omega_{jp}^2 = \frac{d_{bl} \omega_{pint}^2 + d_{int} \omega_{pbl}^2}{(d_{bl} + d_{int}) \varepsilon_{\infty}}, \quad (2.5)$$

where  $d_{bl}$  is the distance between  $CuO_2$  planes in a bilayer,  $d_{int}$  is the distance between bilayers,  $\varepsilon_{bl} = \varepsilon_{\infty} - \omega_{pbl}^2/\omega^2$ ,  $\varepsilon_{int} = \varepsilon_{\infty} - \omega_{pint}^2/\omega^2$ . This theoretically calculated plasma frequency coincides pretty well with the measured one in the IR spectra (see fig. 2.11). For the results of the calculations as plotted in fig. 2.11 the following parameters have been assumed:  $2d_{bl} = d_{int} = 10\text{\AA}$ ,  $\varepsilon_{\infty} = 5$ . The plasma frequencies  $\omega_{pbl}, \omega_{pint}$  are apparent in the figure as the zero crossing points.

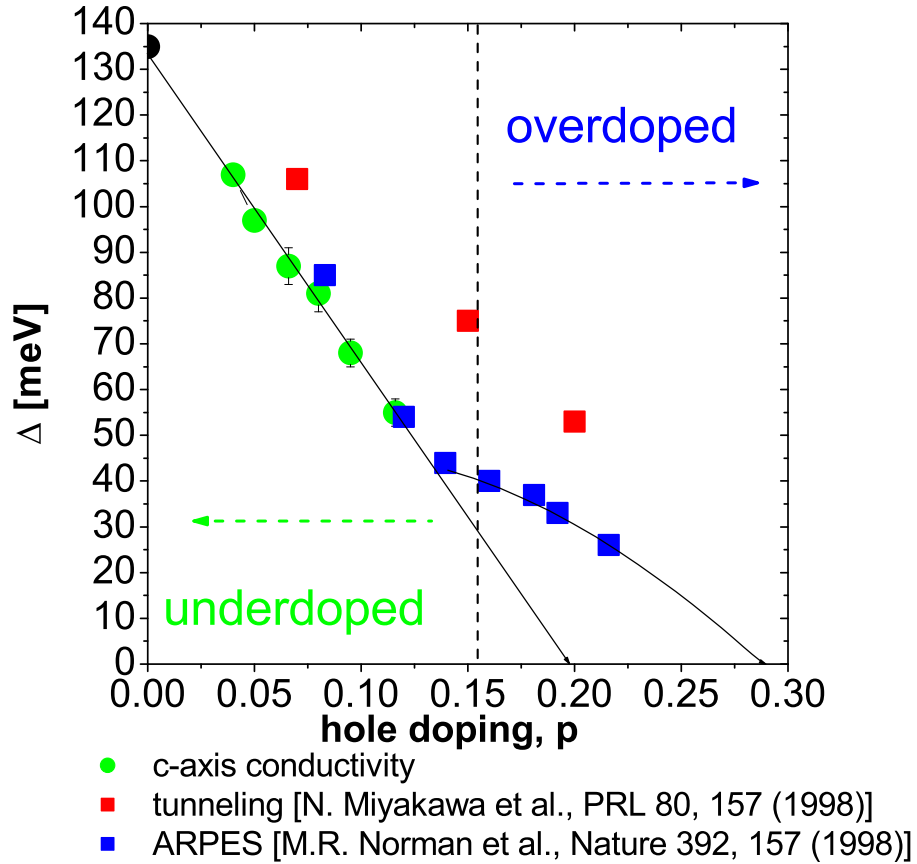


Figure 2.10: Doping dependence of pseudogap [10].



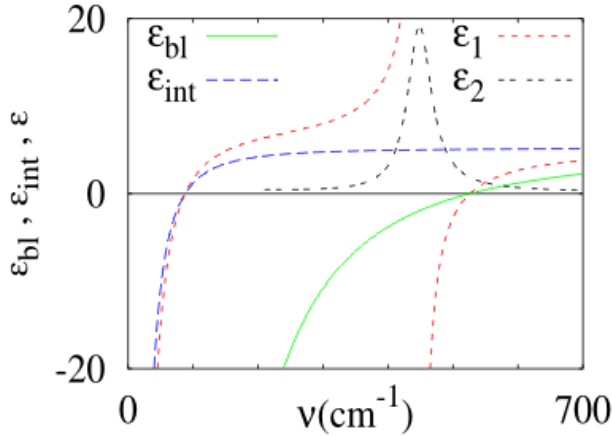


Figure 2.11: Dielectric function in the Josephson super-lattice model [33].

field is largely affected by the Josephson currents which lead to an inequivalent charging of the  $CuO_2$  planes. Particularly, the spectral weight loss of the bond bending mode in Y123 can be related to the fact that with decreasing temperature the local field acting on the in-plane oxygens decreases. As discussed in detail in the next paragraph, the phonon anomalies of Bi2223 trilayer compound can be explained in a similar manner. Meanwhile, all these explanations of the phonon anomalies still remain on a phenomenological level.

Another important issue for the analysis of the c-axis spectra is the calculation of the spectral weight and the corresponding implications of the spectral weight sum rule. One very important question is where the missing spectral weight due to the pseudo-gap formation in the FIR range region is transferred to. Detailed ellipsometric studies were performed in our group [36] in order to address this question. It was found that there is a redistribution of the spectral weight between the pseudo-gap, phonons, Josephson plasmon, broad MIR peak, the origin of which is not established yet, and the peaks in the visible frequency range connected with inter-band transitions. In the superconductive state some spectral weight also goes to the delta function at zero frequency.

Now we turn to the doping dependence of the c-axis conductivity spectrum. With increasing doping the pseudo-gap becomes less pronounced and disappears right at optimum doping. The Josephson plasmon and phonon anomalies are also less pronounced in the optimally doped and overdoped samples than in the underdoped ones. Spectra of slightly under-doped and optimally doped samples

D. Munzar has extended this Josephson plasmon model to explain the phonon anomalies and the transverse plasmon in trilayer compounds[35]. He has shown that the phonon anomalies can indeed be related to the change of the local electrical field inside the bilayer or trilayer regions. The local field is a sum of the external field (due to the IR radiation) and the internal field from charges on the  $CuO_2$  plane. This internal

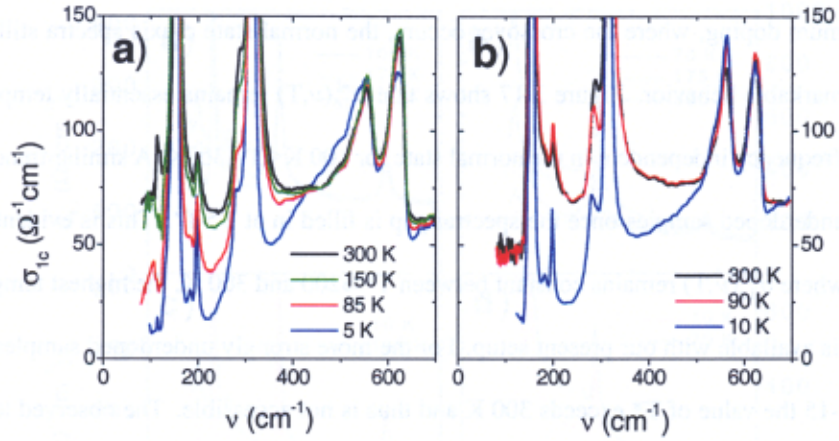


Figure 2.12: Spectrum of c-axis conductivity of slightly under-doped  $Y_{0.86}Ca_{0.14}Ba_2Cu_3O_{6.6}$  crystal (a), and optimally doped  $Y_{0.86}Ca_{0.14}Ba_2Cu_3O_{6.7}$  (b). [10].

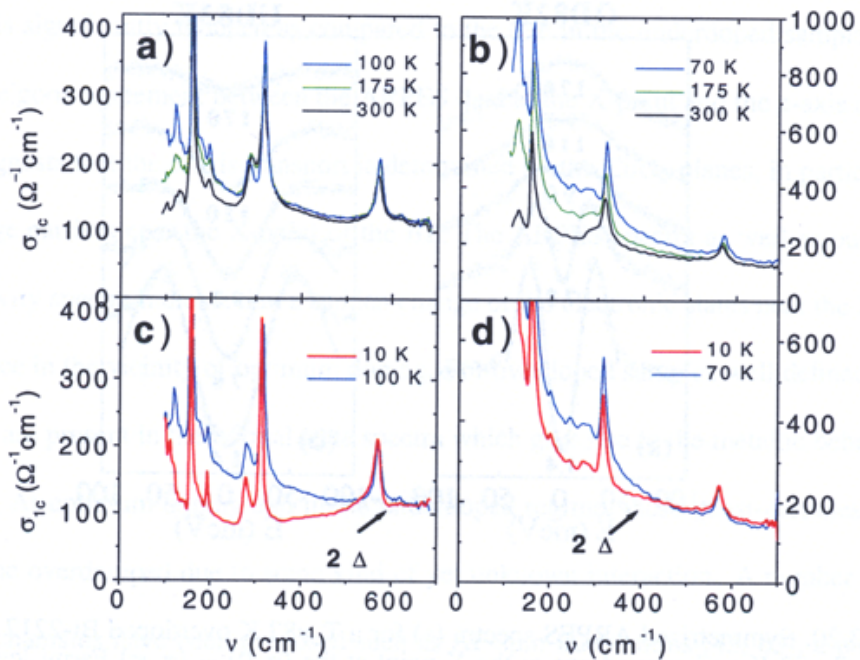


Figure 2.13: C axis conductivity of over-doped  $YBa_2Cu_3O_7$  (a,c) and strongly over-doped  $Y_{0.86}Ca_{0.14}Ba_2Cu_3O_{6.95}$  (b,d) [10].

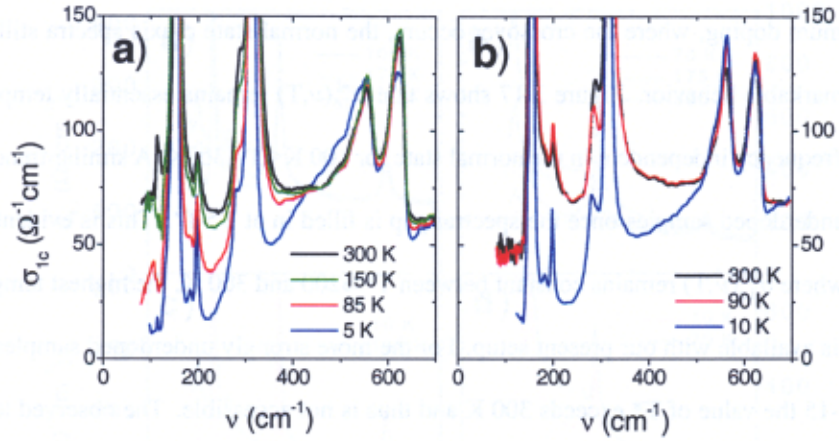


Figure 2.14: Spectrum of the c-axis conductivity of a slightly under-doped  $Y_{0.86}Ca_{0.14}Ba_2Cu_3O_{6.6}$  crystal (a), and optimally doped  $Y_{0.86}Ca_{0.14}Ba_2Cu_3O_{6.7}$  (b). [10].

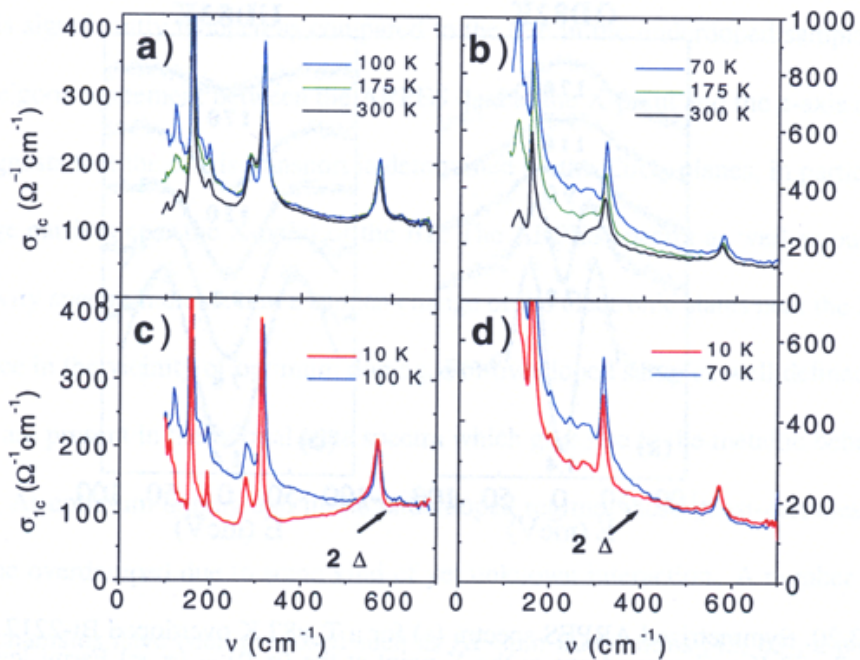


Figure 2.15: C axis conductivity of over-doped  $YBa_2Cu_3O_7$  (a,c) and strongly over-doped  $Y_{0.86}Ca_{0.14}Ba_2Cu_3O_{6.95}$  (b,d) [10].

are plotted in fig. 2.14. Near optimal doping the conductivity remains almost temperature independent in the normal state for the interval from 100 to 300K. The pseudo-gap phenomenon thus is entirely absent in optimally doped and over-doped samples (see fig. 2.10). The spectra of over-doped crystals are shown in fig. 2.15. It can be seen that in the overdoped region the c-axis normal state conductivity finally begins to exhibit the signatures of a Fermi liquid like behavior in a sense that the conductivity increases with decreasing temperature and frequency. The spectra of the optimally and over-doped samples also contain clear signatures of a gap formation. However, in contrast to the underdoped samples, the spectral gap begins to develop now right below the SC transition, i.e. only for  $T < T_c$ . Once more we note that the magnitude of the spectral gap and its doping dependence agree rather well with the values that have been deduced from angle resolved photoemission spectroscopy[37], fig. 2.10.

## 2.5 Josephson resonance and phonon anomalies in $Bi_2Sr_2Ca_2Cu_3O_{10}$

### 2.5.1 Introduction

In this section, we focus on the ellipsometry data on the trilayer Bi2223 compound. In particular, the c-axis Josephson plasmon, the phonon anomalies, and the spectral weight transfer will be discussed. All these results were published in [102]. Related issues for the case of the Y123 compound were discussed in section 2.4.

### 2.5.2 C-axis spectra of Bi2223

A Bi2223 crystal of high quality and size of approx.  $6x4x0.5mm^3$ , was grown by the floating zone technique. Crystal growth method and annealing procedure are described in [108]. The obtained c-axis spectra of this crystal for three different doping levels are shown in fig. 2.16. These spectra were obtained with the technique of ellipsometry using the synchrotron source at ANKA at FZ Karlsruhe. The spectra contain a sizeable number of narrow phonon modes and in addition a broader absorption peak around  $500cm^{-1}$  that appears only in the superconductive state. As was discussed in the previous chapter, this peak corresponds to the

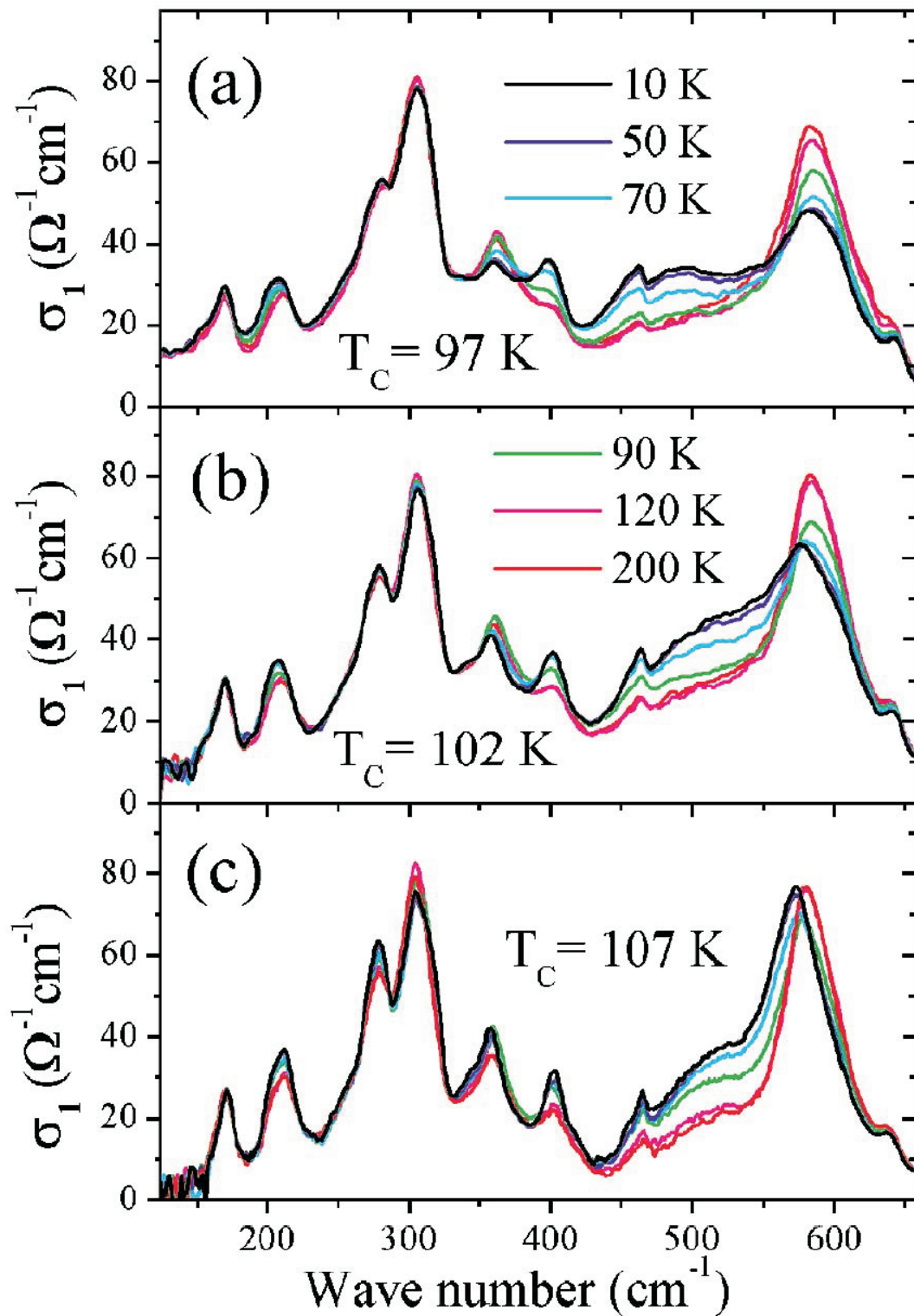


Figure 2.16: Optical conductivity of three Bi2223 crystals with different doping levels ranging from underdoped to nearly optimally doped

so-called transverse Josephson plasmon mode as originally proposed by van der Marel and Tsvetkov [32]. Meanwhile, there have been proposals for an alternative interpretation in terms of spin-fluctuation mediated c-axis hopping conductivity by Timusk and Homes [103]. However, the proposed scenario is rather vague and lacks a detailed microscopic justification. The subject of the present chapter is the explanation of this absorption peak in framework of the model by Marel and Tsvetkov, which was extended by Munzar et al to include the local electric field effect on the phonon modes.

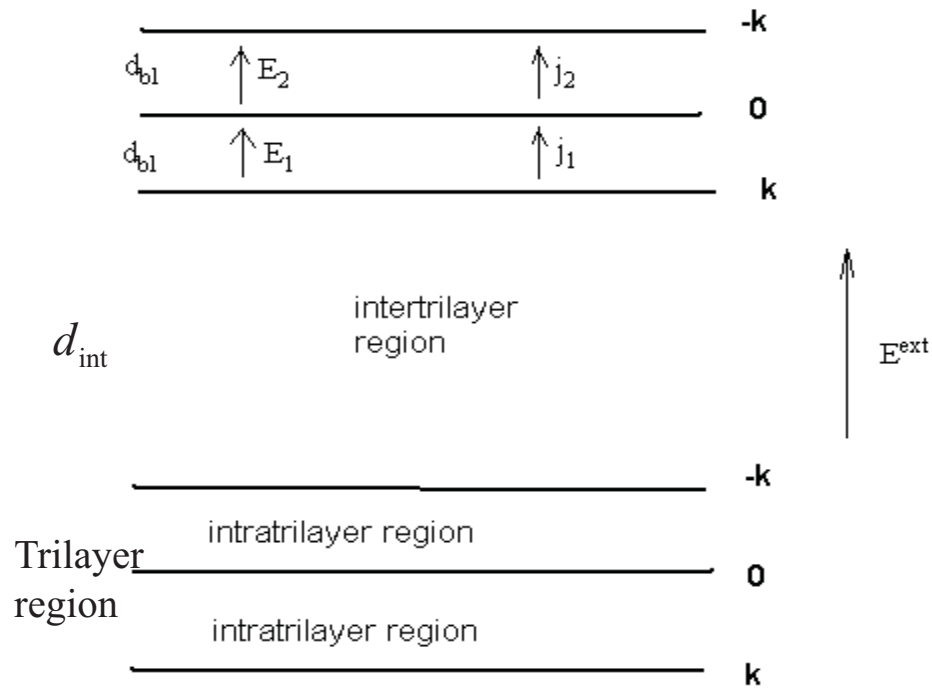


Figure 2.17: Model of trilayer Bi2223: the Josephson currents in intratrilayer regions produce a plasmon feature in the infrared spectrum around  $500 \text{ cm}^{-1}$

The phonon modes are centered at 97, 128, 170, 211, 305, 360, 400, and  $582 \text{ cm}^{-1}$ . There are also two additional rather weak phonon modes at 276, and  $471 \text{ cm}^{-1}$  that are most likely caused by the incommensurate modulation of the BiO and SrO layers [104]. As compared to Bi2212 the present c-axis spectra for Bi2223 contain two additional phonon modes at 128 and  $400 \text{ cm}^{-1}$ . The frequencies of all the other phonon modes are rather similar to the ones in Bi2212. A complete assignment of the phonon modes in the case of Bi2212 can be found in [105]. We have also performed our own shell model calculations for the case of Bi2223. We find that the modes at 97, 128, 170,  $211 \text{ cm}^{-1}$  correspond to the vibrations of

heavy Bi and Sr ions. The  $305\text{cm}^{-1}$  mode involves the vibrations of Bi plane oxygen against Ca. The main subject of the present study is the explanation of the anomalous behavior of the modes at  $360$ ,  $400$ , and  $582\text{cm}^{-1}$  in the SC state. Their assignment will be discussed in more detail in the following paragraph.

The third issue is the spectral weight redistribution in the superconductive state. We find that for the Bi2223 compound one can not apply the Ferrel-Glover-Tinkham (FGT) sum rule in the same way as for conventional superconductors [106]. This sum rule states that the spectral weight of the delta function in the superconductive state is accumulated from a limited frequency range of  $\omega < 6\Delta$ . As we will show, in the c-axis response of Bi2223 the energy scale of the spectral weight transfer is significantly wider.

### 2.5.3 Josephson superlattice model and transverse plasmon

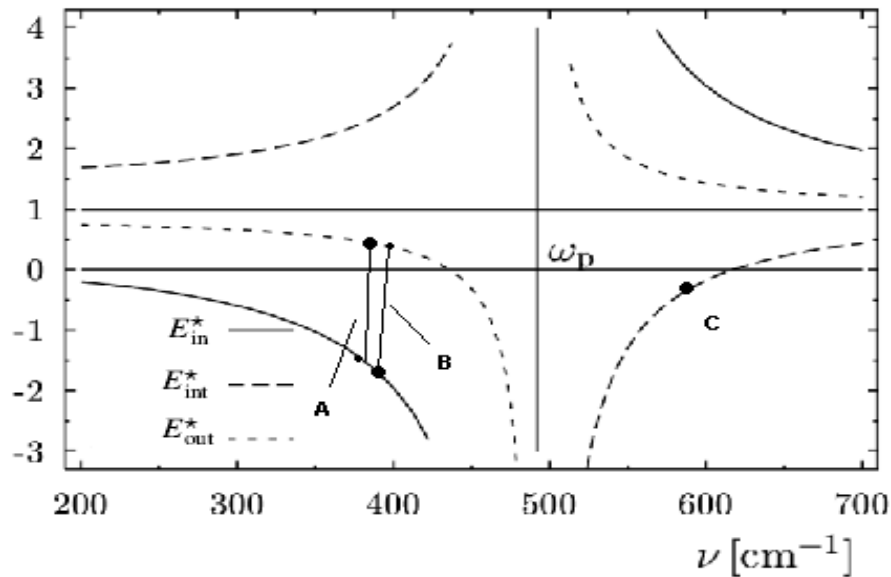


Figure 2.18: Frequency dependent variation of the local field due to Josephson currents.  $E_{int}^*$  is local field between trilayers,  $E_{in}^*$  is local field at inner layer of a trilayer,  $E_{out}^*$  is local field at outer layer of a trilayer. Local field at the sites of particular ions related to  $360$ ,  $400$ , and  $582\text{cm}^{-1}$  phonons are denoted by A, B, C correspondingly. Point A corresponds to  $360\text{cm}^{-1}$ .

The Bi2223 compound contains three closely placed CuO layers, the so-called trilayer. The distances between the layers are about  $d_{bl} = 3.4\text{\AA}$ . The space

between these trilayers is called the intertrilayer region. The width of this region is about  $d_{int} = 12\text{\AA}$ . The structure of the Bi2223 compound is displayed in fig. 2.17.

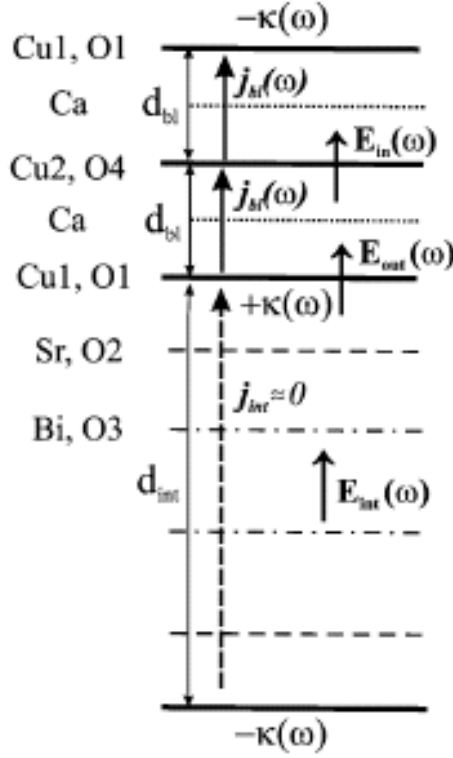


Figure 2.19: Local fields in the Josephson superlattice model

In the case of the Bi2223 compound with its extremely wide and thus very poorly conducting intertrilayer junction the contribution of the intertrilayer current can be safely ignored, i.e.  $j_{int} = 0$ . Each  $CuO_2$  plane has its own local charge density, and if these planes are close enough to each other, Josephson current can appear. In the Josephson superlattice model (JSM) for trilayer compounds, the outer planes of a trilayer have opposite charge densities  $k, -k$ . The inner plane does not become charged (the charge density is zero). The Cooper pairs can hop from the outer plane to the inner plane first, producing the current  $j_1$ . Then they hop from the inner plane to second outer plane producing the current  $j_2$ .

Since the inner plane is not charged, we can apply the JSM for bilayer compounds substituting  $d_{bl}$  in formulae 2.5 with  $d_{tr} = 6.8\text{\AA}$ . Finally, we obtain the following formulae for the plasma frequency in the case of a trilayer compound:

$$\omega_{jp}^2 = \frac{d_{int}\omega_{pbl}^2}{(d_{tl} + d_{int})\varepsilon_\infty}, \quad (2.6)$$

where  $\varepsilon_\infty = 4$  is local dielectric constant unaffected by Josephson current.  $\omega_{pbl} = 1250\text{cm}^{-1}$  is the plasma frequency in intralayer region (see fig. 2.11). For the given values of the parameters the plasma frequency is about  $500\text{cm}^{-1}$ .

Based on the JSM we can now determine the local internal field inside the material [107]. Let  $E_{out}$  be the local field inside an outer CuO layer (in trilayer),  $E_{in}$  is the local field inside an inner CuO layer, and  $E_{int}$  is local field in intertrilayer regions. This notation is illustrated in fig. 2.19. Then according to the Munzar



model, these fields can be expressed with the following formula

$$E_{int}^* = \frac{E_{int}}{\langle E \rangle} = \frac{(d_{tl} + d_{int}) \varepsilon_{tl}}{(d_{tl} \varepsilon_{int} + d_{int} \varepsilon_{tl})} \quad (2.7)$$

$$E_{in}^* = \frac{E_{in}}{\langle E \rangle} = \frac{(d_{tl} + d_{int}) \varepsilon_{int}}{(d_{tl} \varepsilon_{int} + d_{int} \varepsilon_{tl})} \quad (2.8)$$

$$E_{out}^* = \frac{(E_{int}^* + E_{in}^*)}{2} \quad (2.9)$$

here  $\langle E \rangle$  denotes the average field. It is these local fields that are acting on the ions that participate in lattice vibrations (phonons). Accordingly, we can account for the anomalous SC-induced changes of the phonon modes in terms of the changes of the local field caused by the Josephson currents. The frequency dependencies of the local fields are shown in fig. 2.18. Points A, B, C denote the frequencies of the phonons at  $360$ ,  $400$ , and  $582\text{cm}^{-1}$ .

## 2.5.4 Phonon anomalies

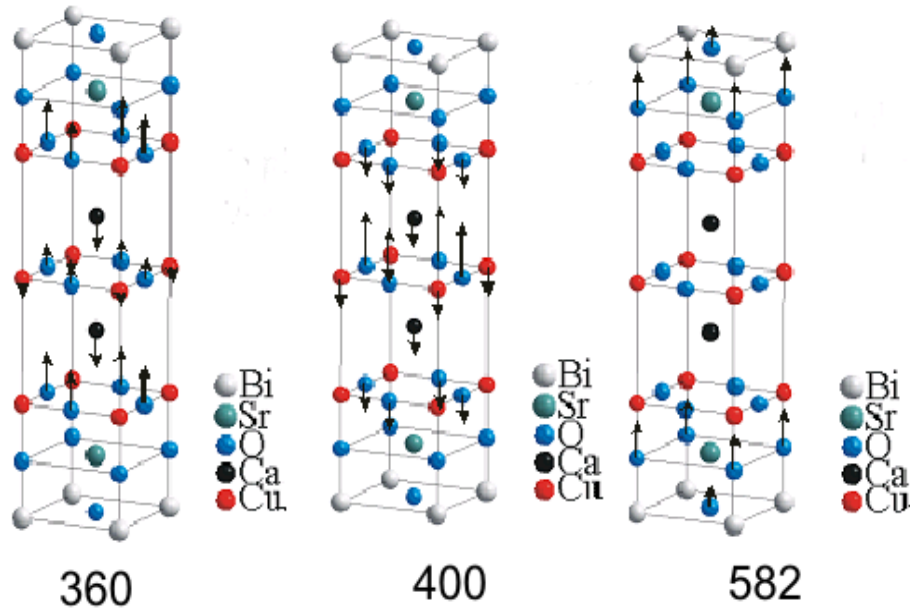


Figure 2.20: Vibrations of ions involved in  $360$ ,  $400$ ,  $582\text{cm}^{-1}$  modes.

**$360\text{cm}^{-1}$  in phase mode of planar oxygens**

This phonon corresponds to point A in fig. 2.18. The important quantities are the the local field  $E_{in}^*$  and  $E_{out}^*$ . Below  $T_c$  the value of  $E_{out}^*$  decreases due to the Josephson current. But it remains positive.  $E_{in}$  acquires a larger negative value. Directions of the local fields are not in agreement with the phonon eigenvector. Therefore, the strength of this mode decreases below  $T_c$ .

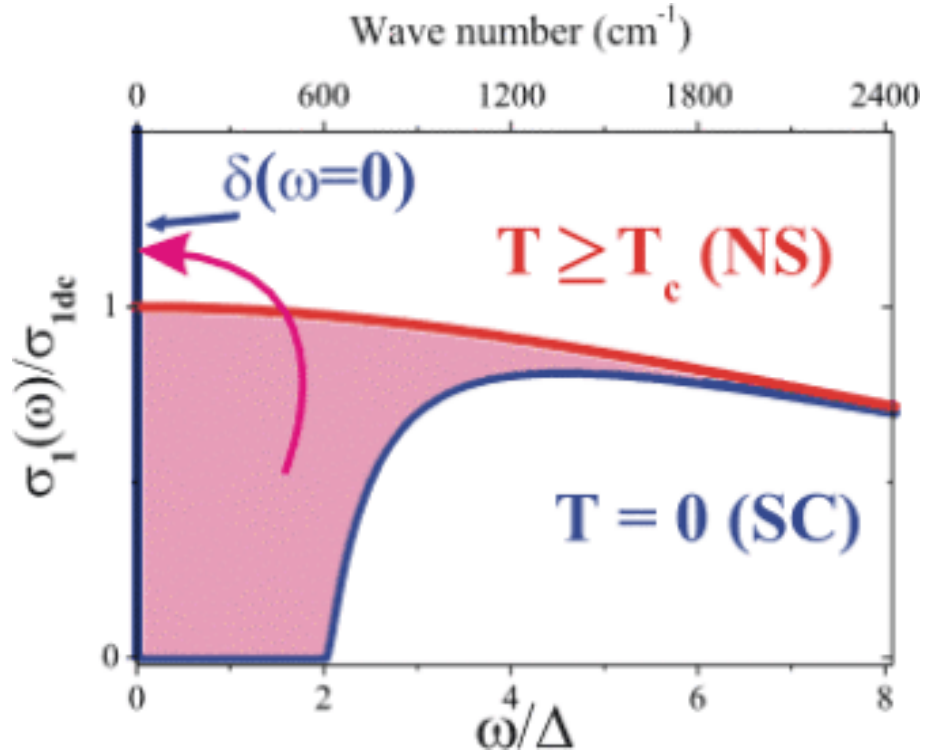


Figure 2.21: Spectral weight transfer in ordinary superconductors

 **$400\text{cm}^{-1}$  out of phase mode of planar oxygens**

In this case, the same local fields,  $E_{in}^*$  and  $E_{out}^*$  act on the ions connecting with the phonon mode. However, the eigenvector pattern is in coincidence with directions of local fields below  $T_c$ . Therefore, this mode becomes stronger below  $T_c$ .

 **$582\text{cm}^{-1}$  Apical oxygens and oxygen in Bi plane**

For this mode, the value of  $E_{int}^*$  is important. It corresponds to point C in fig. 2.18. It is the local field between trilayers. Below  $T_c$ , the value of local field

decreases with respect to normal state. Therefore, the strength of this mode decreases.

### 2.5.5 Spectral weight transfer and sum rule

For the case of conventional superconductors the Ferrell Glover Tinkham sum rule states that:

$$\Delta S = \int_0^{6\Delta} [\sigma_1^N(\omega, T = T_c) - \sigma_1^{SC}(\omega, T \ll T_c)] = \frac{c^2}{8\lambda_L^2} \quad (2.10)$$

here,  $\Delta$  is the frequency of the superconductive gap,  $\lambda_L$  is the penetration depth,  $\sigma_1^N$ ,  $\sigma_1^{SC}$  are conductivities in normal and superconductive state correspondingly. In other words, the FGT sum rule means that all spectral weight from the region  $\omega < 6\Delta$  goes to the delta function at zero frequency. The conductivity in the range  $\omega > 6\Delta$  is almost the same for the normal and superconductive states (see fig. 2.21), and it can be expressed by the formula ( $\alpha$  is a small parameter):

$$\sigma_1^{SC} = \sigma_1^N \left( 1 - \alpha \frac{\Delta^2}{\omega^2} \right) \quad (2.11)$$

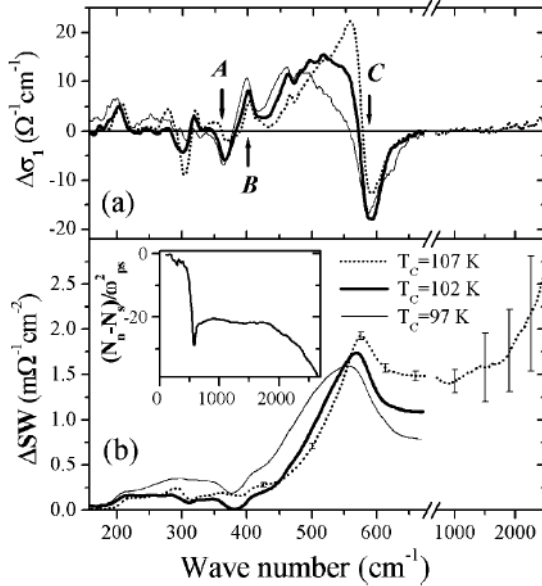


Figure 2.22: Spectral weight transfer in Bi2223. Phonon anomalies denoted by A, B, C.

the changes of the optical conductivity between the superconductive and the normal states,  $\Delta\sigma_1 = \sigma_1(10K) - \sigma_1(100K)$ .  $\Delta SW(\omega)$  is the integral in 2.10

In the Bi2223 compound the absorption peak at  $500\text{cm}^{-1}$  appears only below  $T_c$ . In the context of the JSM model, the spectral weight of this peak is in fact part of the superconductive condensate.

It is the presence of this additional spectral weight due to the transverse Josephson-plasma mode which leads to the apparent failure of the FGT sum rule for the case of Bi2223. Fig. 2.22 displays

taken from 0 to  $\omega$ . The inset of fig. 2.22 shows the frequency dependence of  $(N_n - N_s)/\omega_{ps}^2$ , which is proportional to the ratio of the left and right parts of equation 2.21. Namely, the ratio is  $8\Delta SW(\omega)\lambda_L^2/c^2$ . Physically, it is the ratio of spectral weight changes between normal and superconductive state to spectral weight of delta function. The spectral weight of the delta function was estimated from the imaginary part of the conductivity. According to the FGT sum rule this ratio should approach the value of 1 for  $\omega \ll \Delta$ . In clear contradiction, the inset of fig. 2.22 shows that this ratio acquires a large negative value of about -30 thus testifying for a striking violation of the FGT sum rule.

### 2.5.6 Summary

In the summary, we have found firstly that the JSM interprets the c-axis infrared response of HTSC rather good. However, the model is still on the phenomenological level. Secondly, the spectral weight transfer in Bi2223 compound does not obey the FGT sum rule which is valid for the case of ordinary superconductors.

# Chapter 3

## Pseudogap

### 3.1 Introduction

The superconductive energy gap is one of the most important properties of conventional superconductors. In the infrared range it manifests itself as a suppression of the conductivity below a certain frequency. From the experimental data one can thus determine the magnitude of energy gap. In the  $c$  axis spectra of the high temperature superconductors only a gradual and partial suppression of the conductivity is observed, which furthermore sets already in the normal state at temperatures well above  $T_c$ . This partial suppression of the  $c$ -axis conductivity is interpreted in terms of the so-called pseudo-gap (PG) phenomenon which has been observed by a number of other spectroscopic techniques and thus seems to be a generic feature of the charge dynamics of underdoped HTSC. From transport theory it is known that the  $c$ -axis conductivity is related to the density of excitations (in the incoherent limit). This allows to define the PG as the incomplete depression of the excitations below the energy  $2\Delta$  corresponding to the frequency below which the conductivity is partially suppressed. The pseudo-gap can be measured by different techniques from which one can deduce the density of excitation states. So, the PG has been also observed by specific heat [38, 39], angle resolved photoemission[37], and tunnelling spectroscopy[40]. All these different techniques yield a similar energy scale of the gap  $2\Delta$ . Therefore, one can conclude that the same PG phenomenon is probed by these different techniques. However, one should also mention that in some theoretical papers the authors adopted the point of view that the PG measured by other techniques is different from the  $c$ -axis PG in conductivity[41].

The origin of the PG is not established yet. Several controversial models have been proposed. One group of models assumes the existence of preformed Cooper pairs in the normal state, and explains the PG in terms of a precursor superconductive state that is lacking macroscopic phase coherence. A second class of models assumes that the PG is unrelated to superconductivity. For example, the idea of spin-charge separation (which was proved only for 1D systems) speculatively extends to quasi-2D systems. In this case, there are two kinds of quasi-particles: charged holons with zero spin and spinons which have zero charge and spin  $1/2$ . Spinons pair to form a gap which is called spin gap or PG. The other proposals suggest metallic stripes as a quasi 1D system approximately described by a 1D electron gas model with spin charge separation. These stripes presumably can exist above  $T_c$ , and this is the reason of the PG. An extension of this model suggests that the PG results from the anti-ferromagnetic correlations in the stripes. These AF correlations appear only below the PG temperature  $T^*$  while the charge stripes appear at higher temperature. The argument against this model is that the stripes are not pure 1D system since the interactions between the charges in different stripes plays some role. This makes a model based on independent 1D stripes rather unrealistic. Concerning the preformed pair model, the most significant counter argument is related to the very high values of the PG temperature  $T^*$  which for strongly under-doped Y123 even exceeds room temperature. It is difficult to believe that Cooper pairs exist at such high temperature. The second argument, which will be considered in this thesis is related to the effect of magnetic impurities like Ni on the PG. Below, it is shown that by introducing Ni impurities the superconductivity can be completely suppressed, and, at the same time, the PG energy scale becomes strongly enhanced.

In the following chapter, a number of spectroscopic techniques (other than IR spectroscopy) are introduced, and it is discussed what information they provide about the normal state pseudogap.

## 3.2 Angle resolved photoemission

Angle resolved photoemission (ARPES) is a powerful technique to probe the superconductive gap. This technique is based on the photoelectric effect. High energy photons with an energy of about 20eV are selected by a monochromator and illuminate the surface of a HTSC crystal in high vacuum. Behind the sample

a photoelectron detector is placed that can be set to different angles relative to the crystallographic axes of the crystal. Eventually, one measures the dependence of the intensity on the energy of incident photons and the angle. For materials with a 2D electronic structure, the angular dependence can be converted to the dependence on an electron momentum  $\vec{k}$  parallel to the surface.

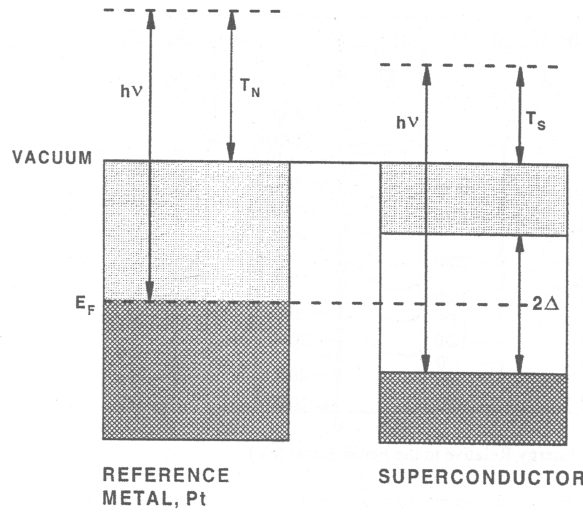


Figure 3.1: Idea of the ARPES measurement of the superconductive gap.[42].

To measure the superconductive gap by ARPES one uses a reference metal, which has electric contact with the superconductive crystal (see fig. 3.1). The reference metal and the superconductor thus have the same Fermi level, and the difference in photoelectron energies of two electrons emitted from the superconductor and the metal is equal to  $\Delta$  characterizing the superconductive gap. Therefore, the ARPES can probe the energy and momentum of the electrons in filled states below the Fermi level. The complete theory is given in [43]. The intensity on the detector depends on the electron energy  $e_k$  measured from Fermi level, and the momentum component parallel to the surface  $k$ :

$$I(\vec{k}, \omega) = I_0(\vec{k})f(\omega)A(\vec{k}, \omega), \quad (3.1)$$

where  $A(\vec{k}, \omega)$  is the spectral function,  $\omega$  characterizes the photoelectron energy relative to the Fermi level. In the rough approach of non-interacting fermi-liquid the line width is neglected  $A(\vec{k}, \omega) = \delta(\omega - e_k)$ . For real materials, more elaborate

models have to be applied to calculate  $A(\vec{k}, \omega)$  [43] and the line has a certain width.

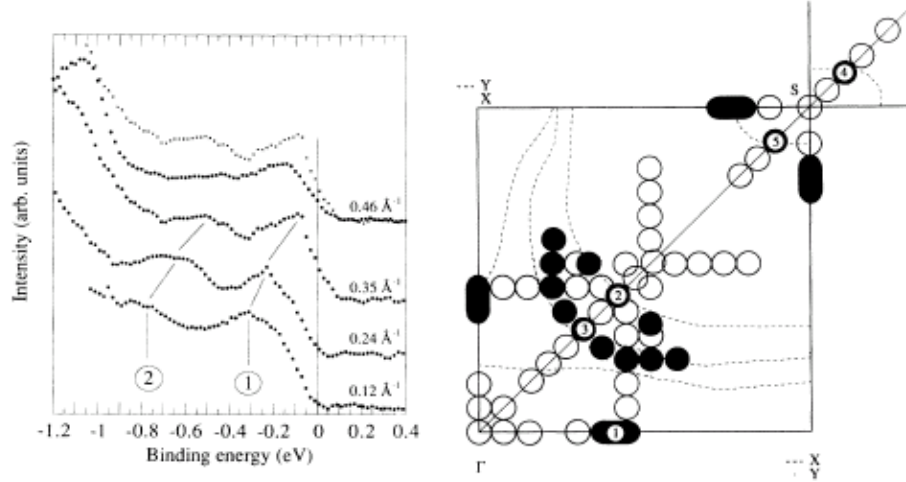


Figure 3.2: Fermi surface of  $YBa_2Cu_3O_{6.9}$  mapped by ARPES[44]. On the left side the intensity corresponding to point (1) is plotted. On the right plot, filled circles indicates points which band crosses Fermi level; open circles are the points where Fermi level crossing is not detected. The dashed lines indicate theoretical prediction of Fermi surface[45].

Since HTSC are quasi 2D materials, they are ideal for ARPES investigations. The whole Fermi surface can be mapped using ARPES. Fermi surface of  $YBa_2Cu_3O_{6.9}$  crystal[44] is plotted in fig 3.2. The Fermi surface corresponds to the transverse momentum where quasi-particle peak disappears as it moves to zero frequency. The pseudo-gap and the superconductive gap can be determined by monitoring the evolution of intensity peak at the  $(\pi, 0)$  point. The study of the PG are mostly done on the Bi2212 compound, which has two Cu-O layers as Y123, but does not contain the chains. The PG manifests itself as a quasi-particle (QP) peak at the k vector  $(\pi, 0)$  or  $(0, \pi)$  (see fig. 3.3. The peak position and the peak leading edge does not change in the temperature range below  $T^*$  which corresponds to the PG temperature. Below  $T_c$  the sharp peak starts to develop and its position does not change as well. The sharp peak is associated with the superconductive gap. Meanwhile, the SC gap and the PG can not be distinguished from each other. Generally, there are two possibilities to identify the gap: using the peak position, and using the leading edge. Therefore, one can define a low energy PG (leading edge) and a high energy PG (peak position). The PG has d-wave k-dependence plotted in fig. 3.3(b). Interesting, that the peak



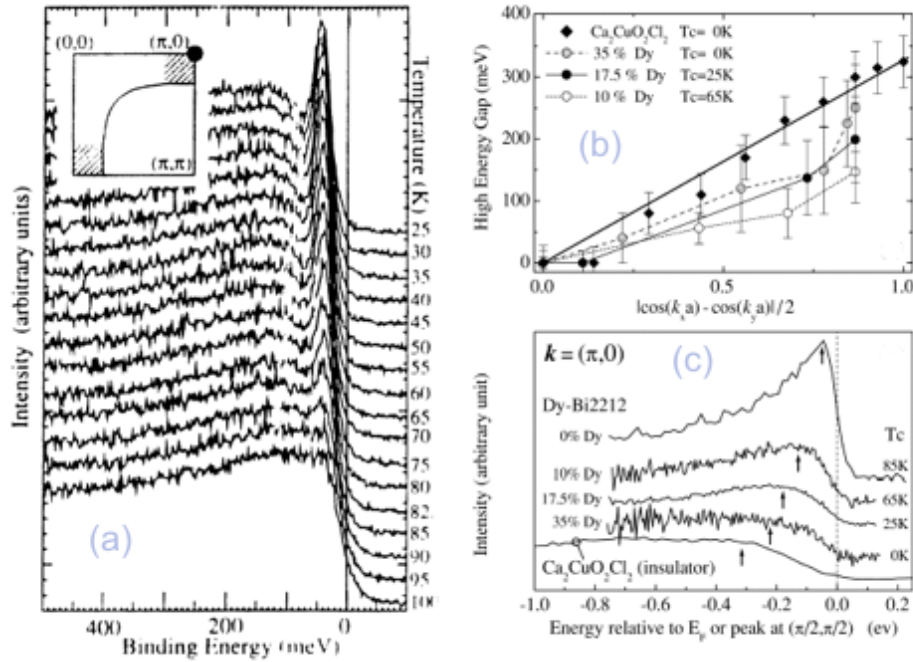


Figure 3.3: ARPES study of the PG in Bi2212 and Dy-Bi2212: (a) Temperature dependence of photoemission spectra at  $k = (\pi, 0)$  point [42]. Sharp peak grows below  $T_c = 79$  K. Its energy does not change with temperature, suggesting that the gap does not close at  $T_c$ . Inset shows the Fermi surface.; (b)  $k$  dependence of the pseudo gap (peak position) [46] for different doping. It shows d-wave nature of the gap; (c) the quasi-particle peak corresponding to the PG for the crystals with different doping [46].

position in insulating  $Ca_2CuO_2Cl_2$  compound also shows the angular dependence so that the total gap is the sum of the Mott gap and the d-wave gap. The doping dependence of the PG is shown in 3.3(c). With increasing doping the QP peak becomes sharper and the peak position shifts toward low energies. It is similar to dependence of  $T^*$  on the doping. The amplitude of d-wave gap also decreases with increasing doping according to fig. 3.3(c), since the line becomes less tilted at high doping. Interesting result on optimally doped Bi2212 has been published in [47]. The sample has been measured with ARPES and AIPES (angle integrated photoemission), and the behavior of QP peak which is related to the PG has been observed. It was found that in ARPES the peak disappears at the temperature  $T^*$ , which is a bit higher than  $T_c$ . At the same time, in AIPES the peak exists up to temperature about 200 K. The AIPES measures the intensity integrated over all possible  $k$ , and therefore it measures some kind of an averaged d-wave gap over the Brillouin zone. The authors of that paper speculate about existence of two

pseudo-gaps, the first large one being associated with the temperature  $200K$ , and the second small one with  $T^*$ . So, there are many controversial interpretations of the ARPES data. The latest ideas can be found in [48]. Two facts concerning ARPES data are presently more or less established: the gap does not vanish at  $T_c$ , and the gap has a momentum dependence assembling d-wave symmetry.

### 3.3 Scanning tunnelling spectroscopy and microscopy

The PG in HTSC can be also measured by tunnelling spectroscopy. Tunnelling spectroscopy measures the density of states near the Fermi level (see fig 3.4).

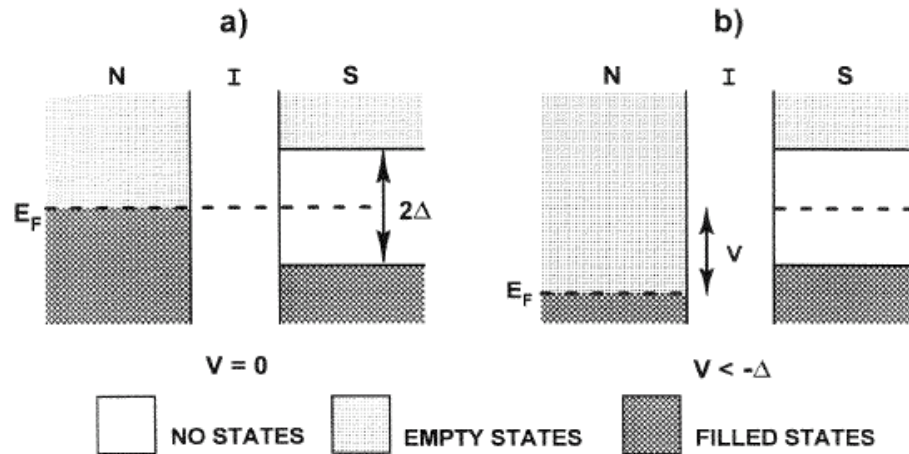


Figure 3.4: Tunnelling spectroscopy: at zero voltage no current flows between normal metal and superconductor fig. (a); if  $V < -\Delta$  electrons from the filled states in superconductor flow into empty states of the metal above Fermi level, and the current is proportional to the difference  $V$  and  $\Delta$ . [42].

Usually, a sample consist of two layers: an insulating layer grown on the superconductor and a normal metal layer or superconductor on top. If no voltage is applied to the metal and the two systems are in equilibrium, then their Fermi levels are equal. If an external voltage is applied to the metal so that it exceeds  $\Delta/e$ , the electrons tunnel from the metal through the insulator to the unoccupied states in the superconductive layer. A peak in the density of states was observed just above the gap edges for the case of ordinary superconductors. This means that the peak in the tunnelling conductance can be observed near the voltage  $eV = \Delta$  (see fig 3.5). If one changes the polarity of the voltage then the electrons

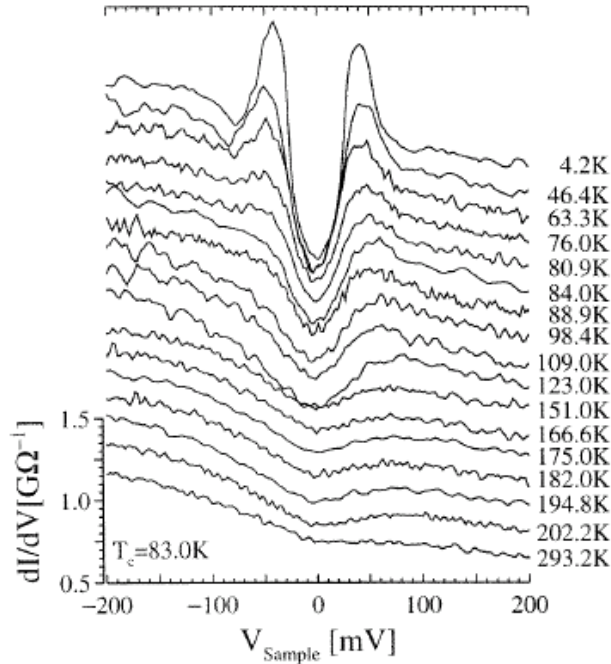


Figure 3.5: Pseudogap in tunnelling conductance: a feature at zero bias which vanishes well-above  $T_c$  is interpreted as the PG[42].

tunnel in the opposite direction: from the superconductor to the metal, and there will be a gap in the conductance with the width  $2\Delta$  centered on the Fermi level at zero bias.

A similar technique is tunnelling microscopy (STM). It allows to obtain the atomic scale images of the crystal surface. The principle of STM is as follows: a very sharp needle (so that only single atom projects from its end) is moved in a controlled fashion close to the surface of the crystal. Under small external voltage the tunnelling current appears as the needle approaches the surface. There is quite a strong interaction between the atom at the end of the needle and the electron cloud of the surface atoms. By scanning the whole crystal surface one can obtain an image in atomic resolution. With STM one can measure the PG locally on specific points of the surface, while ordinary tunnelling spectroscopy only provides the information about integrated current over the entire active surface area. In HTSC, because of the short coherence length, the tunnelling probes the density of states only within a few atomic layers near the surface. Therefore, these measurements require an extremely high quality of the surface. The most reliable results are obtained from experiments where the tunnelling barrier has been prepared by vacuum cleaving.

Most of the tunnelling experiments were performed on Bi2212 crystals. This allows comparing the results with ARPES data. So, recent STM measurements [49] reveal that the electronic states at low energies within the PG exhibit spatial modulations having an energy independent incommensurate periodicity. The re-

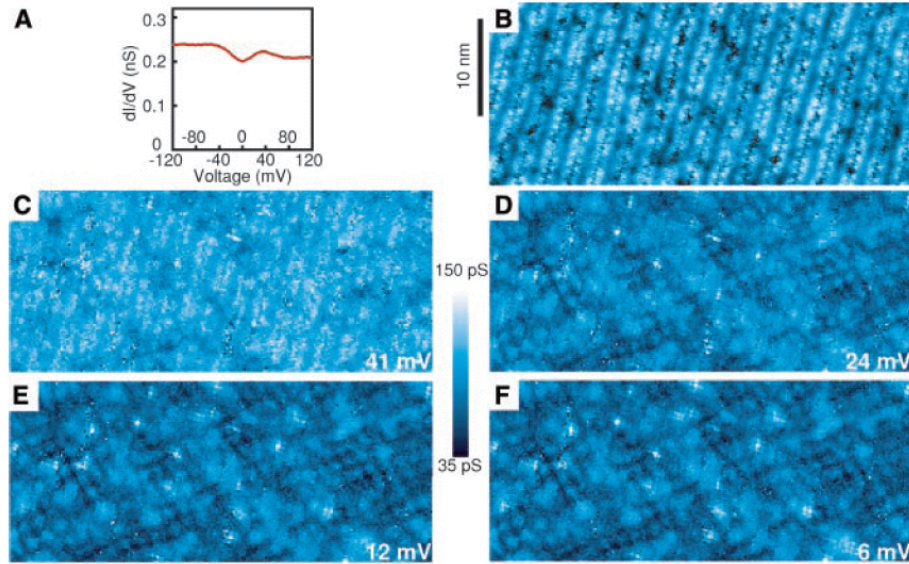


Figure 3.6: STM measurements of density of states (DOS) for Bi2212. Spatial dependence at 100K is shown. The measurements were taken using a standard ac lock-in technique with initial tunnelling current  $I_T$ , initial sample bias  $V_S$ , and bias modulation 4mV rms. (A) typical conductance spectrum ( $I_T = 100pA$  and  $V_S = -150mv$ ) shows the PG at Fermi energy; (B) A typical STM topograph taken at constant  $I_T = 40pA$ ,  $V_S = -150mv$  over  $450\text{\AA}$  by  $195\text{\AA}$  field of view shows atomic corrugations and the incommensurate modulation along the b axis; (C,D,E,F) real space conductance maps recorded simultaneously at 41mV(C), 24mV(D), 12mV(E), and 6mV(E) show appearance and evolution of DOS modulation along the Cu-O bond direction. Also evident from these maps is the presence of electronic variations associated with defects (Zn and other) and the dopant inhomogeneity of the material system [49].

lation between the spatial modulation and the PG can be found if one calculates the 2D Fourier transform to obtain the dependence of the Fourier amplitude on the in-plane wave vector. One can distinguish three kinds of peaks on the Fourier transform diagram: peaks corresponding to atomic sites, secondary peaks corresponding to the b axis incommensurate structural modulation, and the peaks along the  $(\pi, 0)$ ,  $(0, \pi)$  directions. The last group of peaks is related to the PG. These peaks can be detected only if  $eV$  energy is less than  $\Delta_{ps}$ , and they increase in intensity with reduced energy. In real space the characteristic length of this

modulation associated with the PG is about  $4.5a_0$ , where  $a_0$  is the Cu-Cu distance. The characteristic period of this modulations is energy independent in the PG regime (but the intensity of the peaks depends on the energy), while in the superconductive state the length scale depends on the energy. This is supposed to be an important difference between the PG and the SC gap related modulations [49]. Interestingly, similar modulations have also been observed at low temperature inside vortex cores that are induced by an external magnetic field[70]. This observation suggests that the suppression of the SC state inside the vortex cores leads to the formation of the pseudogap state.

Doping dependence of the tunnelling spectrum is plotted in fig. 3.7. The gap is identified as the distance between two peaks. The temperature, at which spectrum was measured, is 4.2K (superconductive state).

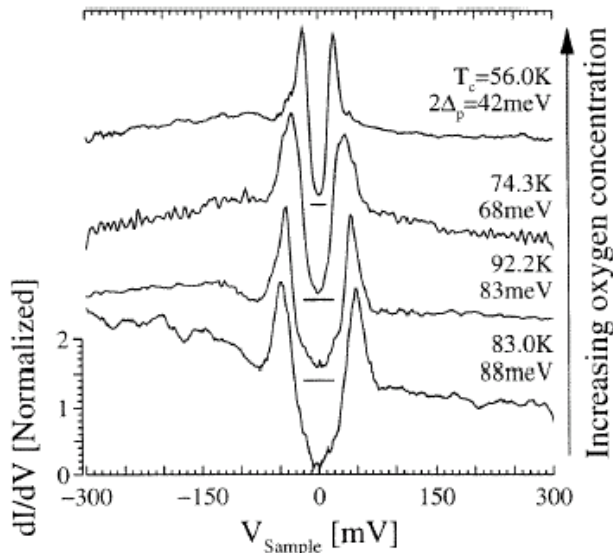


Figure 3.7: Doping dependence of tunnelling spectra of Bi2212 measured at 4.2K[42].

the half-width of the dip. It is about two times less than the distance between peaks, and can not be compared even with the leading edge gap. Note, that these two peaks also exist above in optimally doped and overdoped samples where they disappear right at  $T_c$ . This means that it is impossible to distinguish the pseudogap from the superconductive gap in the tunnelling data.

In conclusion, the STM data provide important information about the spatial

If we compare these data with ARPES results the same tendency is observed: with increasing doping the magnitude of the gap proportional to the distance between two peaks. However, the energy scale of the gap corresponds to the leading edge gap in ARPES, not to the peak positions (see fig. 3.3). The distance between peaks does not change with temperature in the superconductive state. This is also in agreement with the ARPES and optical conductivity data. The second possible determination of the pseudogap energy from the tunnelling spectrum is

modulation related to the pseudogap as well as about its energy scale and doping dependence. The tunnelling data are quite consistent with the results from ARPES and optical conductivity measurements.

### 3.4 Nuclear magnetic resonance NMR

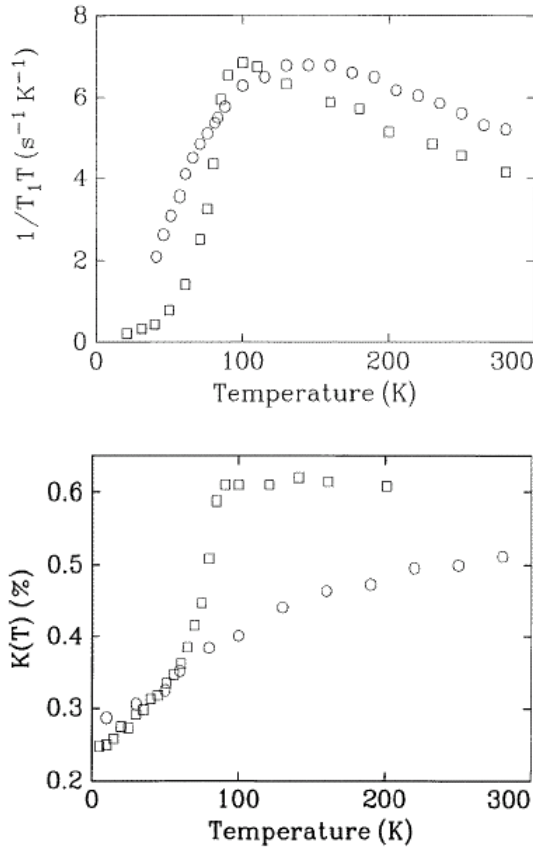


Figure 3.8: Top diagram shows planar Cu site spin-lattice relaxation rate in optimally doped  $YBa_2Cu_3O_{6.95}$  (squares) with  $T_c = 95K$ , and underdoped  $YBa_2Cu_3O_{6.64}$  (circles). Bottom diagram shows Cu Knight shift for the same samples.

Nuclear magnetic resonance spectroscopy is a powerful technique to study magnetic properties of solid state materials, which are related to the spin. The simplest, so called continuous wave NMR technique, corresponds to a radio frequency spectroscopy experiment in a magnetic field. In the framework of a quantum mechanical description the local magnetic field at the nuclear site leads to a Zeeman-splitting of the nuclear states according to different quantized values of the z-component of the nuclear magnetic moment. The energy is highest for those states where the magnetic moment of the nuclei opposes the magnetic field. The absorption of photons from the radio-frequency field is possible only if their energy corresponds to the Zeeman-splitting between these discrete nuclear levels. The absorption frequency is thus determined by the type of nucleus and the amplitude of the magnetic field at the nuclear site. In a continuous wave NMR experiment one measures this resonance frequency, either by scanning the frequency or by varying the magnetic field.

The local magnetic field at the nuclear site is determined by the sum of the

external field plus the field which arises from the environment in which the nucleus is embedded, for instance, in a metal the hyperfine interaction between the conductive electrons and the nuclei. This so-called Knight shift due to the polarization of the charge carriers was first observed by D. Knight [54]. In non-metallic materials the magnetic field from core electrons plays a similarly important role. This so called chemical shift is typically an order of magnitude smaller than the Knight shift in good metals.

If we consider the NMR signal on a macroscopic level we have to introduce the the net magnetization vector, which is proportional to the sum of the magnetization of all the nuclei in the sample. In a constant magnetic field this net magnetization has a large  $z$ -component which is parallel to the applied magnetic field while the transverse component is close to zero. In the so-called pulsed technique one applies a short pulse (the duration is inversely proportional to the Larmor frequency) of high intensity at the Larmor frequency such that the net magnetization is rotated into the  $x$ - $y$  plane. After this pulse the net magnetization will exhibit a free precession in the constant magnetic field. Dissipative processes will lead to a relaxation of net magnetization back to the ground-state with the magnetization parallel to the  $z$ -axis. The time scale for the recovery of the  $z$  component of net magnetization vector is called the spin lattice relaxation rate,  $1/T_1$ . The relaxation time of the transverse component contains contributions from the dynamics processes, i.e. from  $T_1$ , as well as from the de-phasing effects of the individually precessing moments due to a static variation of the local magnetic fields at the different nuclear sites which is usually described in terms of the spin-spin relaxation rate,  $1/T_2$ .

In theory, the Knight shift is proportional to the real part of spin magnetic susceptibility and indicates the spatially uniform polarization of the electrons in a magnetic field. The spin-spin relaxation rate is related to the spatial variation of the real part of the spin susceptibility. The spin lattice relaxation rate is related to the imaginary part of electronic spin susceptibility and thus provides valuable information about the spin fluctuations. The  $k$ -space dependence of the contributions of the susceptibility of both relaxation rates depends on the particular nuclear site as well as on the structure of the magnetically ordered state or the magnetic correlations.

The signatures of the pseudogap have been observed in the Knight shift as well as in the spin-lattice relaxation rate. In figure 3.8 these two quantities are

displayed for optimally doped and underdoped YBCO crystals. The Knight shift of the underdoped sample evidently decreases with reduced temperature in the normal state signalling a corresponding decrease in the low-energy spin-excitation spectrum. In contrast for the optimally doped sample the Knight shift is nearly T-independent in the normal state in good agreement with the Fermi-liquid models.

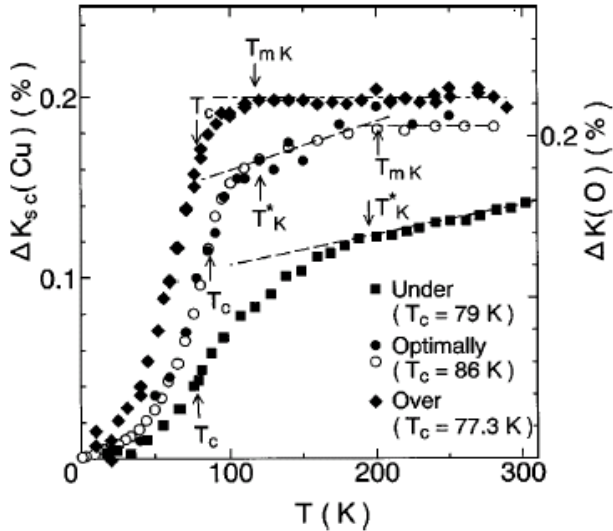


Figure 3.9: Knight shift for underdoped, optimally doped, and overdoped Bi2212[61]

For the underdoped sample it is clearly seen that the maximum in the relaxation rate is shifted towards high temperature, i.e. well above  $T_c$ . Both features, the T-dependence of the normal state Knight shift and the shift in the maximum of the  $1/T_1T$  relaxation rate have been interpreted in the framework of the pseudogap phenomenon. The Knight shift data are commonly interpreted in terms of the suppression of the low-energy density of electronic states due to the formation of the pseudogap. The deduced trends indeed seem to agree reasonably well with the ones obtained from other spectroscopic techniques. Concerning the interpretation of the spin-lattice relaxation rate the situation clearly is more difficult and subject of controversial discussion.

Further NMR investigations have found the pseudogap is also present if one looks on the spectra of Y and O nuclei in the YBCO compound [58, 59, 60]. These authors claim that the Cu 3d states and O 2p states form a unique spin system while the Y nuclear spins are most strongly coupled with the spin density

The spin lattice relaxation rate ( $1/T_1T$ ) also exhibits a characteristic T-dependence. In the optimally doped sample it exhibits a continuous increase with decreasing temperature in the normal state before it sharply decreases below  $T_c$ . The increase in the normal state has been attributed to magnetic fluctuations, which are enhanced with decreasing temperature but suddenly become suppressed with the onset of the superconductive energy gap. For the underdoped sample it is clearly



of the O 2p states. The doping dependence of the NMR Knight shift and the

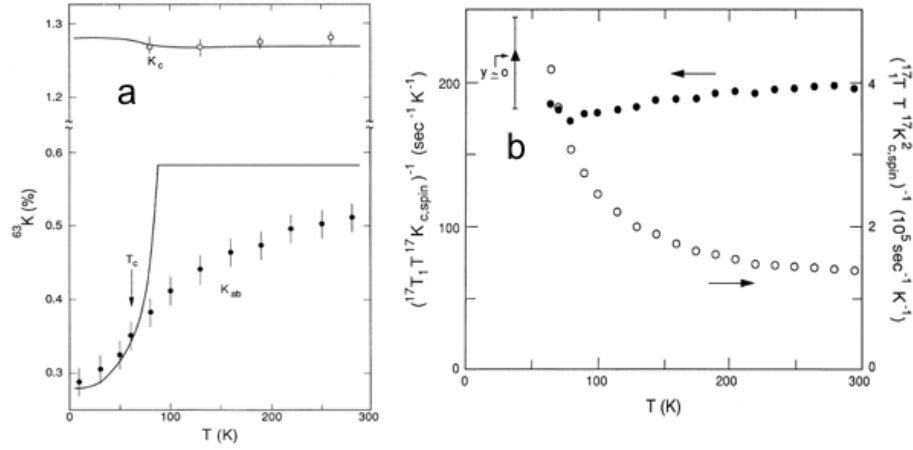


Figure 3.10: In-plane Cu Knight shift for different directions of the magnetic field and for different doping - figure (a).  $K_c$  is for underdoped  $\text{YBa}_2\text{Cu}_3\text{O}_{6.63}$  and field is along  $c$ -axis.  $K_{ab}$  is the same underdoped compound, the field is in  $ab$  plane. Solid line is the  $K_{ab}$  for overdoped  $\text{YBa}_2\text{Cu}_3\text{O}_7$ . Figure (b): spin lattice relaxation time for underdoped (open circles) and overdoped (filled circles) compounds. Results are taken from [60]

relaxation rate are shown in fig. 3.10. In the underdoped regime the pseudogap is seen only if the magnetic field is parallel to the  $ab$  plane. The  $c$ -axis Knight shift is almost temperature independent in YBCO. In the Bi2212 compound the Knight shift  $K_c$  behaves similarly to  $K_{ab}$  [61] (see fig. 3.9). A pseudogap in Knight shift also exists only in underdoped samples. The spin lattice relaxation time is nearly temperature independent in the overdoped regime, while in the underdoped regime it exhibits an increase below the pseudogap temperature  $T^*$ . This doping dependence of the relaxation time indicates that anti ferromagnetic spin fluctuations weaken as a function of the hole doping of the samples.

### 3.5 Raman scattering

Raman scattering is an inelastic light scattering technique. One distinguishes two kind of processes: in the so-called Stokes scattering an incoming photon is absorbed by the material, a phonon or another kind of internal excitation is created and finally a photon with lower energy is emitted. In the Anti-Stokes scattering the energy of the emitted photon is higher than the one of the incident photon. In this case an internal excitation is absorbed yielding the additional energy of the

emitted photon. This kind of second-order inelastic light scattering effect has been observed for the first time by C.V. Raman [69]. Its intensity is orders of magnitude weaker than the first order Rayleigh scattering which contributes to the optical conductivity.

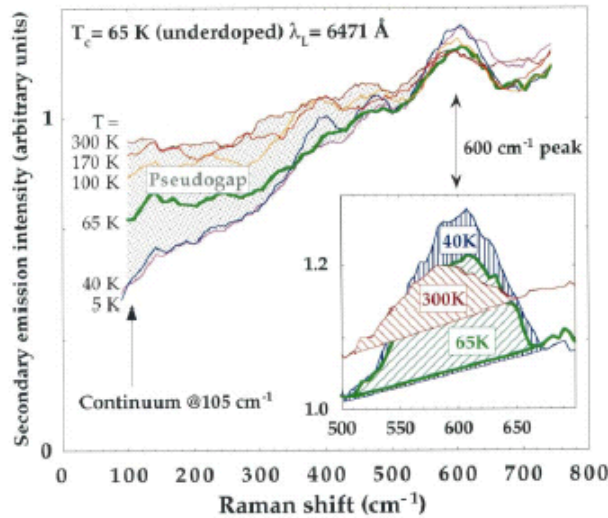


Figure 3.11: Electronic conituum measure by Raman scattering for underdoped  $T_c = 65K$  Bi2212 as a function of temperature[68]

associated with the anomalous T-dependence of a broad peak around  $600\text{cm}^{-1}$  which most likely cannot be associated with a phonon mode but rather must be assigned to excitations of electronic and/or magnetic origin. This peak hardly depends on the energy of incident photon, but rather on the polarization state of the incident and scattered light. With decreasing temperature the amplitude of the peak increases, and it becomes sharper. At the transition temperature  $T_c$  the integrated intensity of this peak exhibits a further sudden enhancement.

### 3.6 Specific heat measurements

Specific heat measurements are usually carried out using calorimeters, which are thermo-isolated systems where one can determine the temperature transfer between two substances without energy leak. If the specific heat and mass of a reference material, the initial temperature difference, and mass of a sample

The Raman spectrum of HTSC consists of several phonon modes and a continuum that arises from the electronic excitations. The pseudogap shows up in terms of a suppression of the electronic excitations below  $T^*$ . It shows up in the electronic background in similar fashion as in the infrared conductivity in the form of a suppression of the electronic Raman response below the characteristic pseudogap energy scale (see fig. 3.11).

The PG phenomenon in Raman scattering has also been associated with the anomalous T-dependence of a broad peak around  $600\text{cm}^{-1}$

are known, the specific heat coefficient can be calculated using the first law of thermodynamics.

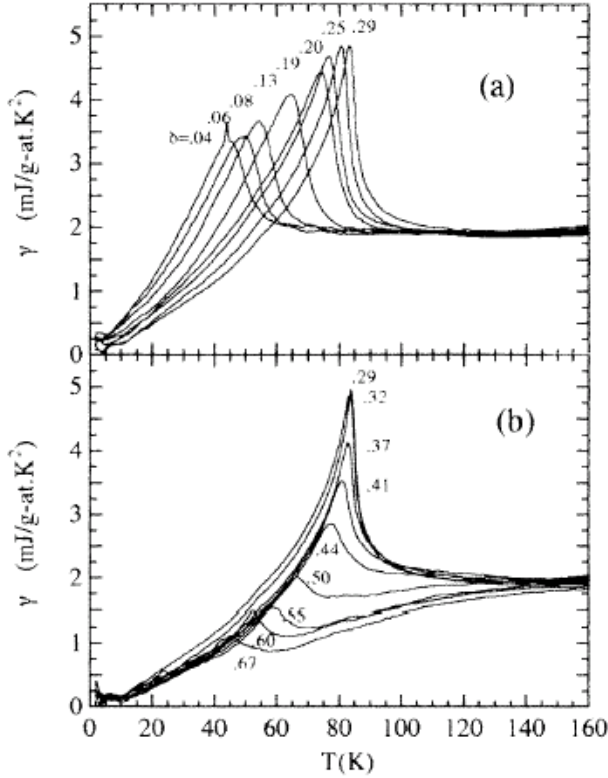


Figure 3.12: Specific heat coefficient of  $Y_{0.8}Ca_{0.2}Ba_2Cu_3O_{7-\delta}$ . Figure (a) corresponds to overdoped side  $\delta < 0.29$ , figure (b) is underdoped side  $\delta > 0.29$ [42]

To observe the pseudogap one needs to separate the electronic part of the specific heat from the total specific heat, which is dominated by the phonon contribution especially at higher temperature. This separation poses a severe experimental problem to the reliable determination of the T-dependent changes of the electronic part of the specific heat. To overcome this problem several groups have performed difference measurements with respect to a non-doped system, i.e. the insulating  $YBa_2Cu_3O_6$  in case of the Y123, where the free carrier concentration is absent. The obtained temperature dependence of specific heat coefficient of several YCa123 poly-crystalline samples is displayed in fig. 3.12 for different doping levels. The weight of

the peak at  $T_c$  can be directly related to the gain in condensation energy in the SC state. In the normal state, within a Fermi-liquid approach, the electronic specific heat,  $\gamma$  should remain temperature independent representing the density of electronic states at the Fermi-level. Such a trend is indeed observed on the overdoped side as shown in Fig. 3.14a. In clear contrast on the underdoped side  $\gamma$  can be seen to exhibit a pronounced T-dependence already well above  $T_c$ . This decrease is associated with the pseudogap and interpreted as a partial suppression of electronic excitations. It starts at  $T^*$  and has a similar doping dependence like the normal state pseudogap as seen by other spectroscopic techniques.

## 3.7 Other techniques

Finally we mention some further techniques which have been applied to study the energy scale and the evolution of the normal state pseudogap.

### 3.7.1 Andreev reflection spectroscopy

An electron can travel through a metal superconductor interface only under the condition that it combines with another electron of opposite spin on the normal metal side to form a Cooper pair. It will thus leave behind a hole of opposite spin in the normal metal. This Andreev reflection happens only if the superconductive condensate is formed, and it will enhance the conductance of the metal-superconductor contact. G. Deutcher et al [57] compared tunnelling spectroscopy

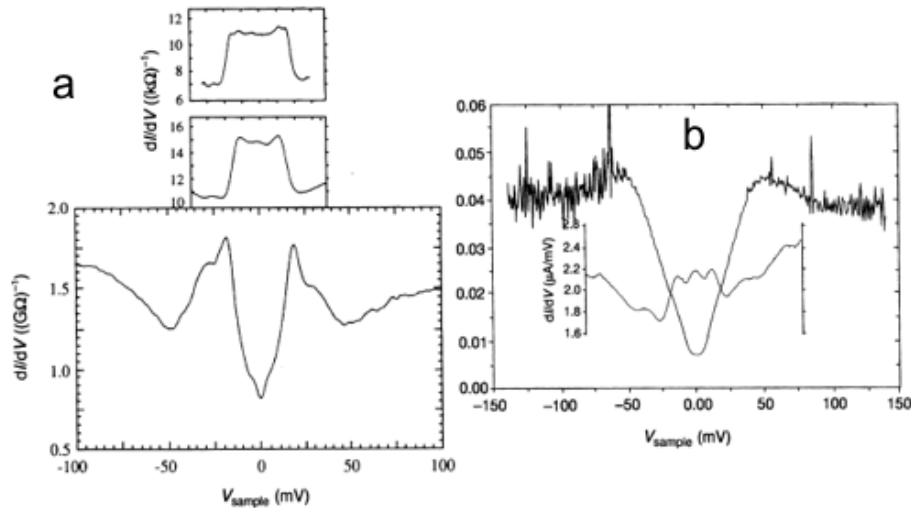


Figure 3.13: Andreev spectroscopy data and tunnelling spectroscopy data for optimally doped YBCO (a), and for underdoped YBCO (b). Modified picture from [57].

results with Andreev spectroscopy and found that in the pseudogap regime the energy scales of the two spectroscopic techniques did not agree (see figure. 3.13). He interpreted this difference in energy scales in the following way. In tunnelling spectroscopy one measure the energy required to break up a Cooper pair into independent quasi-particles, whereas in Andreev spectroscopy the relevant energy scale is given by the coherency energy, i.e. the energy required to break the macroscopic coherence between the Cooper pairs. Their observation implies that in underdoped samples these two energies are not identical. With decreasing

doping the difference between these two energies increases. In the spirit of their interpretation the pseudogap would be interpreted in terms of preformed Cooper pairs which cannot maintain phase coherence above  $T_c$ .

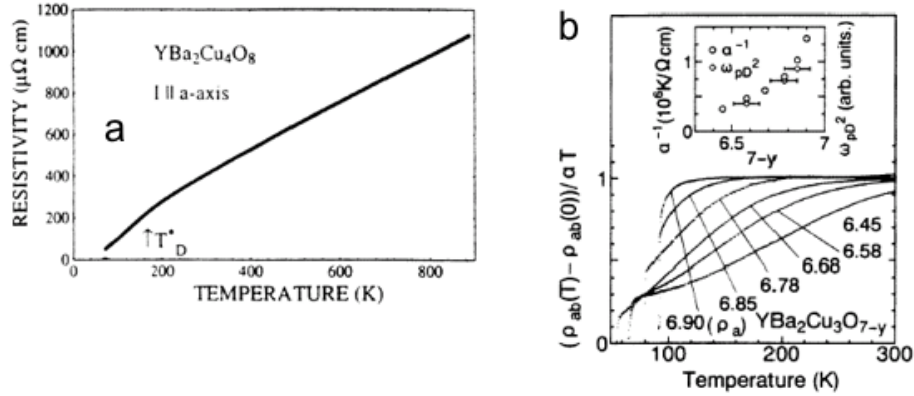


Figure 3.14: Pseudogap in dc resistivity (a), and doping dependence of dc resistivity (b) [42].

### 3.7.2 DC resistivity

The signatures of the pseudogap have also been identified in dc resistivity measurements based on anomalous changes in the temperature dependence. For instance, in the in-plane resistivity of underdoped samples frequently a small kink is observed at  $T^*$  (see fig. 3.14). The doping dependence of  $T^*$  deduced from the resistivity kink is consistent with  $T^*$  measured by infrared ellipsometry (see chapter 2) and with the phase diagram of YBCO.

## 3.8 Interpretations of pseudogap

### Stripes

Within the stripe theory the pseudogap is the result of strong spin and charge fluctuations in the underdoped regime. It assumes that the charge carriers segregate forming quasi one-dimensional regions with high hole concentration and others with low hole concentrations. The driving force is the avoided frustration of the AF-exchange coupling in the hole poor regions. Counteracting are the Coulomb force as well as the reduced kinetic energy of the charge carriers. The pseudogap in this scenario can be explained in terms of a two liquid model

where there are superconductive stripes and non-superconductive stripes. With decreasing temperature the number of superconductive ones increases. There are also arguments against this model. First, no correlations between pseudogap characteristics (energy, temperature) and observation of stripes have been found. Secondly, stripes do not produce the same angular dependence as the pseudogap in ARPES data. Third, there are difficulties to explain the high energy of the pseudogap using the stripe scenario.

### **Anti-ferromagnetic fluctuations**

A complete description of this theory can be found in [63]. The basic idea is that short range anti ferromagnetic fluctuations play an important role in the underdoped and optimally doped regime. With increasing doping these fluctuations become weaker and begin to ease on the overdoped side. It is possible to explain the existence of the pseudogap using the anti-ferromagnetic Fermi liquid model, which operates with two kinds of quasi particles: so-called hot quasi-particles and cold quasi-particles [63]. Only the hot quasi particles are strongly coupled to spin fluctuations. The difference between optimally doped and underdoped regimes is explained in terms of the reduction of the number of hot quasi-particles in the underdoped regime. The pseudogap is thus a consequence of the increasing of spin fluctuations in underdoped regime. According to this model the pseudogap is unrelated to superconductivity. Arguments against this model are, in principle, similar to the ones against the stripe idea.

### **Superconductive fluctuations and preformed Cooper pairs**

This theory tries to link the pseudogap with the superconductive gap since both of them have a similar energy scale and the same d-wave like k-space dependence. The pseudogap is thought of as some kind of incomplete or partial superconductive gap. Cooper pairs are formed here well above  $T_c$ , but a macroscopically phase coherent SC state appears only below  $T_c$ . Responsible for the suppression of phase coherence are thermal phase fluctuations which can become very strong if the amplitude of the SC order parameter is fairly small or spatially strongly inhomogeneous, accordingly the transition temperature reduces from  $T^*$  to  $T_c$  [64]. However, GHz conductivity measurements [65] have shown that such a large phase incoherence can be reached only well above  $T^*$ , and this is the most important experimental argument against this theory. The second theoretical

idea was that the coherence length or the size of a Cooper pair is too small so that the superconductivity appears only at  $T_c$  when the temperature fluctuations are small enough. However, this contradicts the measurements of the coherence length [118].

### **Spin charge separation scenario**

In 1D systems one can consider independently spin and charge parts of the Hamiltonian. This is called spin charge separation scenario. One introduces the quasi-particles, which have a spin but no charge, and others, which have a charge, but no spin. There are claims that such a scenario might be valid even in 2D systems. However, a mathematical proof does not exist so far. In this case, the charged particles (holons) are free to move, and the spin particles (spinons) are coupled into singlets. The pseudogap really is a spin gap here: it corresponds to the energy required to split the spin singlets. Indeed, the calculated energy of the spin gap is similar to the one of the pseudogap, ie. it is about  $100meV$ . Within this model it is more difficult to explain why the pseudogap manifests itself not only in spin channel but also in the charge channel. Evidently, one has to assume some kind of coupling between the spin and charge degrees of freedom. Details of such a coupling have not been demonstrated yet.

### **Quantum critical point**

This group of theories suggests that there is a quantum phase transition at the point on the phase diagram where a transition temperature goes to zero as a function of some order parameter. The transition should be between a phase with a certain kind of order or symmetry and a phase without it. To explain the pseudogap a quantum critical point near optimally doping state has been proposed. However, no order parameter has been found so far. Furthermore, it is not established what kind of symmetry is broken during this proposed quantum phase transition, and no singularities in thermodynamic properties have been observed around this point. An exotic idea[67] suggests that time reversal and four fold rotational symmetries are broken at the quantum critical point due to local ring currents between copper and oxygen ions, but the product of these two symmetries is preserved (see [67] for details). So far, no experimental confirmations of this idea have been found.

# Chapter 4

## Impurities

### 4.1 Introduction

Generally, impurities are some "foreign" ions, which are incorporated into the crystal in a controlled manner in order to change some of its properties. One should distinguish them from defects and imperfections of the crystal which are inherent to the crystal growth process and thus cannot be avoided or handled in a controlled manner. A classical example is the partial substitution of impurities with higher (lower) valency in semiconductors which thus act as electronic donors or acceptors and enable one to vary in a controlled way the number of electrons (holes) in the conduction (valence) band. A similar doping effect can be achieved in the superconductive YBCO compound if one substitutes  $Y^{3+}$  with  $Ca^{2+}$ . In combination with the oxygenation process this is a convenient way to adjust and control the hole content in this superconductor. Such impurities whose main effect is to change the hole content are usually called dopants.

In the case of the cuprate HTSC there is a second kind of impurities which have a profound effect on the normal state electronic and superconductive properties even though they hardly modify the hole doping state of the  $CuO_2$  planes. These are impurities like Zn, Ni that replace Cu ions within the  $CuO_2$  planes. It is meanwhile well established that these impurities hardly affect the hole doping, i.e. they maintain a similar 2+ valency like Cu. Unlike the cationic impurities which reside outside the  $CuO_2$  planes, these impurities lead to strong potential scattering of the charge carriers. This potential scattering introduces a k-space mixing of the electronic states and thus leads to severe destructive interference effects in the presence of a SC order parameter with a d-wave symmetry, i.e. for



the case of HTSC. It is indeed observed that only a few percent of non-magnetic Zn impurities are sufficient to fully suppress SC in the cuprate HTSC. The  $T_c$  suppression even seems to be more rapid for non-magnetic Zn-impurities than for the case of magnetic Ni-impurities. It has been argued that this difference arises from the tendency of Ni impurities in the 123 compound to partially occupy both the in-plane Cu(2) as well as the Cu(1) chain sites. To the contrary, Zn impurities have been shown to exclusively occupy the in-plane Cu(2) site in Y123 at least at small concentrations. The lower rate of  $T_c$  suppression in Ni-impurity substituted samples thus has been explained in terms of a much weaker pair-breaking effect from Ni-impurities on the Cu(1) chains site.

While the influence of these Zn and Ni impurities on the superconductive state has been studied in very much detail, the present work is mostly concerned with the corresponding impurity related effects on the pseudogap phenomenon. In particular, we have concentrated on the ground state properties once superconductivity is fully suppressed by introducing a sufficiently large amount of these pair-breaking impurities.

## 4.2 Theoretical background

There are two generic theoretical approaches to describe impurities: the effective mass method and the Greens function formalism. The effective mass theory reduces the problem to solving a Schrödinger equation with an effective potential, that accounts for the difference between the actual potential and the pure lattice potential. In this approximation, the complexity of the perfect lattice potential is represented by an effective mass and dielectric constant. The problem is thus reduced from a (N+1) body problem to an effective one body problem. This theory describes very well the case of donors and acceptors in semiconductors.

The second method is the so-called Greens function method, and it is more precise than effective mass approach. In this theory the impure system is described by the Greens function of the Schrödinger equation, in which one includes a local perturbation potential describing an impurity. In this approach one can consider magnetic and non magnetic impurities in magnetically ordered (ferromagnetic or anti-ferromagnetic) materials.

### 4.2.1 Effective mass method

The complete evaluation of the effective mass equation can be found in the literature [71]. Here we only specify the approximations involved in this method. The initial single particle Schrödinger equation to solve is

$$(H_0 + U)\Psi = E\Psi, \quad (4.1)$$

where  $H_0$  is Hamiltonian in the case of a perfect crystal,  $U$  is the perturbation potential due to the impurity. One can write the wave function  $\Psi(\mathbf{r})$  in the basis of the functions of the impurity free crystal like:

$$\Psi(r) = \sum_{n'} \int d^3k' \Phi_{n'}(k') \psi_{n'}(k', r), \quad (4.2)$$

where  $\Phi_n(\mathbf{k})$  are the amplitude functions. The perturbation potential can be also presented by its Fourier transform:

$$U(r) = \left(\frac{1}{2\pi}\right)^3 \int d^3U(k) \exp ikr \quad (4.3)$$

The electron wave function in the impurity-free lattice can be expressed through the Bloch functions  $\psi_n(k, r) = u_n(r) \exp ikr$ . Substituting  $\Psi$  and  $U$  in 4.1 we can deduce the following equation:

$$(E_n(k) - E) \Phi_n(k) + \sum_{n'} \int d^3k' \Phi_{n'}(k') \sum_m a_m^{nn'} U(k - k' + k_m) = 0, \quad (4.4)$$

where  $k_m$  are the reciprocal lattice vectors of the impurity-free lattice. At this point the following two approximations are made. First, the Fourier components of the potential outside the first Brillouin zone are neglected so that  $\sum_m a_m^{nn'} U(k - k' + k_m) = a_0^{nn'} U(k - k')$ . Second, we can eliminate interband terms  $n \neq n'$  so that  $a_0^{nn'} = (1/2\pi)^3 \delta_{nn'}$ . In this approximation 4.4 can be written in the form

$$(E_n(k) - E) \Phi_n(k) + \frac{1}{(2\pi)^3} \int d^3k' \Phi_n(k') U(k - k') = 0 \quad (4.5)$$

If one introduces the envelope function

$$F_n(r) = \int d^3k \Phi_n(k) \exp ikr, \quad (4.6)$$

equation 4.5 can be simplified to:

$$E_n(-i\nabla)F_n(r) + U(r)F_n(r) = EF_n(r) \quad (4.7)$$

Finally, if we substitute  $E_n = -\hbar^2/(2m^*)$  ( $m^*$  is the effective mass) we obtain the effective mass equation for the envelope function  $F(r)$ :

$$\left(-\frac{\hbar^2}{2m^*}\Delta + U(r)\right)F(r) = EF(r) \quad (4.8)$$

This substitution is only possible if the band is isotropic, parabolic, and non-degenerate. If these conditions are not fulfilled one has to use equation 4.7 directly. It can not be solved easily.

The potential  $U(r)$  can be taken in the form

$$U(r) = \frac{e}{4\pi\epsilon r} \quad (4.9)$$

if the electron cloud is much larger than the lattice constant. In this case, the equation 4.8 transforms to the equation of the Bohr hydrogen atom:

$$-\frac{\hbar^2}{2m^*}\Delta F(r) + \left(\frac{e}{4\pi\epsilon r} - E\right)F(r) = 0. \quad (4.10)$$

The corresponding energy levels are  $E_n = e^4 m^*/(32\pi^2 \epsilon^2 n^2 \hbar^2)$ .

We once more list the approximations of this method. Firstly, the interband term is excluded. That means the  $k$  vector is close to the minimum  $k_0$  and varies in a narrow range so that  $(\hbar\Delta k)^2/2m^* \ll E_g$  ( $E_g$  is the band energy gap). Secondly, the impurity potential  $U(r)$  varies slowly so that only its Fourier components in the first Brillouin zone need to be considered. Third, the band is isotropic, parabolic, and non-degenerate. Forth, we have hydrogenic type of impurity.

In practice, this theory works quite well for donor impurities in semiconductors. For most acceptors the valance band is degenerate and one can not use this simple equation. In this case, the more complex equation 4.7 has to be solved.

### 4.2.2 Green function method

The Greens function method is coming from the theory of linear response. Briefly, one considers the Hamiltonian  $H = H_0 + V$ , where  $V$  is small and can be treated as a perturbation. In this case, the expectation value of an observable quantity  $Q(t)$  in the ground state  $|G\rangle$  of  $H$  in the presence of the perturbation will be modified according to the ratio:

$$\langle G|Q(t)|G\rangle \rightarrow \langle G|U^{-1}(t)Q(t)U(t)|G\rangle, \quad (4.11)$$

where  $U$  is the evolution operator

$$U \propto \exp\left(-\frac{i}{\hbar} \int_{-\infty}^t V(t') dt'\right) \quad (4.12)$$

If one keeps only the linear terms in the Taylor expansion of the exponent the effect of perturbation to  $Q(t)$  simplifies to

$$\delta \langle G|Q(t)|G\rangle = \frac{i}{\hbar} \int_{-\infty}^t dt' \langle G|Q(t), V(t')|G\rangle. \quad (4.13)$$

Afterwards, one can introduce the "force"  $f(t)$  so that  $V(t) = f(t)Q(t)$ . Then, 4.13 assumes the form

$$\delta \langle G|Q(t)|G\rangle = \frac{i}{\hbar} \int_{-\infty}^t dt' f(t') \langle G|Q(t), Q(t')|G\rangle = \int_{-\infty}^t dt' f(t') \chi(t-t'), \quad (4.14)$$

where  $\chi(t)$  is the generalized susceptibility, a coefficient between the change of expectation value and the force. It should be a response function because of causality, i.e  $\chi(t < 0) = 0$ . The quantity  $\langle G|Q(t), Q(t')|G\rangle$  is the density matrix  $\rho(r(t), r'(t'))$  evaluated in the state  $|G\rangle$ . Single particle Green function is

$$G(r, t; r', t') = -i\rho(r, t; r', t'), \quad t > t' \quad (4.15)$$

The Greens function is also proportional to the susceptibility  $G(t-t') \propto \chi(t-t')$ . The Green's function can be presented as the matrix  $G_{mn}(E)$  if one uses the eigenfunctions of the stationary Schrödinger equation  $H\Psi = E\Psi$  as a basis. Then

$$G(r, r', E) = \sum_{mn} G_{mn}(E) \Psi_m(r) \Psi_n^*(r') \quad (4.16)$$

From 4.15 and 4.16 one can deduce the density of states  $g(E)$ :

$$g(E) = -\frac{1}{\pi} \text{ImTr}G(E), \quad (4.17)$$

Substituting 4.16 to the definition of Green function  $(H - E)G(r, r') = -\delta(r - r')$  one can find that

$$G_{mn} = \frac{\delta_{mn}}{E - E_m} \quad (4.18)$$

This ratio can be written in operator form if one introduces the Green function operator

$$G(E) = \frac{1}{E - H + i\delta}, \quad (4.19)$$

here  $i\delta$  is the small imaginary part, which is added because of the causality principle. The Fourier transform of the Green function should not have poles in the upper half-plane since  $G(t) = 0$  for  $t < 0$ .

If we consider the Hamiltonian  $H = H_0 + V$ , where  $V$  is due to impurities, the perturbation theory gives the following transformation of the Green's function operator  $G(E)$ :

$$G(E) = G_0(E) + G_0(E)V G(E), \quad G_{nm}(E) = G_{nm}^0(E) + \sum_{pl} G_{np}^0(E)V_{pl}G_{lm}(E), \quad (4.20)$$

where  $G_0$  is the Green's function of the unperturbed equation. Using 4.17 and 4.20 one can obtain the density of states  $g(E)$ . This is the basic idea of the Green's function method.

### 4.2.3 Some theoretical results

Next we consider some theoretical conclusions, which arise from the application of the Green's function method to different types of perturbation potentials and the initial unperturbed Hamiltonian  $H_0$ . The complete evaluation will not be presented here since the theory is quite complex and it is not the main purpose of this thesis. The complete evaluations can be found in [72].

First we consider the effect of a single impurity atom with  $V_{nm} = u_0\delta_{n0}\delta_{0m}$ . Such an impurity results in a density of states corresponding to a single impurity level, or virtual resonance level which depends on  $1/u_0$ , the density of states in the impurity-free crystal  $g_0(E)$  and the Green's function of the impurity-free crystal  $G_0(E)$ . This is illustrated in figure 4.1. Figure (a) shows  $1/u_0$ ,  $\text{Re}G_0(E)$ , and

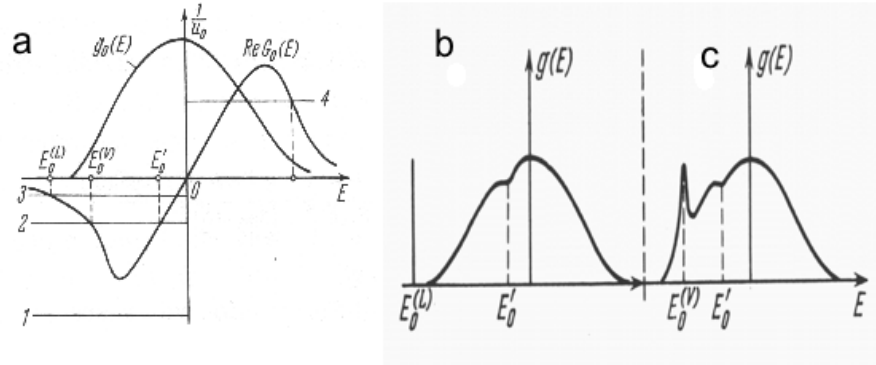


Figure 4.1: Density of states in a crystal containing a single impurity atom. From ref. [72]

$g_0(E)$ . If the  $1/u_0$  is large as illustrated in case 1 the line does not cross the one of  $Re G_0(E)$  and the density of states is not strongly modified by the impurity (case 1 in fig. 4.1 (a)). For scenario 2, we have two crossing points within the band  $E_0'$ ,  $E_0^{(V)}$  so the impurity produces a virtual resonance level that lies within the band corresponding to the peak at  $E_0^{(V)}$ .  $E_0'$ . Finally, for case 3 where the crossing points is outside the band one obtains a localized impurity level at  $E_0^{(L)}$ .

If one considers a single magnetic impurity atom in a ferromagnetic or an anti-ferromagnetic crystal, the spin exchange interaction and the impurity spin vector have to be taken into account. The important parameters are the ratio of spins  $S'/S$ , the ratio of the exchange integrals  $I'/I$  and the direction of the impurity spin. The prime denotes the impurity here. The symmetry of the crystal structure is also important, since it determines the number of atoms neighboring the impurity. These atoms play a major role in the interaction with the impurity. Although, the theory becomes more complex the results are, in principle, similar to the case of a non-magnetic perturbation: depending on the parameters  $S'/S$  and  $I'/I$  one gets either localized impurity levels or a virtual impurity resonance within the band.

If the concentration of impurities is high enough, the interactions between the impurity atoms has to be taken into account. It produces impurity bands instead of impurity levels.

### 4.3 Impurities in ordinary superconductors

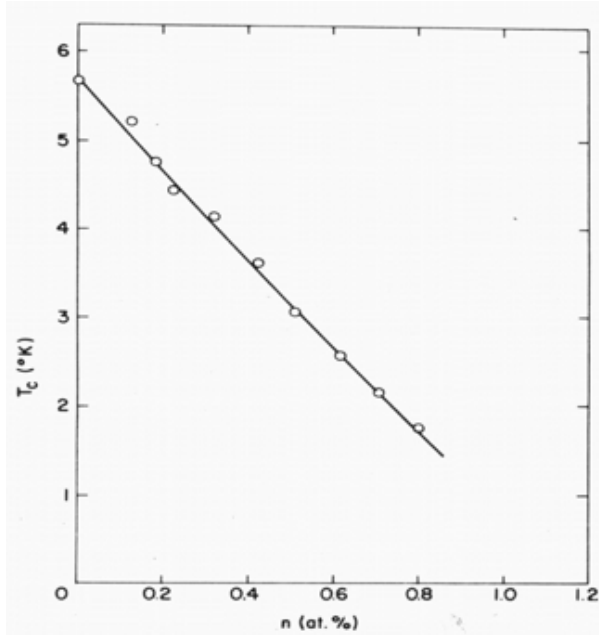


Figure 4.2:  $T_c$  versus Gd concentration in  $La_{1-x}Gd_x$  superconductor[75].

The key issue in ordinary superconductors related to impurities was the explanation of superconductivity in type II superconductors ( $Nb_3Sn$ ,  $Nb_3Al$ ) which contain impurities. This problem was independently solved by A.A. Abrikosov, L.P. Gor'kov [74], and P.W. Anderson [73]. Presently, it is known as Anderson theorem. It states that non-magnetic impurities do not give rise to pair-breaking effects, at least not as long as the concentration of impurities is low. At high concentrations, when the interaction between impurities becomes sizeable, superconductivity can be destroyed when the vibrations of the phonons exhibit large changes within the area of a coherence length. Magnetic impurities are active pair breakers and, therefore, even low concentrations of magnetic impurities rapidly destroy superconductivity (see fig. 4.2). At high concentration of paramagnetic impurities long range ferromagnetic order was observed [75].

Non-magnetic impurities play a fundamentally important role in the conventional superconductors only in terms of their influence on the vortex dynamics. Various kinds of impurities have indeed been investigated in terms of their ability to provide pinning centers which reduce the electromagnetic losses from vortex flow. These kinds of impurity induced effects on the vortex dynamics are also of great interest in the case of HTSC, but they will not be further discussed in this thesis.

## 4.4 Magnetic and non-magnetic impurities in HTSC

The effect of impurities in high temperature superconductors is presently not completely understood, in spite of the intensive theoretical and experimental efforts in this area. So far, three facts are more or less established. Firstly, non magnetic impurities suppress  $T_c$  at least as fast as magnetic impurities. This highlights that potential scattering in the presence of an unconventional d-wave symmetry order parameters and subsequent destructive interference effects play the major role in the  $T_c$  suppression. Secondly, non-magnetic Zn impurities are exclusively incorporated on Cu(2) sites within the  $CuO_2$  planes, while the magnetic Ni also partially occupy the Cu(1) chain site of the 123 structure. Third, both Zn and Ni impurities do not significantly modify the hole content.

In this section we summarize the experimental STM and NMR results. A detailed discussion of the neutron scattering data is not included here. It should be only briefly mentioned, that it was found that Ni and Zn have a rather different influence on the magnetic resonance peak as measured by neutron scattering. The addition of Zn strongly broadenes and increases the intensity of the resonance mode. The resonance mode furthermore does not sharply vanish any more at  $T_c$  but persists to elevated temperature  $T \ll T_c$  even in optimally and slightly overdoped samples. To the contrary, the Ni-impurities mostly lead to a red-shift of the resonance mode. The broadening and the weight gain of the mode is far less pronounced. The reason for this behavior is presently unknown [137].

### 4.4.1 Reduction of $T_c$

In high temperature superconductors the effect of magnetic and non-magnetic impurities is different than in ordinary superconductors. Obviously Anderson's theorem does not apply anymore: non-magnetic impurities like Zn are at least as effective in suppressing superconductivity as magnetic ones. The evolution of the superconductive transition temperature versus Ni and Zn impurity content is plotted in fig. 4.3. Two curves correspond to each compound. Evidently, Ni decreases  $T_c$  at a slower rate than Zn. Consequently, the lower curve always corresponds to the case of Zn. As discussed above, in YBCO there are two different Cu sites, Cu(2) on the planes and Cu(1) on the chains, which can be occupied by the impurities. Meanwhile it has been established that Zn goes



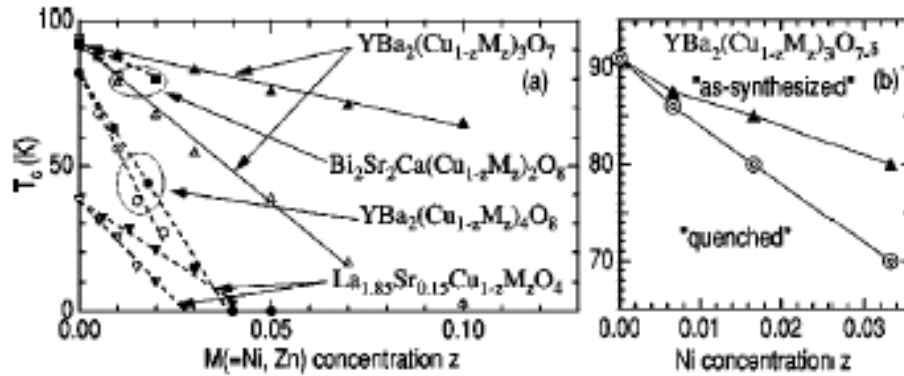


Figure 4.3: Superconducting transition temperature versus  $Zn$  and  $Ni$  concentration [50].

exclusively on the planes, while Ni tends to partially occupy both sites. The relative occupation of the chain and plane sites by Ni can in fact be modified during a high temperature annealing treatment in oxygen rich (Ni prefers the chain site) or oxygen poor (Ni prefers the plane site) environment. The reduction rate of  $T_c$  upon Ni substitution thus becomes dependent on the thermal history of the sample. This is nicely demonstrated in the right panel of fig. 4.3.

These results highlight that the main pair-breaking effect comes from impurities which give rise to strong potential scattering of the charge carriers within the  $CuO_2$  planes. This is closely related to the d-wave symmetry of the unconventional order parameter which changes sign in k-space. In the vicinity of the nodes (where the order parameter disappears and changes sign) the k-space mixing associated with the potential scattering thus can give rise to strongly destructive interference effects which lead to a very rapid suppression of superconductivity. From the experimental data it appears that the magnetic moment of the Ni-impurities plays a minor role in the  $T_c$ -suppression if any at all.

#### 4.4.2 Tunnelling spectroscopy results

As it was discussed in Chapter 3, tunnelling spectroscopy provides direct information about the density of states near the Fermi level. Tunnelling microscopy STM can produce atomic scale images of the crystal surface, measuring the tunnelling current at different points. Therefore, this technique is useful not only to study the pseudogap in pure samples, but to investigate the effect of impurities. It should be mentioned that most of STM experiments have been performed on

BSCCO single crystals.

First of all, it is necessary to mention that in real crystals there are also some natural defects, like missing Cu or O atom etc. Therefore, one investigates three things: magnetic Ni impurities, non-magnetic Zn impurities, and natural defects. The first feature being seen in STM is that there are regions with smaller and larger values of the local gap  $\Delta$ . If one puts impurities in the system the size of the area with a smaller value of the gap is increasing as shown in fig. 4.4. The STM image of the pure underdoped crystal is on the left side, and the image of the Ni impurity is on the right. One can see that the red area corresponding to the smaller value of the gap is much larger in the crystal with impurities. The typical size of this areas is about 2-3 nm. Variations of the local gap as large 100% are apparent.

STM can also resolve a single impurity atom in the crystal. STM images of BSCOO are shown in fig. 4.5. Zn and Ni impurities have characteristically different patterns in the STM image and different resonance levels in the density of states. The pattern near the Ni impurity looks similar to the pattern of a natural defect. Ni introduces two energy levels which are shifted from the center of the gap and are seen only at positive bias of the single atom site, and only at negative bias close to the nearest neighbor sites. This can be explained in terms of an electron hopping to the impurity site. It creates holes on the nearest neighbor atom. Due to the spin of the Ni we have two levels. Zn introduces one level, which lies almost at the center of the gap (at -1.5meV). Natural defects manifest themselves as a resonance level at the center of the gap.

Many theoretical investigations have been reported to explain the tunnelling and STM results as shown above. The resonance levels in the density of states can be explained using classical BCS theory with the assumption that the superconductive gap has d-wave symmetry in k-space[79, 80, 81]. The starting point of the model is a square lattice with one electron per site corresponding to the CuO plane in the underdoped compounds. The electron spins ( $S=1/2$ ) are anti-ferromagnetically correlated. The doping of the system with holes corresponds now to the creation of empty sites. Above a certain hole concentration the electrons will be able to hop from one site to another. In the vicinity of an impurity atom substituting for Cu, the interaction between impurity spin and the spin of electrons has to be taken into account. In addition, the potential scattering due

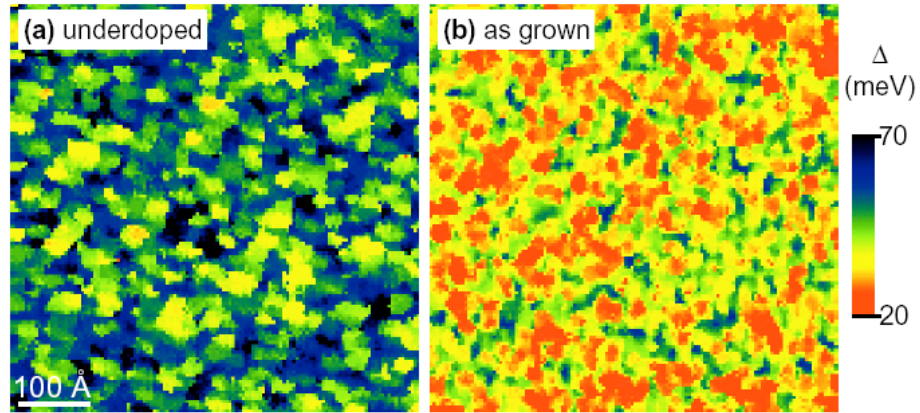


Figure 4.4: STM image of a pure underdoped BSCOO crystal (a), and an "as-grown" slightly overdoped crystal with 0.5% Ni (b). Figure from [77].

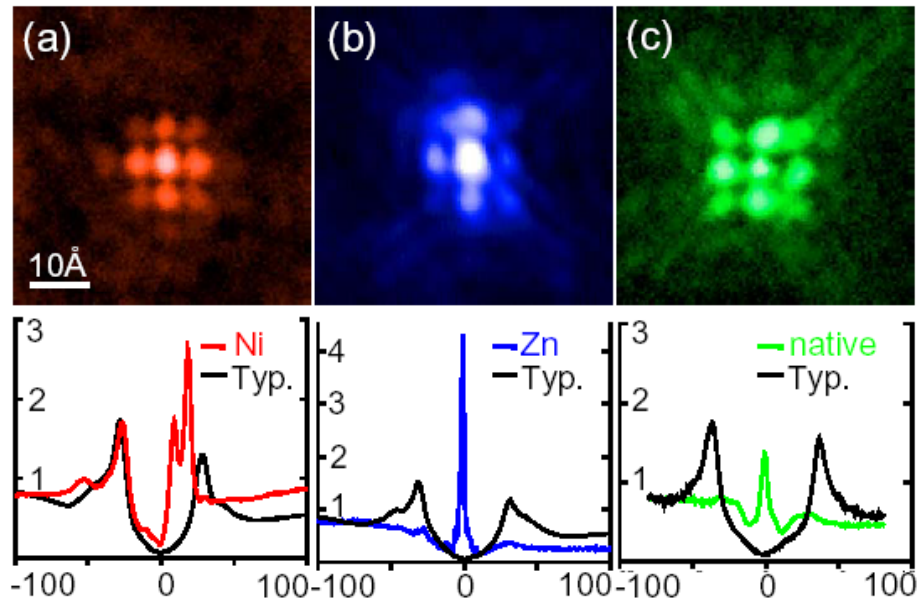


Figure 4.5: Local density of states map and tunnelling current near Ni(a), Zn(b), and natural defect (c). The size is  $50 \times 50 \text{ \AA}$ . Ni shows two resonances at +9 and +18 meV; Zn has resonance peak at -1.5 meV; Natural defects correspond to the peak at 0 eV. Slightly overdoped BSCCO crystals.  $T_c$  is about 85K. Black curve corresponds to the tunnelling current at the point far from an impurity. The impurity content is about 0.6% Zn, and 0.2% Ni. Figure from [77].

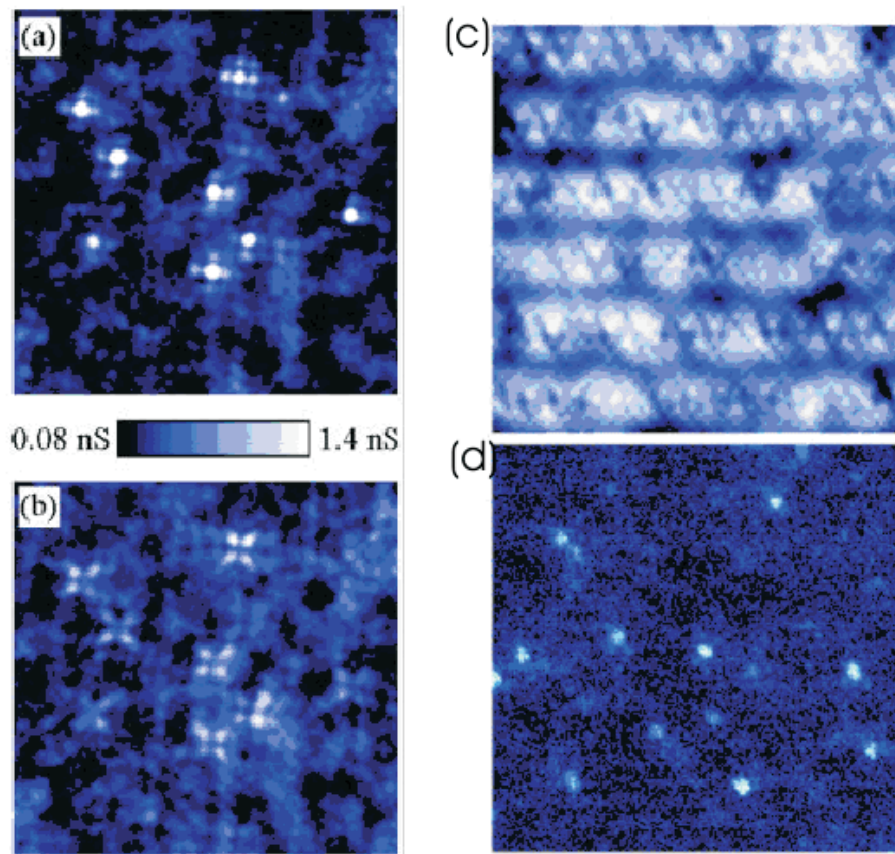


Figure 4.6: Local density of states map for Ni impurities (a, b), and Zn impurities (d) in BSCCO;  $T = 4.2K$ ; bias voltage is  $+9mV$ (a),  $-9mV$ (b),  $0V$  (d). (c) is the constant current topograph of the same Zn doped crystal. The current is  $100pA$ . Modified figure from [76]

to the different Coulomb interaction with the impurity has to be taken into account. Using the Green's function method and BCS theory one can thus calculate the density of states, and its spatial modulation. The result is shown in fig. 4.7. The frequency  $\Omega$  of the additional impurity levels depends on the magnitude of the superconductive gap  $\Delta_0$ , the density of states at the Fermi level per site  $N_F$ , the Coulomb energy of an electron orbiting the impurity ion  $U$ , and the energy of the magnetic spin exchange interaction between the electron and the impurity  $W$ . The approximate equation can be written as

$$\Omega = -\frac{\Delta_0}{2N_F(U \pm W) \ln [8N_F(U \pm W)]} \quad (4.21)$$

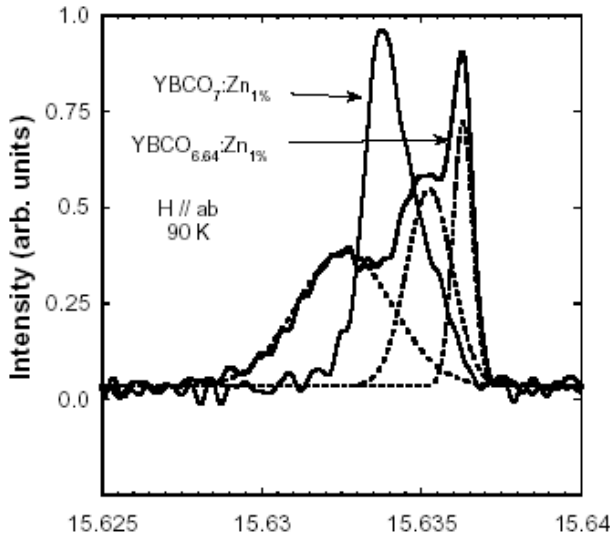


Figure 4.8: Y NMR spectra of Y123:Zn crystals[82]

Accordingly, non-magnetic impurities with  $W = 0$  create one additional level, while magnetic impurities with  $W \neq 0$  create at least two levels. In figure 4.7 the case of a non-magnetic impurity is shown. For Zn impurities, this model gives good results that are comparable with the experiment [78]. The spatial modulation of the local density of states should be symmetric relative to the nodes of superconductive gap as is shown in fig. 4.7b. This theoretically predicted modulation is not accurate enough for

the case of Zn impurities, but for Ni impurities it more or less coincides with the experimental results as plotted in fig. 4.6.

#### 4.4.3 NMR results

Nuclear magnetic resonance spectroscopy is a well suited technique for the study of magnetic effects caused by impurity atoms. The spin lattice relaxation time usually gives information about different kinds of magnetic correlations around

impurities. The amount of information may even be a bit too large and complex since a unique model that explains all the aspects of the NMR experiments in high temperature superconductors with impurities does not exist at present. Therefore, there are only several phenomenological interpretations of the experimental results. The situation is worse than with STM data where the effect of impurities can be approximately understood within d-wave BCS theory.

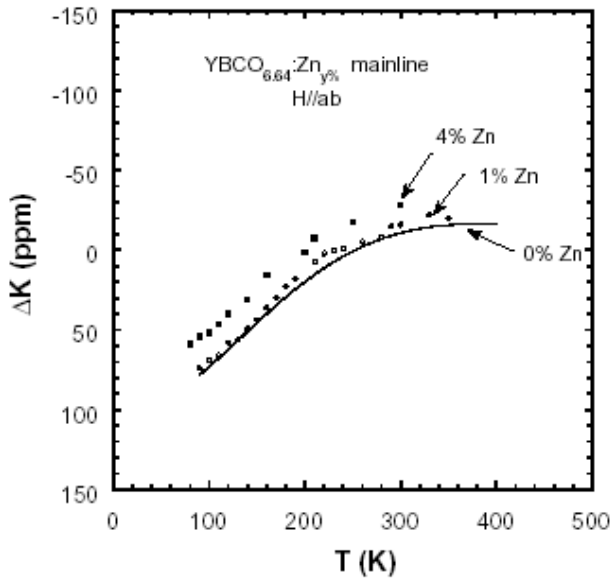


Figure 4.9: Knight shift of main Y line (Y nucleus far from impurity) in underdoped YZn123 sample.[82]

with a different local environment. For example, the outermost line, which is most effected by Zn, corresponds to nuclei neighboring a Zn impurity. The middle line accounts for the response from 2nd and 3rd nearest neighbors of the impurity. The most intense line comes from the nuclei, which are located further away from the impurity. The temperature dependence above 90K of these two impurity related peaks follows a Curie law with a negative hyperfine coupling constant. This is a common feature of local magnetic moments and implies that the magnetic Cu moments are enhanced in the vicinity of the Zn impurity. Interestingly, the Knight shift of the main Y line is almost unaffected by the Zn impurities (see fig. 4.9). Only at the highest doping level of 4% Zn can a slight offset be seen. Overall, this main line behaves rather similar as in the case of a

Mahajan[82] performed an extensive Y-NMR study of  $YBa_2(Cu_x, Zn_{1-x})_3O_{7-\delta}$ . They measured underdoped  $YBa_2Cu_3O_{6.64} : Zn$  and overdoped  $YBa_2Cu_3O_7 : Zn$ . The Zn concentration was varied up to 4%. The NMR spectra of these samples are shown in fig. 4.8.

The NMR line shape is strongly dependent of the oxygen content. For underdoped samples it can be fitted with three Gaussians. For overdoped samples one peak dominates the spectrum. First, we concentrate on the underdoped sample. It is shown that the three Gaussian lines arise from Y nuclei

pure sample without Zn. For the case of the overdoped sample the Knight shift of the single Y line also does not strongly depend on the Zn concentration.

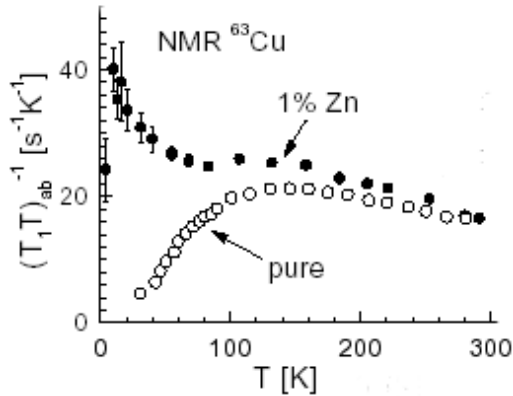


Figure 4.11: Cu relaxation rate of pure Y123 sample and for YZn123 sample. For the pure sample the absolute value of relaxation rate does not correspond to the Y axis but temperature dependence is reflected on the plot[83].

There are two important conclusions. Firstly, the Zn impurities enhance the magnetic moments of the nearest neighbor Cu atoms. Secondly, Zn impurities tend to weaken the spin fluctuations. Third, Zn goes exclusively in CuO planes. Fourth, the hole doping is not affected by Zn impurities, at least not in the dilute limit.

Similar conclusions can be made from the analysis of Cu NMR line in underdoped Y123 or Y124 (see fig. 4.10). The broadening of the Cu line is interpreted in terms of the presence of local moments near the Zn impurity [83]. The spin lattice relaxation rate increases with Zn substitution, its T-dependence becoming rather different from the one in the pure underdoped compounds. This makes an assignment of the pseudogap temperature  $T^*$  based on the relaxation rates rather difficult (see fig. 4.11). The evolution of the pseudogap with impurity substitution can in fact more safely be determined from the Y Knight shift. The same conclusions hold concerning the evolution of the pseudogap upon Ni substitution. Gaps determined from Knight shift and spin lattice relaxation time have different dependencies on the impurity concentration.

Next we consider in more detail the NMR investigations of Ni impurities. In contrast with Zn, Ni does not create any spin vacancies. Accordingly, the spin fluctuations are not suppressed by Ni impurities. NMR data have also been

The conclusion one can make from this is that the pseudogap determined from the Y Knight shift is not affected by the Zn impurities at concentrations below 4%. With increasing oxygen content the outer impurity peak merges with the middle line, and for an oxygen content close to optimum doping (6.92) the outer line fully disappears. There are two important conclusions. Firstly, the Zn impurities enhance the magnetic moments of the nearest neighbor Cu atoms. Secondly, Zn impurities tend to weaken the spin fluctuations. Third, Zn goes exclusively

interpreted in terms of an enhancement of the anti-ferromagnetic fluctuations near Ni impurities[84, 85]. However, there is no consensus about whether this enhancement is larger than in the case of Zn. The reason for this is washing out of the Y and O NMR line due to the Ni magnetic moments[100]. The second feature of Ni is that it goes also in the chains in Y123 crystals, while Zn goes exclusively in the planes.

A very interesting NMR study of Zn and Ni impurities in the Y124 system was reported by Itoh[86]. In this system the Knight shift of the Y main line does not significantly change its temperature dependence upon Ni substitution. The relaxation rate however changes from pseudogap like in pure samples to Curie like in impurity substituted samples. The pseudogap temperature vs impurity content is plotted in fig. 4.12.

The first line  $T_g$  in fig. 4.12 corresponds to the pseudogap determined from the Knight shift. The second line  $T_s$  is the pseudogap determined from the spin-lattice relaxation rate. For the details of this determination see chapter 3. The behavior of the pseudogap versus impurity concentration thus strongly depends on the way the pseudogap is observed. If one looks on the relaxation rate, the gap is suppressed in both cases of Zn and Ni impurities. It corresponds to the change in the behavior of relaxation rate from pseudogap like to Curie law like dependence. From the Knight shift, one concludes that Zn suppresses the PG much faster than Ni. From our infrared measurement, we conclude that the pseudogap increases with increasing of Ni concentration and is locally suppressed by Zn. This discrepancy can be related to the complex nature of the pseudogap, as well as to the difference in its experimental observations by different techniques. For example, reflectivity and NMR have different time scales. The time scale is orders of magnitude shorter in the optical data.

In conclusion, MNR experiments are interpreted in terms of the creation of local moments near impurities. However, this is still under discussion [87]. Ni is less effective in changing the low-energy spin fluctuations spectrum, while Zn leads to a strong suppression of these fluctuations. Both Ni and Zn do not so much affect the Knight shift of main Y line, while they strongly modify the T-dependence of the relaxation rate from pseudogap like to a Curie law.



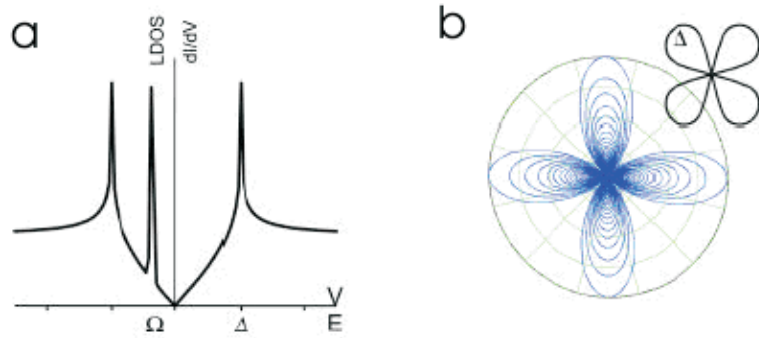


Figure 4.7: Tunnelling conductance (a) and spatial modulation of local density of states (b) obtained theoretically within BCS theory with d-wave gap in case of impurities. [76]

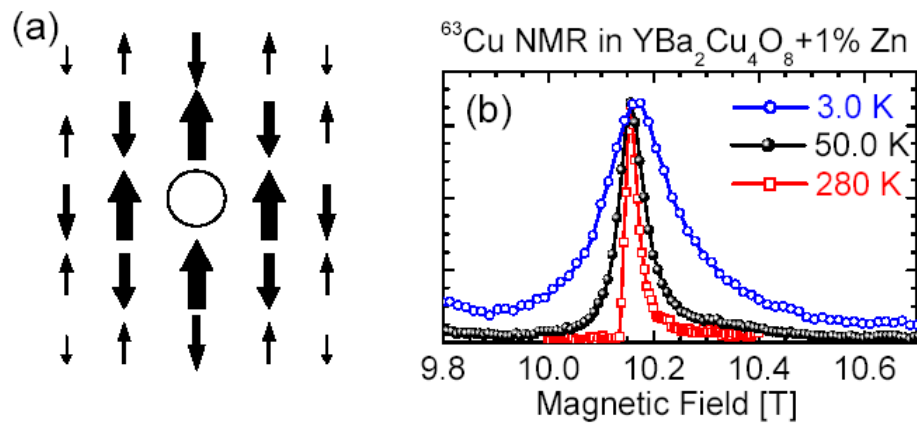


Figure 4.10: Localized moments near Zn impurity (a); Cu NMR line in  $\text{YBa}_2\text{Cu}_4\text{O}_8$  with 1%Zn (b)

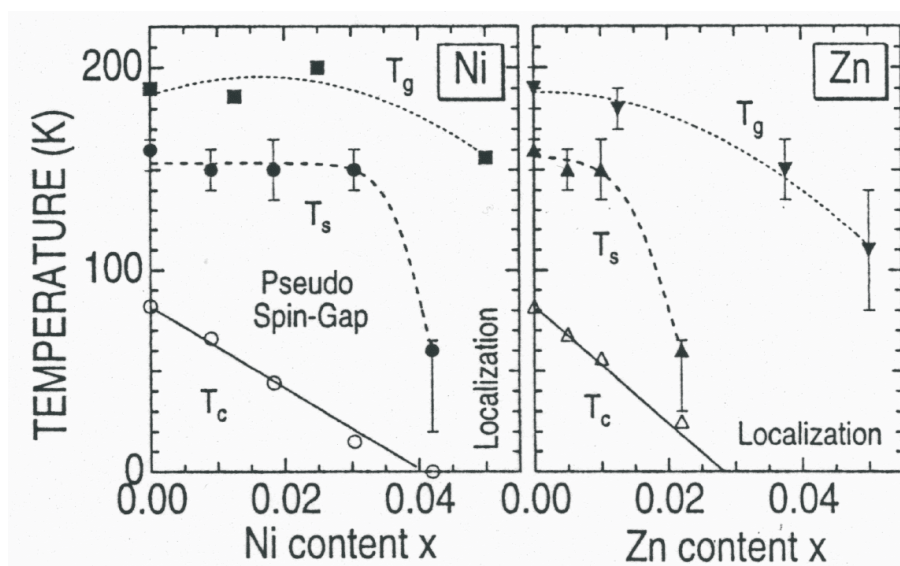


Figure 4.12: Pseudogap determined from Knight shift  $T_g$  and spin-lattice relaxation  $T_s$  rate depending on the impurity content in Y124 compound. [86].

# Chapter 5

## Influence of impurities on the pseudogap

### 5.1 Introduction

The influence of Zn and Ni impurities on the pseudogap has been previously investigated by a number of techniques like tunnelling spectroscopy [77], NMR [86], or Raman spectroscopy [99]. All these experiments have been performed on samples with concentration of impurities that are insufficient to suppress superconductivity completely. The persistent response of the superconductive condensate at low temperature therefore made it very difficult to differentiate whether the pseudogap is related to superconductivity or whether it is caused by another kind of mechanism. A definite answer can be expected only from measurements on entirely non-superconductive samples with high impurity concentrations. A second way to suppress superconductivity is by applying of a very large magnetic field. However, in the case of HTSC one finds that the upper critical field  $H_{c2}$  is of the order of 100 Tesla. The magnetic field approach therefore cannot be readily combined with spectroscopic techniques that probe the spectral shape of the energy gaps.

The second issue related to impurities, concerns their influence on the hole concentration. The variation of the hole content has been estimated from the thermoelectric power coefficient [95] as well as from the NMR Knight shift [82]. In specific case of Zn and Ni impurities, it was found that they do not change the hole content, at least not at small concentrations.

The present work was motivated by the recent discovery of Thomas Wolf that

large single crystalline samples of the 123 compound with very high impurity concentrations can be grown if instead of the Y ion one incorporates a larger rare earth elements like Nd or Sm. Using this approach it was possible to incorporate up to 9% of Zn and 17% of Ni impurities in the 123 structure. Even more importantly, it was found that the larger rare earth also assists the incorporation of a larger relative fraction of Ni on the Cu(2) site within the CuO<sub>2</sub> planes. This enabled us to prepare a series of underdoped to overdoped crystals where  $T_c$  could be completely suppressed either by Zn or Ni substitution. Subsequently, we performed optical studies of the evolution of the spectral gap in the c-axis response in order to investigate and possibly clarify the relationship between the normal state pseudogap and superconductivity.

## 5.2 Sample characterization by SQUID and EDX

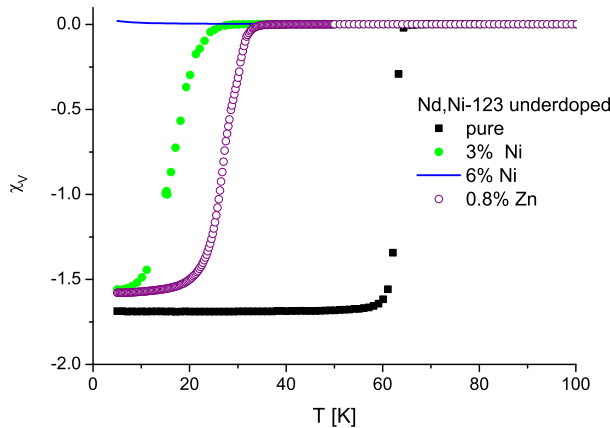


Figure 5.1: SQUID data for pure underdoped Nd123 sampled used in our ellipsometry experiments.

In the following paragraph we discuss the SQUID magnetometry and the EDX results on our Ni and Zn substituted  $(Sm, Nd)_{1-x}Ca_xBa_2Cu_{3-x}(Ni, Zn)_xO_{7-\delta}$  single crystals. While SQUID magnetometry provides information about the superconductive transition temperature  $T_c$  and the superconductive volume fractions, the EDX data give information about the stoichiometry and the impurity concentration of the crystals.

### 5.2.1 $T_c$ measurements by SQUID

A superconductive quantum interface device (SQUID) magnetometer is the most sensitive instrument to measure the magnetization of a given material [90]. Its sensitivity is about an order of magnitude higher than the one of conventional magnetometers. This is achieved by using superconductive wires in the

coil that picks up the change in magnetic flux due to a magnetized samples that is moved in and out of the coil. For our purpose, SQUID magnetometry is simply an accurate technique to measure the superconductive transition temperature  $T_c$  of our crystals and furthermore to determine the volume fraction that is shielded by the superconductive currents. All of our Ni and Zn substituted samples have been characterized by this technique. Representative data of the volume susceptibility are shown in fig. 5.1 for underdoped  $NdBa_2Cu_{3-x}(Ni, Zn)_xO_{6.8}$  with Ni content of  $x = 0, 0.03$  and  $0.06$  and Zn content of  $x = 0.01$ .

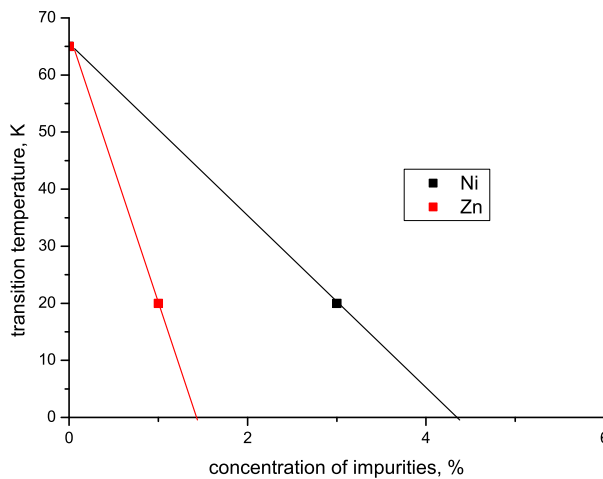


Figure 5.2:  $T_c$  versus Zn and Ni concentration for our series of underdoped Nd(Zn,Ni)123 crystals.

Due to reasons related to vortex pinning but also to possible inhomogeneity within the sample, the former (zfc) signal is more sizeable. Thus it provides a more sensitive test for any remnants of superconductivity that may remain in the heavily Ni and Zn-substituted crystals. Figure 5.2. demonstrates that this is not the case since any diamagnetic signal is absent already for the crystal with 6% Ni. Only a paramagnetic upturn in the magnetic susceptibility is observed here which arise predominantly from the magnetic Nd-moments but also from the Cu moments which tend to slow down and freeze in at temperature below 15 K depending on the Ni content (see  $\mu SR$ ). For the samples with lower impurity concentration

The data were taken with an external field of 10 Oersted using the so-called zero-field-cooled (zfc) mode where the sample is first cooled to the lowest temperature in zero-field before the magnetic field is applied. This probes how the shielding currents hinder the magnetic flux from entering the sample. Note that this is not the so-called Meissner-effect which is probed in the field-cooled mode when the super-currents have to expel the magnetic flux that has already penetrated the sample volume in the normal state above  $T_c$ .

we used the diamagnetic signal to determine the superconductive transition temperature and its width. Quoted are the temperature with half the diamagnetic signal as  $T_c$  and the 10 to 90% variation as the width,  $\Delta T_c$ .

The  $T_c$  dependence on the concentration of impurities for Nd(Ni,Zn)123 is shown in fig. 5.2. In agreement with previous reports it can be seen that Ni suppresses superconductivity at a slower rate than for the Zn impurities. About 1.5% of Zn and 4% of Ni impurities are required to suppress superconductivity completely for this specific oxygen content.

### 5.2.2 Measurements of impurity content by EDX

The EDX (energy dispersive X ray) analysis technique has been used to measure the impurity concentrations in our samples. EDX is usually a part of a scanning electron microscope. A sample is placed in the electron beam of the microscope. The electrons interact with the core electrons of the various ions inside the sample and induce excitation to higher levels. Subsequently, electrons from higher levels make a transition into this lower one. Thereby they reduce their energy by emitting an X-ray photon. The energy of this x-ray photon is characteristic of the element that is involved. The emission spectrum of these x-ray photons is recorded. It contains specific maxima that are thus characteristic of the particular ions that are incorporated in the crystal. Furthermore, the relative intensities of these peaks can be used to determine the stoichiometry of a given sample. More details about the EDX technique can be found in the literature [91]. The EDX spectrum of a  $(Sm, Y, Ca)Ba_2(Cu, Ni)_3O_7$  crystal is shown in fig. 5.3. It contains several lines per element corresponding to the different possible transitions of the core electrons, i.e. the transition from the L-shell to the K-shell is denoted K-Alpha peak, the one from the M-shell to the K-shell as K-Beta, etc. In order to study the homogeneity of our crystal, the EDX measurements were typically performed on several regions of the sample surface. We typically probed five to six points and found no significant variation in the stoichiometry of our samples. This technique also allows one to search for possible minority phases which can be incorporated within the regions of growth defects or simply embedded in the volume of the crystal. We did not obtain any evidence for the presence of such minority phases.

All our crystals have been investigated with this EDX technique. Based on these EDX results are the Zn, Ni and Ca concentrations that are quoted in this

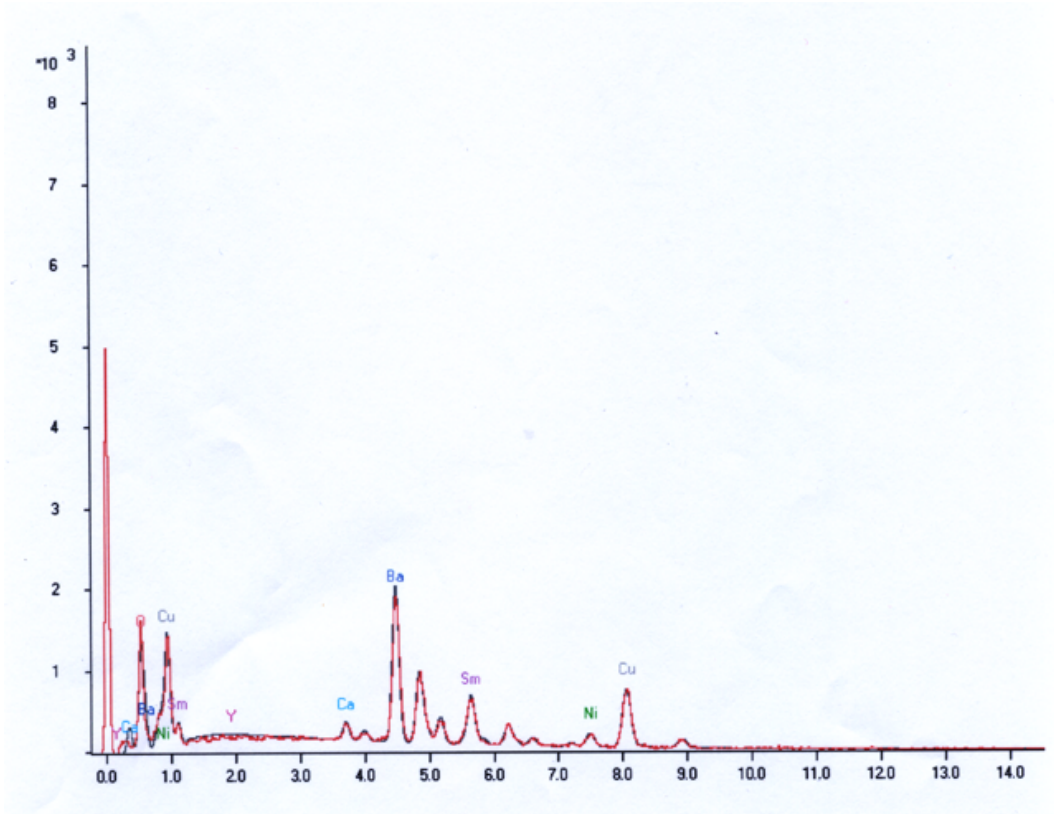


Figure 5.3: EDX spectrum of an overdoped  $(Sm, Y, Ca)Ba_2(Cu, Ni)_3O_7$  sample thesis.

### 5.3 Thermoelectric power measurements

The thermoelectric power coefficient  $S$  is determined by the voltage  $dV$  which appears when a temperature gradient  $dT$  is applied to a sample:

$$dV = SdT. \quad (5.1)$$

Generally, this coefficient is temperature dependent, and it is assumed that the temperature gradient is small enough to use the theory of linear response. In theory, the thermoelectric power coefficient depends on the energy derivative of the mean free path of the carriers, and their charge, concentration and mobility[92]. For example, from the sign of the thermoelectric power coefficient one can usually determine the type of charge carriers, i.e. whether they are electrons or holes.

The thermoelectric power coefficient are typically measured by attaching a

small heater to one side of the sample plus an electrical circuit to measure the voltage between the two sides. The voltage is measured after a small heat pulse is applied to one side of the sample. In principle, it is possible to measure the temperature dependence of the thermoelectric power coefficient, and to combine this measurement with resistivity measurements. Details of the experimental technique are described in [93].

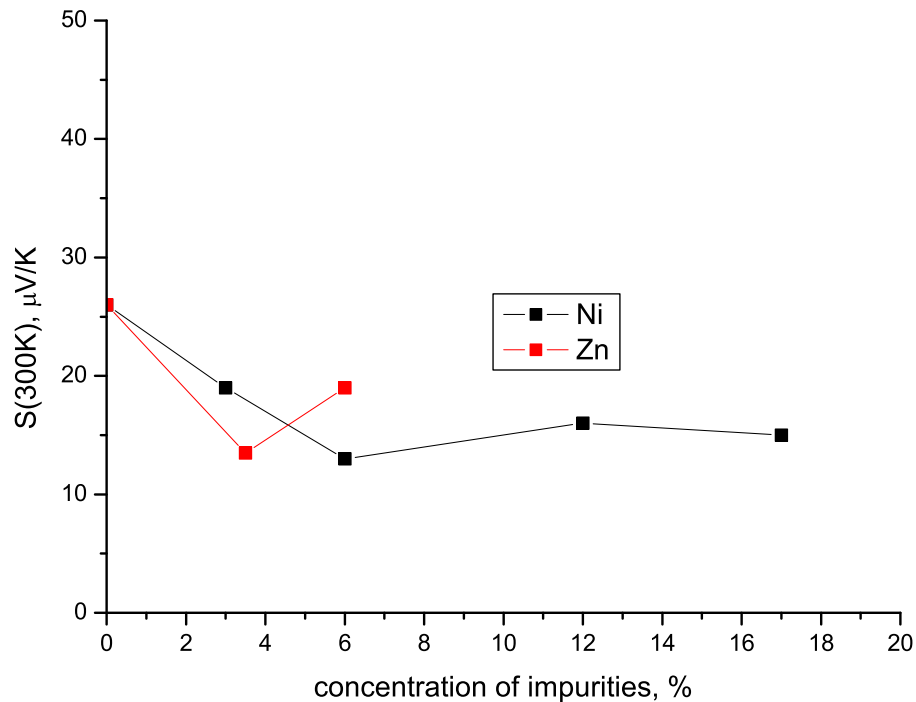


Figure 5.4: Thermoelectric power coefficient versus Zn, Ni content for  $NdBa_2Cu_{3-x}(Zn, Ni)_xO_{7-\delta}$  samples.

In case of the cuprate HTSC it has been established empirically that the thermoelectric power coefficient allows for a rather accurate and reproducible estimate of the hole concentration [95]. A common scaling relationship has been established for various compounds of the cuprate HTSC. Concerning our samples, which are hole doped high temperature superconductors with Zn and Ni impurities, the dependence of thermoelectric power coefficient on the impurity concentration contains information about the changes of hole concentration with impurity content. Based on our thermoelectric power measurements we could confirm that the Zn and Ni impurities do not significantly change the hole concentration of our samples.

The thermoelectric power coefficients of our series of underdoped Ni and Zn



substituted Nd123 crystals are shown in fig. 5.4. The small variation in the room TEP coefficient translates into a corresponding variation of the hole doping state of about 0.01. So,  $26 \mu V/K$  corresponds to hole content 0.0995, and  $12 \mu V/K$  corresponds to hole 0.112 [125]. The TEP data thus put a rather small upper limit on the possible variation of the hole concentration upon Ni and Zn impurity substitution.

## 5.4 $\mu SR$ measurements

### 5.4.1 Introduction to $\mu SR$

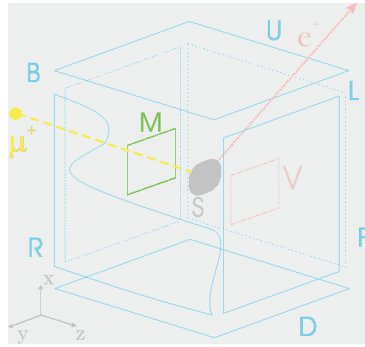


Figure 5.5: Scheme of a typical time differential  $\mu SR$  experiment [96].

The technique of  $\mu SR$  is especially well suited to investigate weak and short range magnetic correlations and to determine their volume fractions. Similar like the nuclear magnetic resonance technique, in muon spin rotation experiments one determines the distribution and the dynamics of the local magnetic fields at the muon sites. The main difference lies in the production of a spin-polarized state and in its detection. Muons are short lived particles (lifetime of about 2.2 microseconds, spin 1/2 and charge  $+e$  for positive muons) that are produced at a proton accelerator. Under appropriate conditions a beam of fully spin-polarized muons can be produced with their spin antiparallel to their momentum. The muons can be stopped inside a sample without any significant loss in their initial spin polarization. They are situated at particular lattice sites within a unit-cell but are randomly distributed throughout a range of several hundred micrometers thus sampling a representative part of the sample volume. Just like in an NMR experiments the muons experience the local magnetic field from the host lattice and thus exhibit a spin-precession. The detection of the final spin state makes use of the decay of the muons which is mediated by the weak interaction that violates parity. The decay products, i.e. a positron, electronic neutrino and a

muon antineutrino, are thus emitted in preferential directions as determined by the muon spin direction at the instant of decay. In the  $\mu SR$  experiment only the emission of the positions is detected with scintillator detectors that are arranged in pairs located at 180 degree with respect to each other. This allows one to monitor the asymmetry of the position emission rate in a time dependent mode. The measured time dependence of this asymmetry can be directly translated into the time dependence of the ensemble of muons (see fig. 5.5).

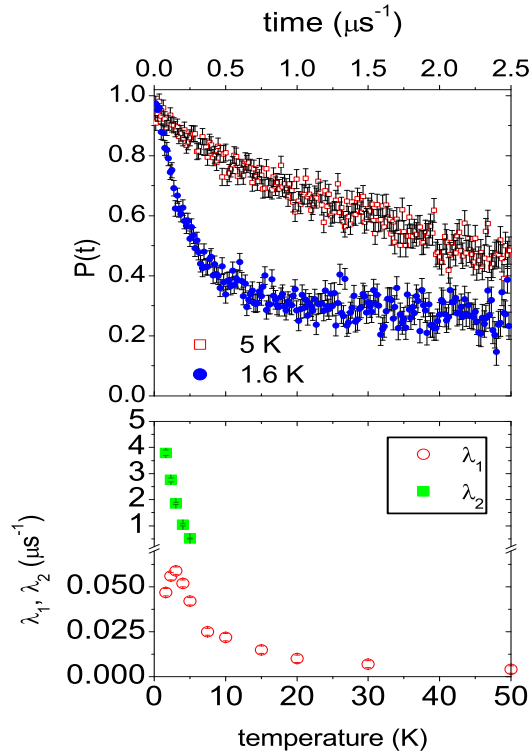


Figure 5.6: ZF spectra of slightly overdoped  $Eu_{0.85}Ca_{0.15}Ba_2Cu_{2.86}Ni_{0.24}O_{6.8}$ . Fig. (a) shows spectra above and below 3K, fig. (b) shows the evolution of the transverse and longitudinal relaxation rates.

A clear signature that the different muons experience a well defined local magnetic field. The signature of strongly disordered static local magnetic fields is a rapid depolarization of the muon spin polarization function. The signature of the formation of such a strongly disordered magnetic state is indeed evident from our ZF  $\mu SR$  experiments on the Ni-substituted samples as shown in the next paragraph.

The specific form of the muon polarization function  $P(t)$  depends on the magnetic properties of the sample. If we consider only a single muon site in a polycrystalline sample and a so-called zero-field (ZF) condition without an external field, then the powder average yields that 1/3 of the amplitude of the muon spin polarization function remains constant whereas 2/3 of the amplitude exhibit a time dependence that reflects the internal field distribution. An oscillatory behavior of this 2/3 component will be a clear signature that the different muons experience a well defined local magnetic field. The signature of strongly disordered static local magnetic fields is a rapid depolarization of the muon spin polarization function.

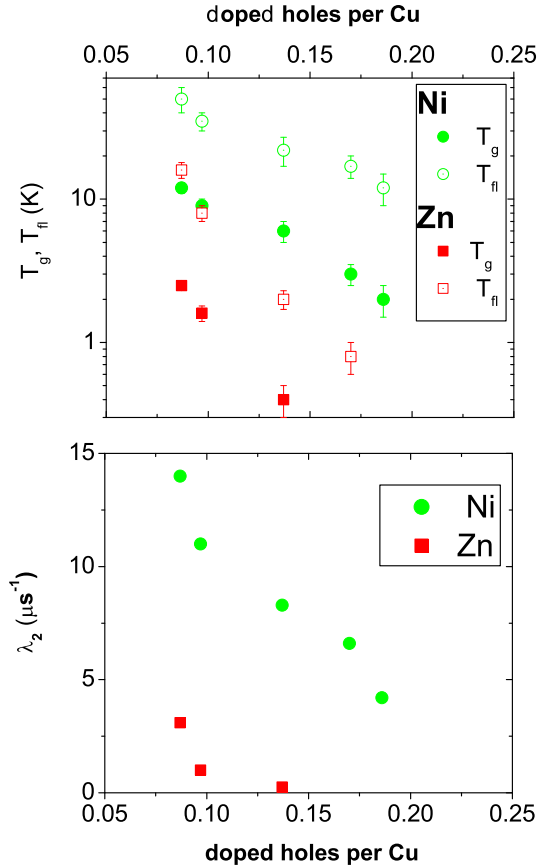
5.4.2  $\mu SR$  measurements on  $Eu_{0.85}Ca_{0.15}Ba_2Cu_{3-y}(Zn, Ni)_yO_{7-\delta}$ 


Figure 5.7: (a) Doping dependence of the spin freezing temperature  $T_g$  and the temperature below which spin fluctuations appear in the  $\mu SR$  time window  $T_{fl}$ ; (b) doping dependence of the transverse relaxation rate for  $Eu_{0.85}Ca_{0.15}Ba_2Cu_{2.86}(Ni, Zn)_{0.24}O_{6.8}$

Heavily Zn, and Ni substituted poly-crystalline  $EuCa(Zn, Ni)_{123}$  samples have been measured by  $\mu SR$ . The ZF spectra for a slightly overdoped Ni doped sample are shown in fig. 5.6. From the rapid onset of a strong depolarization one can deduce that a spin-glass transition is taking place in this sample around 3K. The spectrum at 5 K exhibits a moderate relaxation which is characteristic of the local magnetic fields that arise from the nuclear spins of Cu. The much more rapid depolarization as shown at 1.6K is caused by the strongly disordered magnetic field due to electronic magnetic moments. The circumstance that the related asymmetry accounts for the entire sample volume suggests that these electronic moments must exist even in the regions that are far away from the magnetic Ni impurities. The present  $\mu SR$  data therefore suggests that the Ni impurities induce a spin-polarization that persists through the entire sample volume.

The related spin-freezing transition and its evolution as a function of doping is summarized in Fig. 5.7. It is clearly seen that this spin-freezing transition temperature is strongly enhanced upon Ni substitution whereas it is much lower in the Zn substituted samples. Note that a similar spin-freezing transition of the electronic Cu moments has previously been observed in the pure samples but only

in the strongly underdoped regime of the phase diagram Ref. [126]. Our present  $\mu SR$  data suggest that the Ni impurities largely enhance the tendency for this spin-freezing transition thereby extending the related spin glass regime even into the overdoped regime (see fig. 5.7. This effect is clearly absent for the case of the non-magnetic Zn-impurities.

## 5.5 Pure samples

### 5.5.1 Identification of pseudogap in c-axis optical conductivity

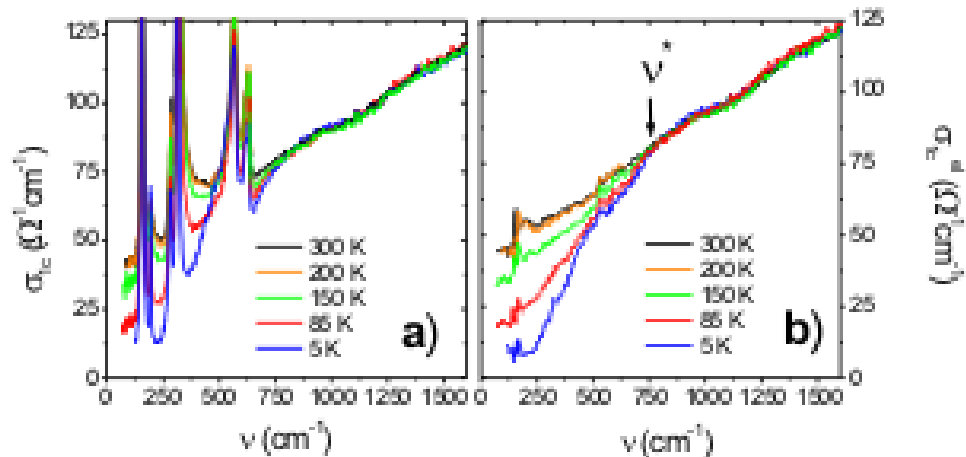


Figure 5.8: Pseudogap in underdoped  $YBa_2Cu_3O_{6.8}$

In conventional superconductors the optical conductivity becomes zero below the frequency  $2\Delta$  at  $T = 0K$  as given by the superconductive energy gap. The typical behavior of the optical conductivity was discussed already in chapter 2, 2.21 on page 81 in the context of the discussion of the optical sum rule. The theory of the optical conductivity in BCS superconductors is given in [109]. Physically, zero conductivity below twice the gap energy means that the material is a perfect reflector that does not absorb photons with energy less than  $2\Delta$ , because all the carriers are condensed in Cooper pairs with binding energy  $2\Delta$ . An energy higher than  $2\Delta$  is required to break up the Cooper pairs.

Figure 5.8 shows representative c axis spectra of the Y123 HTSC  $YBa_2Cu_3O_{6.8}$  with  $T_c$  about 80 K. Apart from the narrow peaks which correspond to infrared active phonon modes, the broad electronic background exhibits characteristic spectral changes that set in already in the normal state well above  $T_c$ . A partial gap-like suppression of the c-axis conductivity with decreasing temperature gradually sets in below a characteristic frequency of about  $850\text{cm}^{-1}$ , which is denoted as the pseudogap frequency  $\omega_{pg}$ . This decrease first occurs around 150 K, i.e. well above  $T_c = 80\text{K}$ . A similar behavior has been observed for many HTSC compounds. It was found that the partial suppression of conductivity starts from  $T^*$ , which is the pseudogap temperature.

Similar results were previously obtained based on normal-incidence reflectivity measurements [101]. Furthermore, the doping dependence of the temperature and energy scales of this feature is similar to the one observed for the pseudogap by other technique like STM or ARPES (see Chapter 3 for details). Therefore, this feature was termed as c-axis pseudogap and it is commonly assumed that it corresponds to the same PG as probed by STM and ARPES. However, the opposite point of view has also been expressed by some authors claiming that c-axis pseudogap as measured by optical conductivity has a different origin than the pseudogap observed by photoemission [41]. The predictions of these models in terms of the sensitivity of the pseudogap to the particular properties of the spacing layers separating the  $\text{CuO}_2$  planes have been contradicted by the measurements showing that the c-axis PG systematically depends on the hole doping state of the  $\text{CuO}_2$  planes while it hardly depends on the number of defects or the dielectric properties of the spacing layers. For this reasons, in the following we assume that the pseudogap in the optical c-axis conductivity is of the same origin as the one observed by the other techniques.

In contrast with the superconductive gap in conventional superconductors, the pseudogap is not a real gap in a sense that the optical conductivity goes to zero at  $T = 0\text{K}$  below  $2\Delta$ . The c axis conductivity of high temperature superconductors remains non-zero at all frequencies below  $\omega_{pg}$  even at the lowest experimentally available temperatures of about  $4\text{K}$  (see fig 2.7 on the page 69). For this reason this gap was called "pseudo". Non-zero optical conductivity is a sign of anisotropy of an order parameter in k-space, or an indication of the presence of some unpaired carriers at low temperature. Concerning the SC gap it is meanwhile well established that the d-wave symmetry of the order parameter

and the subsequent gap nodes are a reason for the finite conductivity within the energy gap region. Concerning the pseudogap phase very little is known at the present stage.

### 5.5.2 Effect of substitution on the rare earth site: differences between Y123 and Nd123

As it was discussed in introduction, one can not incorporate larger amounts of Zn and Ni impurities in the 123 type compounds when Y is replaced by a larger rare earth like Nd or Sm. For this reason we have studied  $Nd(Ni, Zn)123$  and  $Sm(Ni, Zn)123$  crystals. In the following interpretation of our data we would like to make contact with the results concerning the doping dependence of the spectral gap in the c-axis conductivity which was mainly performed on Y123 type single crystals. Therefore, we first need to consider whether the substitution of Y versus Nd and Sm on the rare earth site of the 123 structure has any significant effect on the pseudogap energy scale.

Figure 5.9 shows spectra of the c-axis conductivity for three kinds of crystals which exhibit a similarly underdoped state. It should be noted that the doping state is similar but not quite identical. Shown are spectra for (a)  $Y_{0.7}Pr_{0.3}Ba_2Cu_3O_7$  with  $T_c = 61K$ , (b)  $YBa_2Cu_3O_{6.6}$  with  $T_c = 65K$ , and (c)  $NdBa_2Cu_3O_{6.8}$  with  $T_c = 65K$ . For each sample the pseudogap onset is indicated by an arrow. Irrespective of the ion on the rare earth site, the pseudogap energy scales obviously are fairly similar for all three samples. The dependence on the hole doping state of the spectral gap in the c-axis conductivity is furthermore illustrated in the figure 5.9. In fig. 5.9, the solid green data points account for data that have been obtained for Y123 while the solid pink and black squares mark data points obtained for Nd123 or Sm123 samples. Blue points correspond to the gap in optimally doped and overdoped state. The doping state was determined here based on the measured  $T_c$  and  $T_{cmax}$ , max values of the compounds or from the measured value of the thermo-electric power.

Based on these data we conclude that the pseudogap is evident in all underdoped RE123 crystals (RE is an rare earth element). The energy scale furthermore, is determined mainly by the hole doping state of the  $CuO_2$  plane. The RE-substitution has hardly a direct effect on the PG energy scale.

Next we consider the IR-active phonons in the spectra of Y123, YPr123,

Sm123, and Nd123. The most obvious changes concern the phonon mode near  $190\text{cm}^{-1}$  which exhibits a clear red-shift for the compounds with heavier rare earth like Nd and Sm. This agrees with the previous assignment of this mode to vibrations of (Y, Nd) ions against Cu in the chains (so-called rare earth mode). The observed shift is well explained by the difference in the masses of Y, Pr, Nd and Sm. Further differences in the oscillator strengths of the modes at 570, 620, 630  $\text{cm}^{-1}$  are related to the different oxygen content which the CuO chains have in these samples. Meanwhile it is well established that the ordering of oxygen vacancies and the subsequent charge transfer from the chains to the  $\text{CuO}_2$  planes is dependent on the kind of ion on the rare earth site. As a result a somewhat higher oxygen content is required in Nd123 than in Y123 in order to achieve the same doping level of the  $\text{CuO}_2$  planes [110]. As discussed in previous chapters, the hole doping state can be affected and manipulated by different cationic substitutions. For instance, the partial substitution of Y by Ca (Pr) will lead to an increase (decrease) of the hole doping state. A corresponding hole doping state as for a Ca(Pr)-free sample thus requires a significantly lower (higher) oxygenation of the CuO chains. Apart from the conditions under which the sample has been annealed, an estimate of this difference in the oxygen content of the CuO chains can be obtained directly from the c-axis optical spectra in terms of the relative spectral weight of the modes at 570 to the ones at 620 and 630  $\text{cm}^{-1}$ . The so-called apical mode at 570  $\text{cm}^{-1}$  corresponds to the vibration of apical oxygen with respect to Cu(1) in the chains with two neighboring oxygen ions. The ones at 620 and 630  $\text{cm}^{-1}$  are the corresponding apical modes where one or two oxygen ions in the neighborhood of the Cu(1) are missing.

Another interesting difference is apparent in the superconductive state, where the position of the so-called transverse Josephson plasma mode clearly varies between the different RE123 compounds, i.e. it is shifted to lower frequency in case of the large RE ions like Nd and Sm. This difference can be well accounted for in terms of the Josephson super-lattice model that was introduced in a previous chapter and discussed in detail in the context of our data on the Bi2223 compound. Within this theory the position of the transverse mode depends on the Josephson-plasma frequency of the intra-bilayer region which is exponentially related to the bilayer spacing. The main effect thus can be explained in terms of the larger ionic radius of the  $\text{Nd}^{3+}$  and  $\text{Sm}^{3+}$  ions.

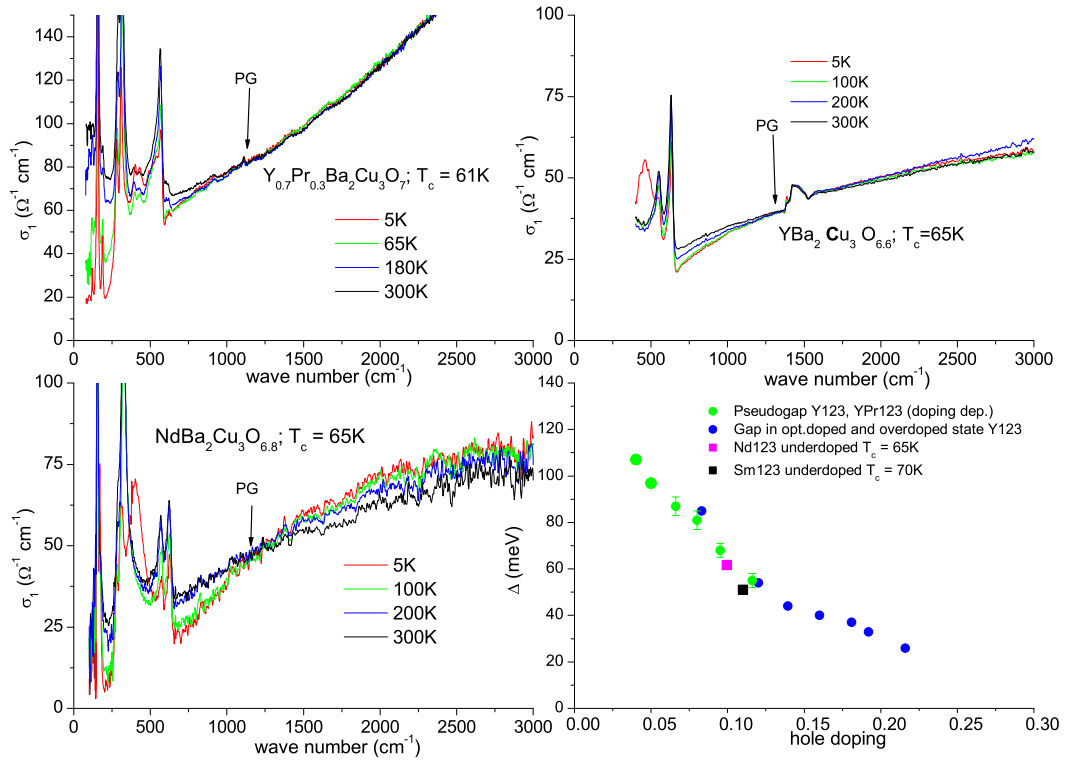


Figure 5.9: Pseudogap in three underdoped samples: on top is  $Y_{0.7}Pr_{0.3}Ba_2Cu_3O_7$  ( $T_c = 61K$ ), in the middle is  $NdBa_2Cu_3O_{6.8}$  with ( $T_c = 65K$ ), and on bottom is  $YBa_2Cu_3O_{6.6}$  with ( $T_c = 65K$ ). Hole contents in YPr123 and Nd123 samples a close to each other. Sm123 has higher hole content. The graph in right lower corner shows doping dependence of the pseudogap in Y123 sample. The points corresponding to our Nd123 and Sm123 sample.



## 5.6 Pseudogap in Ni doped $(Sm, Nd)Ba_2Cu_{3-y}Ni_yO_{7-\delta}$ samples

### 5.6.1 Introduction

This section presents our ellipsometry data as obtained on the series of underdoped  $NdBa_2Cu_{3-x}Ni_xO_{6.8}$  single crystals. The Ni content was varied over a very wide range from 0 to 17%. The most important result concerns the doping dependence of the pseudogap energy scale as deduced from our c-axis optical spectra which increases very strongly with the Ni-content. At the same time the in-plane conductivity remains metallic even for the sample with the highest Ni concentration of 17%. In the following we also present the doping dependence of the pseudogap energy scale as observed for heavily Ni substituted crystals where superconductivity is fully suppressed at all doping levels.

### 5.6.2 Dependence of pseudogap frequency on Ni content

Ellipsometry results on the series of underdoped Ni substituted samples are presented in fig 5.10. Spectra of pure, 6%, and 12% Ni samples are shown. The dependence of  $T_c$  and pseudogap frequency on the Ni content is plotted in the bottom right corner in fig 5.10. It contains two additional points corresponding to 3% and 17% Ni. As was previously shown by SQUID, about 4% Ni is sufficient to suppress superconductivity completely. Accordingly, already the sample with 6% Ni impurities is not superconductive anymore.

The samples were simultaneously annealed together in the same furnaces to ensure that they have the same oxygen content. The thermoelectric power measurements as presented above on page 127 furthermore reveal that the hole doping state of the  $CuO_2$  planes does not exhibit a sizeable variation as a function Ni content.

The observed dramatic increase in the pseudogap frequency scale  $\omega_{pg}$  can thus not be ascribed to a Ni induced change in the hole content which according to Fig. 5.13. would need to be extremely large. In the pure sample  $\omega_{pg}$  is about  $1250cm^{-1}$ , while in the sample with 12% Ni  $\omega_{pg}$  it is already about  $2000cm^{-1}$ . This huge Ni impurity induced increase of the pseudogap energy scale is a very interesting result that has not been anticipated. It represents one of the major

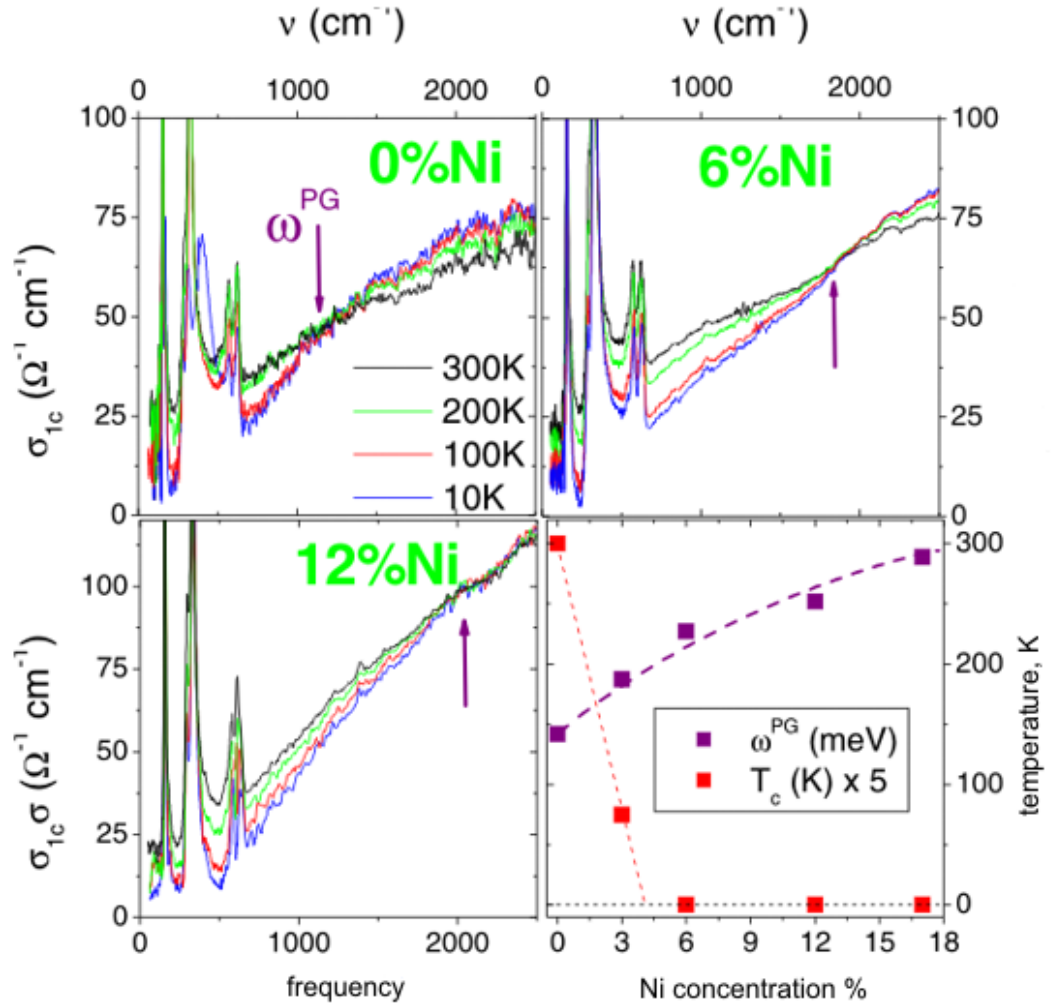


Figure 5.10: C-axis optical conductivity spectra of three under-doped  $NdBa_2Cu_{3-x}Ni_xO_{6.8}$  single crystals with 0, 6, and 12% Ni content. The bottom right panel presents the dependence of the PG energy and  $T_c$  on the Ni concentration.

achievements of the present thesis work. The ability of the magnetic Ni impurities to enhance the pseudogap contradicts with many existing theories of the pseudogap phenomenon. Most obviously, it challenges the theory interpreting the pseudogap in terms of precursor superconductive fluctuations. As Ni impurities apparently fully suppress superconductivity, within this theory accordingly they should tend to reduce the energy scale of the order parameter and thus of the spectral gap. Certainly, it is not be expected that the gap energy scale is doubled while superconductivity is fully suppressed.

### 5.6.3 In-plane conductivity of Ni-doped samples

The present study was focused on the evolution of the c-axis conductivity where the signature of the pseudogap is strongest. This is related to the k-space anisotropy of the c-axis hopping parameter which is large at the so-called hot-spot regions near the X-point of the Brillouin-zone where the signature of the correlations underlying the PG are strongest. The signature of the pseudogap effect can also be seen in the in-plane response where it is superimposed, however, by a much larger contribution due to the quasi-particle in the vicinity of the so-called cold-spots near the diagonal of the BZ [42, 10]. For the sample with the highest Ni content of 17% we have also performed corresponding measurements of the in-plane response. The real parts of the in-plane conductivity  $\sigma_1$  and the dielectric function  $\varepsilon_1$  are shown in fig. 5.11. Apparently, the in-plane response in this most highly Ni substituted sample maintains a metallic frequency and temperature dependence. By metallic we mean that the conductivity remains quite high, and the dielectric function becomes negative towards low frequency. In agreement with previous reports, we observe a significant broadening of the Drude-like response which we attribute to a corresponding increase of the scattering rate of the quasi-particles in the cold-spot regions of the BZ. In clear contrast to the c-axis spectra there is no direct evidence for the formation of an energy gap. This confirms our point of view that the pseudogap is limited to the so-called hot-spots in agreement with the direct observation by ARPES measurements on pure crystals. It also supports our point of view that the Ni-enhanced or induced PG in the c-axis conductivity spectra is not related to the development of an overall insulating electronic state in these heavily Ni-impurities substituted and thus disordered crystals.

### 5.6.4 Pseudogap in optimally doped and overdoped Ni substituted samples

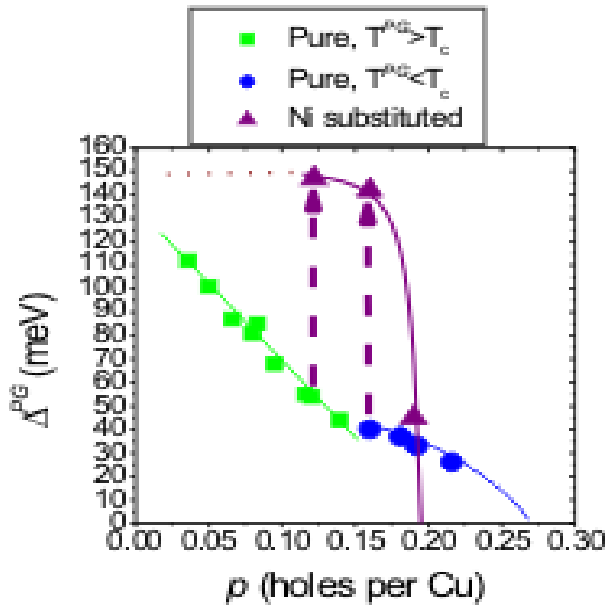


Figure 5.13: Pseudogap on the phase diagram for pure crystals and for Ni doped crystals

Next consider how the PG in heavily Ni substituted crystals evolves as a function of hole doping in the optimally doped and over-doped regions. As was shown in chapter two, the conductivity does not exhibit the pseudogap effect for the case of pure samples in the optimally doped and overdoped regimes. Note that in the pure samples there is no evidence for a pseudogap in optimally doped and overdoped samples. It is always observed that the spectral gap forms here right below the superconductive transition temperature  $T_c$  [10]. The normal state conductivity spectra are nearly featureless and temperature independent in optimally doped samples while they gradually acquire a metallic like frequency and temperature dependence towards the overdoped side of the phase diagram. The spectra of the optimally doped  $SmBa_2Cu_{2.86}Ni_{0.14}O_7$  and the over doped  $Sm_{0.86}Ca_{0.14}Ba_2Cu_{2.88}Ni_{0.12}O_7$  are plotted in figure 5.12. The optimally doped sample is non-superconductive, the overdoped one has a  $T_c$  of 25K. It is evident from this figure that a sizeable pseudogap is induced upon Ni-substitution in the optimally doped sample. Note that this sample is not superconductive and that it would not exhibit a pseudogap if it did not contain the Ni impurities. This Ni-induced restoration of the PG in the c-axis optical response of this optimally doped sample is a clear manifestation that the pseudogap and the superconductive gap must have different origins. In fact, for the present sample the suppression of the electronic conductivity is almost complete below  $300\text{ cm}^{-1}$ , the gap restored by the Ni-impurities thus has the signatures of a real gap rather than of a spatially inhomogeneous feature which thus remains incomplete.

Next consider how the PG in heavily Ni substituted crystals evolves as a function of hole doping in the optimally doped and over-doped regions. As was shown in chapter two, the conductivity does not exhibit the pseudogap effect for the case of pure samples in the optimally doped and overdoped regimes. Note that in the pure samples there is no evidence for a pseudogap in optimally doped and overdoped samples. It is always observed that the spectral gap forms here right below the superconductive transition temperature  $T_c$  [10]. The normal state conductivity spectra are nearly featureless and temperature independent in optimally doped samples while they gradually acquire a metallic like frequency and temperature dependence towards the overdoped side of the phase diagram. The spectra of the optimally doped  $SmBa_2Cu_{2.86}Ni_{0.14}O_7$  and the over doped  $Sm_{0.86}Ca_{0.14}Ba_2Cu_{2.88}Ni_{0.12}O_7$  are plotted in figure 5.12. The optimally doped sample is non-superconductive, the overdoped one has a  $T_c$  of 25K. It is evident from this figure that a sizeable pseudogap is induced upon Ni-substitution in the optimally doped sample. Note that this sample is not superconductive and that it would not exhibit a pseudogap if it did not contain the Ni impurities. This Ni-induced restoration of the PG in the c-axis optical response of this optimally doped sample is a clear manifestation that the pseudogap and the superconductive gap must have different origins. In fact, for the present sample the suppression of the electronic conductivity is almost complete below  $300\text{ cm}^{-1}$ , the gap restored by the Ni-impurities thus has the signatures of a real gap rather than of a spatially inhomogeneous feature which thus remains incomplete.

A really drastic change is apparent for the overdoped sample where despite the high Ni concentration there is only a faint signature of a spectral gap. Furthermore, the gap energy as indicated by the solid arrow in fig. 5.12 is strongly reduced from more than  $2000 \text{ cm}^{-1}$  for the optimally doped sample to about  $750 \text{ cm}^{-1}$ . This highlights a second important result concerning the doping dependence of the Ni-induced or enhanced PG which is summarized in Fig. 5.12. which shows the doping dependence of the spectral gaps in pure and in heavily Ni substituted samples. The green points and line correspond to the pseudogap in pure under-doped samples whereas the blue symbols give the spectral gap which develops right below  $T_c$  in pure optimally doped and over-doped samples. The purple symbols indicate the maximum value of the pseudogap as observed in heavily Ni substituted samples. The doping state has been deduced for the Ni-substituted samples from the measured TEP at room temperature. Evidently, the Ni-induced PG has a very large energy scale for underdoped and optimally doped samples while it falls off very steeply shortly past optimum doping towards the overdoped side. In contrast the spectral gap in the pure and thus superconductive samples persists to a significantly higher doping level. The Ni-enhanced PG disappears rather sharply towards a doping state of about 0.2. Interestingly, anomalously rapid changes of the normal state and SC properties of pure samples have been reported to occur around this doping state. This behavior is suggestive of a phase transition around this critical doping point. Extensive evidence in favor of such a critical point in the phase diagram situated slightly on the overdoped side has been summarized in Ref. [129]. In pure samples, the drastic changes of the ground state properties cannot be accessed since they are superimposed by the response of the SC phase which forms at elevated temperatures. In our Ni-substituted samples however where SC is absent, this transition becomes evident from the sudden onset of the energy gap in the  $c$ -axis conductivity. Clearly, our results should motivate further investigations of heavily Ni-impurity substituted samples by means of other spectroscopic techniques which can provide more direct information on the  $k$ -space and real-space variation of their electronic and magnetic properties.

## 5.7 IR spectra of Zn substituted samples for different hole doping

The drastic enhancement of the PG upon Ni impurity substitution as described in the previous section raises the question whether this phenomenon is related to the potential scattering or rather due to the magnetic properties of the Ni impurities with a magnetic moment of  $S = 1$ . In order to address this important issue we have performed corresponding ellipsometric measurements on Zn substituted  $(Nd, Sm)Ba_2Cu_{3-y}Zn_yO_{7-d}$  single crystals. The  $Zn^{2+}$  ions themselves are non-magnetic impurities ( $S = 0$ ). Their most prominent effect is the strong potential scattering in the unitary limit (large phase shift upon scattering). Nevertheless, the Zn impurities also affect the magnetic correlations of the host  $CuO_2$  planes. At low concentrations they even induce static local moments on the nearest and next nearest neighbor Cu sites. However, this effect apparently is limited to low Zn content. It is maximum around 2% of Zn impurities, falls off very rapidly towards higher Zn content and finally is fully absent for Zn concentrations in excess of 5% [127].

In short, both Ni and Zn impurities when incorporated within the  $CuO_2$  planes give rise to strong potential scattering. The non-magnetic Zn impurities locally restore static magnetic correlations of the neighboring Cu moments at very low concentrations [82] while at concentration higher than 2% they strongly suppress AF correlations of the host  $CuO_2$  planes [127]. To the contrary, the magnetic Ni-impurities tend to restore magnetic correlations of the host  $CuO_2$  planes.

This was demonstrated in the section 5.4.1 where we discussed the  $\mu SR$  measurements which establish that the Ni impurities enhance the low-energy spin-correlations. The spin-freezing temperature as seen by  $\mu SR$  is found to increase continuously as function of Ni substitution with no sign of saturation up to the highest available concentrations.

In the following we present our ellipsometric data of the c-axis conductivity of the Zn substituted samples which highlight that the non-magnetic Zn impurities have an entirely different impact on the optical pseudogap than the magnetic Ni impurities. Figure 5.14 shows the conductivity spectra as a function of temperature for underdoped  $(NdSm)Ba_2Cu_{3-y}Zn_yO_{6.8}$  crystals with Zn concentrations of 0, 1, 6 and 9%. This series of samples was prepared under identical conditions as the underdoped Ni-substituted series. In fact, the data on the pure

sample with  $T_c=65\text{K}$  are the same as for the Ni series in Fig. 5.10. The sample with 1% Zn has a  $T_c$  of 20 K whereas the samples with 6 and 9% are entirely non-superconductive.

The most important result that is very obvious from Fig. 5.14 is that the non-magnetic Zn impurities do not lead to a similar strong enhancement of the pseudogap energy scale as it was observed in the case of the magnetic Ni impurities. To the contrary, the Zn impurities rather tend to fill in the pseudogap while they slightly reduce its characteristic energy scale. Only at the comparably small Zn concentration of 1% it appears that a slight increase of the pseudogap energy scale may occur. The onset frequency of the gap like suppression of the optical conductivity indeed increases from about  $1250\text{ cm}^{-1}$  in the pure sample to nearly  $1300\text{ cm}^{-1}$  at 1% of Zn content before it decreases again at higher Zn content to about  $1100\text{ cm}^{-1}$  at 9% of Zn impurities. The second important feature induced by the Zn impurities is the apparent filling in of the pseudogap. The gap like suppression of the conductivity becomes very weak especially at the highest Zn content of 9% where the signatures of the pseudogap become very faint.

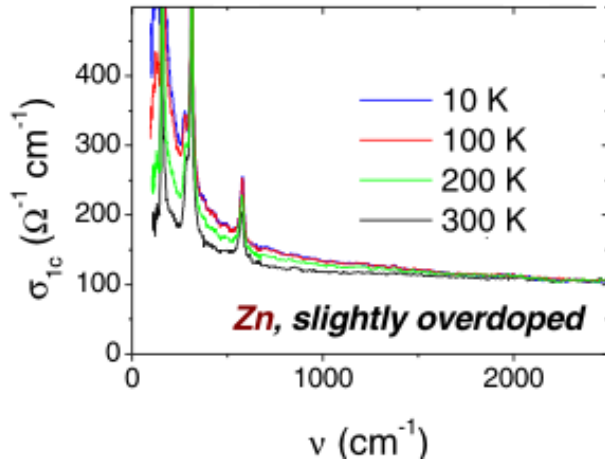


Figure 5.15: Infrared c-axis conductivity spectra of slightly overdoped  $Sm_{1-x}Ca_xBa_2Cu_{3-y}Zn_yO_{7-\delta}$  with 8.5% Zn

The above described observations concerning the behavior of the pseudogap upon Zn substitution are consistent with the previously expressed point of view that the Zn impurities have a rather local effect, i.e. only the regions in the vicinity of the Zn impurity are affected. This effect was previously seen by NMR and especially by means of STM measurements which highlight that the spectral gap becomes locally suppressed in the vicinity of the Zn impurities.

The apparent filling in of the pseudogap that is evident in our spectra can be simply explained within such an inhomogeneous scenario. The growing number of Zn impurities gives rise to an

increasing volume fraction where the optical response is gapless and thus maintains a finite conductivity. It should be noted however, that STM experiments have been performed on samples with comparatively much lower Zn content. Future NMR and STM experiments on samples with similarly high Zn content would be desirable in order to confirm our interpretation. Another interesting feature is the initial moderate increase of the PG energy scale as observed for the small Zn content of about 1% which compares rather well with the previously reported Zn impurity-induced increase of the local AF correlations for  $z < 0.02$ . In agreement with the observed Ni-induced enhancement of the PG energy scale, this observation suggests that the strengthening of the AF correlations of the Cu spins of the host lattice is intimately related to the energy scale of the pseudogap phenomenon. Leaving aside any details, this observation suggests that short range AF spin fluctuations (which may be best described in terms of the tendency for local singlet formation) or are playing a vital role in the correlations that are underlying the pseudogap phenomenon and the related anomalous normal state properties of the underdoped cuprate HTSC.

Next we consider how the Zn-induced changes of the c-axis optical conductivity evolve as a function of hole doping. In clear contrast with the Ni substituted samples, the Zn-impurities do not induce or restore a pseudogap in optimally or slightly overdoped crystals. This is evident in Figure 5.15 which shows the c-axis conductivity of a slightly overdoped SmZn123 sample which highly Zn substituted and thus non-superconductive. Unlike for the correspondingly doped heavily Ni substituted sample in Fig. 5.12, there is no trace of a pseudogap in the c-axis conductivity. To the contrary, the conductivity exhibits a metallic-like increase towards low temperature and frequency. Also the overall value of the c-axis conductivity is considerably higher than in the corresponding Ni substituted sample. Apart from the fact that the present sample is not superconductive and thus does not exhibit any signature of a spectral gap at finite temperature, the c-axis spectra compare rather well to those of a correspondingly overdoped pure crystal as shown in reference [128]



## 5.8 Discussion

### 5.8.1 Discussion and Conclusions

Our ellipsometric spectra of the c-axis conductivity in impurity substituted 123 type cuprate HTSC can be used to discriminate amongst various theoretical models that have been proposed to explain the pseudogap. Our data highlight that magnetic Ni and non-magnetic Zn impurities whereas they both strongly suppress superconductivity, have an entirely different impact on the PG correlations. Magnetic Ni impurities are highly beneficial and strongly enhance the pseudogap energy scale. With Ni substitution one can even restore a pseudogap in optimally and slightly overdoped samples, where it is fully absent for pure samples. To the contrary, the substitution with non-magnetic Zn-impurities is detrimental for the pseudogap correlations, at least at higher Zn content in excess of 3%.

This result raises serious questions about the validity of several of the proposed theoretical models. In the following we provide a more detailed discussion for some of the most prominent models.

### 5.8.2 Precursor superconductive fluctuations and preformed Cooper pairs

This class of theories interprets the pseudogap in terms of a precursor superconductive state which occurs at elevated temperatures where thermally induced phase fluctuations suppress a long-range coherent state. These models are motivated by the observation that the pseudogap exhibits a similar k-space asymmetry as the d-wave type superconductive order parameter below  $T_c$ . The second argument concerns the similar energy scales of the pseudogap and the superconductive gap.

Our new data are in contradiction to this class of theories. Within the theory of a precursor SC state it is difficult to explain the circumstance that the Ni-impurities give rise to a complete suppression of the macroscopically coherent superconductive state while at the same time they dramatically increase the energy scale of the gap. Within a strong coupling scenario one may explain that the suppression of the order parameters is fairly weak such that a sizeable spectral gap survives even in the absence of a macroscopically coherent state [135, 136]. Our results on the non-magnetic Zn impurities would indeed be consistent with

these predictions. The observed two-fold increase of the pseudogap energy scale upon Ni substitution, however, is extremely difficult to explain in the context of these theories. The main difficulty lies in the unconventional d-wave symmetry of the SC order parameter. Strong potential scattering from any kind of magnetic or non magnetic impurity gives rise to a mixing in k-space and thus leads to destructive interference effects for the states that are located in the vicinity of the gap nodes where the order parameter exhibits a sign change. The effect of potential scattering thus necessarily is deleterious in the presence of an order parameter that has an unconventional symmetry in real or in k-space.

### 5.8.3 Exotic Flux-phase or density wave theories

Similar arguments as outlined above in the context of scenario of a precursor SC state apply for other kinds of models which explain the pseudogap in terms of distinct kinds of correlations that are based on an order parameter with an unusual k-space or real space symmetry such as flux phases or an unconventional d-density wave state [132, 133, 134]. The k-state mixing due to potential scattering and subsequent destructive interference effects will also be deleterious. Within these models it is thus to be expected that the substitution with any kind of impurities which act as potential scatterers will lead to a weakening of the pseudogap correlations.

Our experimental data thus seriously contradict several of the most influential models for the pseudogap. On the other hand, the fundamental difference between the effect of non-magnetic Zn and magnetic Ni impurities points towards an important role of short range AF correlations. In the following we thus discuss some of the models which are based on short range AF correlations or spin-singlet formation.

### 5.8.4 Anti-ferromagnetic fluctuations

The fully deoxygenated compounds  $YBa_2Cu_3O_6$ ,  $REBa_2Cu_3O_6$  are anti-ferromagnetic insulators. Upon hole substitution long range AF order is rapidly suppressed, but short range AF order persists to rather high hole content well into the underdoped regime where it coexists with superconductivity [87]. Pronounced AF spin fluctuations were observed even in optimally doped and slightly overdoped

samples by inelastic neutron scattering. Accordingly, it was proposed theoretically that the pseudogap results from anti-ferromagnetic fluctuations[65]. Within this theory, the underdoped regime is described as a fermi-liquid with two kinds of quasi-particles. The so-called hot quasi-particles reside in the flat part of the Fermi-surface near the X-point of the BZ. The hot quasi-particles are strongly coupled to anti-ferromagnetic fluctuations which give rise to the pseudogap phenomenon. The second kind are the so-called cold quasi-particles which reside near the diagonals of the BZ, i.e. in the vicinity of the gap nodes. The quasi-particles are only weakly interacting with the AF fluctuations and thus are well described by a Fermi-liquid theory. With increasing doping the number of hot quasi-particles decreases whereas the number of the cold ones increases, the pseudogap thus eventually disappears upon doping. Within this theory the pseudogap is unrelated to superconductivity. The pseudogap can be related here to the formation of a partial spin-density wave which introduces a gap on parts of the Fermi-surface, i.e. near the hot spots.

Our present results may well be compatible with this kind of theory. The magnetic Ni impurities strengthen the AF correlations and thus increase the relevant energy scale as well as increasing the number of hot quasi-particles. This may explain that the pseudogap is seen in optimally doped samples, and is enhanced in underdoped samples.

### 5.8.5 Stripe theory of pseudogap

The stripe scenario is based on the idea that the hole carriers frustrate the AF exchange interaction of the Cu spins. The competition between AF exchange energy, the kinetic energy of the holes and their Coloumb repulsion thus has been proposed to lead to the formation of nearly one-dimensionisal regions that are either hole poor or hole rich, i.e. the so-called stripes. Experimental evidence in favor of such hole poor and hole rich stripes has indeed been observed in some of the HTSC compounds in the underdoped regime. [113, 114, 115]. To be more specific, they were observed in compounds that are hardly superconductive anymore, whereas they have not been identified in the samples with a high critical temperature. It has thus been questioned whether the stripe formation is a common property of the HTSC and if so, whether it is involved in the SC pairing mechanism or rather a competitive instability. More recently, it is mostly assumed that the stripes are strongly fluctuating in real HTSC compounds. The

pseudogap phenomenon in the normal state arises here due to the energy barrier against the motion of the quasi-particles through the hole poor regions. The upper limit for the energy scale of the pseudogap is thus given by the AF exchange coupling energy. The stripe fluctuations will decrease the PG energy scale. However, no systematic correlations between the observation of stripes and either the characteristic pseudogap temperature,  $T^*$ , or the pseudogap energy,  $2\Delta$ , have been found. Furthermore, the stripes produce the angular dependence which is different from that of the pseudogap as seen using ARPES [116]. Therefore, there are arguments against an interpretation of the pseudogap in terms of stripes.

On the other hand, it is well possible that magnetic and non-magnetic impurities can have an entirely different impact on the stripes and, in particular, on their fluctuation rate. Magnetic Ni-impurities will not disturb the AF correlations whereas they may tend to slow down the charge carrier dynamics and thus the also the stripe fluctuations. This would restore the PG energy towards the upper limit as given by the exchange coupling energy. To the contrary, non-magnetic Zn impurities will break up the AF network and thus eventually will lead to break-down of the stripe scenario. Only at low concentrations they may act as pinning centers for stripes and thus lead to an initial increase of the PG energy scale.

### 5.8.6 Spin charge separation scenario

In this theory the spin and charge degrees of the quasi-particles are decoupled into spinons with no charge and holons with no spin. Superconductivity requires here the condensation of both holons and the formation of spin-singlets by the spinons. The resulting phase diagram is characterized by a spin singlet phase whose transition temperature decreases with doping, and a holon condensate whose transition temperature exhibits a corresponding increase. Optimum doping corresponds to the point where both transition temperatures coincide. Within this theory the pseudogap phase corresponds to the range where the spin-singlet state is formed, while the holons are not yet condensed. The pseudogap energy is equivalent to the energy that is required to break up the spin singlet pairs. From an experimental and also from a theoretical point of view this theory is far from being established in the quasi-2d cuprate HTSC. In particular, this theory has difficulties in explaining that the pseudogap effect is observed in the charge channel as well as in the spin channel [119]. In the context of this theory it is not

obvious what the role of magnetic and non-magnetic impurities should be. We hope that our work may stimulate future theoretical work along this line.

### 5.8.7 Quantum critical point scenario

Apart from the question of identifying a theoretical model for the pseudogap phenomenon, it is also an utmost important question whether the pseudogap state is related to a real phase transition or whether it is merely a crossover phenomenon related to disorder or strong fluctuations of some kind. Based on the former assumption it has been proposed that a quantum critical point exists in the hole doping phase diagram such that the phase transition occurs at lower doping whereas it is absent at higher doping. Such a quantum critical point has not been unambiguously identified so far. One possible reason is that it is obscured by the superconductive state which coexists on both the underdoped and the overdoped sides. In this context our new data provide new insight since they were performed on samples where superconductivity is fully absent. In particular the phase diagram for the evolution of the pseudogap energy scale as a function of doping for the highly Ni impurity substituted samples provide evidence in favor of such a scenario (fig. 5.13). In particular, the step drop of the pseudogap energy scale around  $p=0.2$ , i.e. well within the region where pure samples remain superconductive, agrees very well with the predictions of the theory of a quantum critical point.

### 5.8.8 Ideas for future projects

First of all, corresponding ARPES experiments on highly Ni substituted would be required to obtain further information on the symmetry of the gap. It could also verify that the Ni induced enhancement of the pseudogap is the property of the in-plane charge dynamics and not an exclusive feature of the c-axis dynamics that is specific to the spacing layer properties. Further ellipsometric measurements of the in-plane response by means of ellipsometry could also be performed and analyzed in terms of the optical scattering rate to obtain further information on the pseudogap behavior that must be unrelated to the properties of the spacing layers.

It is also interesting to investigate the effect of other kinds of magnetic impurities like Fe, Co. Some of these magnetic impurities exclusively occupy the Cu

chain sites and thus do not affect  $T_c$  significantly. It would be interesting to see what happens to the pseudogap in samples with this sort of impurities.

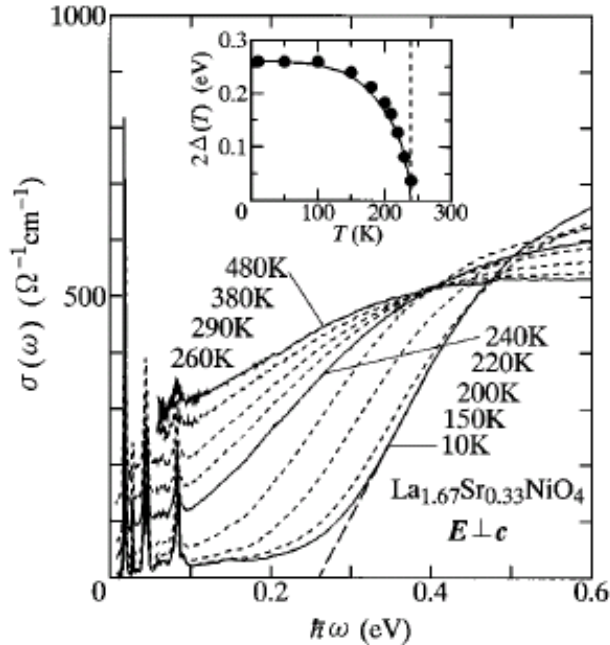


Figure 5.16: Conductivity spectra of  $La_{1.67}Sr_{0.33}NiO_4$  in the  $ab$  plane [52]. Inset shows the temperature dependence of the gap energy

the linear extrapolation of conductivity as it is shown in the figure. The temperature dependence of this crossing point is shown on the insert. The reason of this gap in LSNO is the charge ordering within the stripes as it was observed by electron diffraction measurements[53]. In our NdNi123 samples no direct evidence for charge ordering has been observed. It would thus be very interesting to study how the spectral gap and the evidence for charge ordering evolve as Cu becomes partially substituted into the LS(C,N)O system.

Another interesting question concerns samples with even higher Ni content above 17%. Unfortunately, it is so far not possible to incorporate more Ni into the RE123 structure. This situation can be circumvented by using other compounds like LSCO and LSNO. The first one is a high temperature cuprate superconductor while the second one is a non-superconductive insulator that exhibits anti-ferromagnetic order. The  $ab$  plane conductivity spectra of LSNO are shown in fig. 5.16. It is insulating and exhibits a spectral gap even for the in-plane response. The gap energy is about 0.4eV as determined from the crossing point of the x axis and

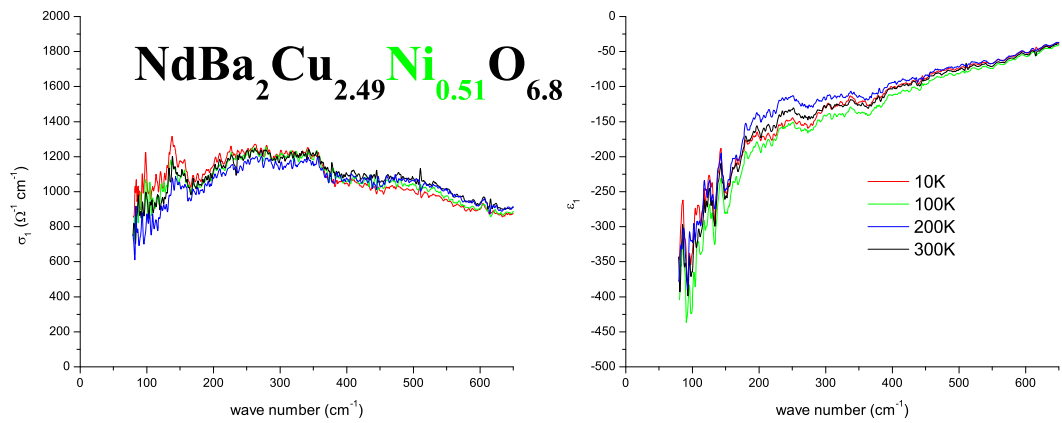


Figure 5.11: ab plane conductivity and dielectric function of underdoped NdNi123 sample with 17%Ni.

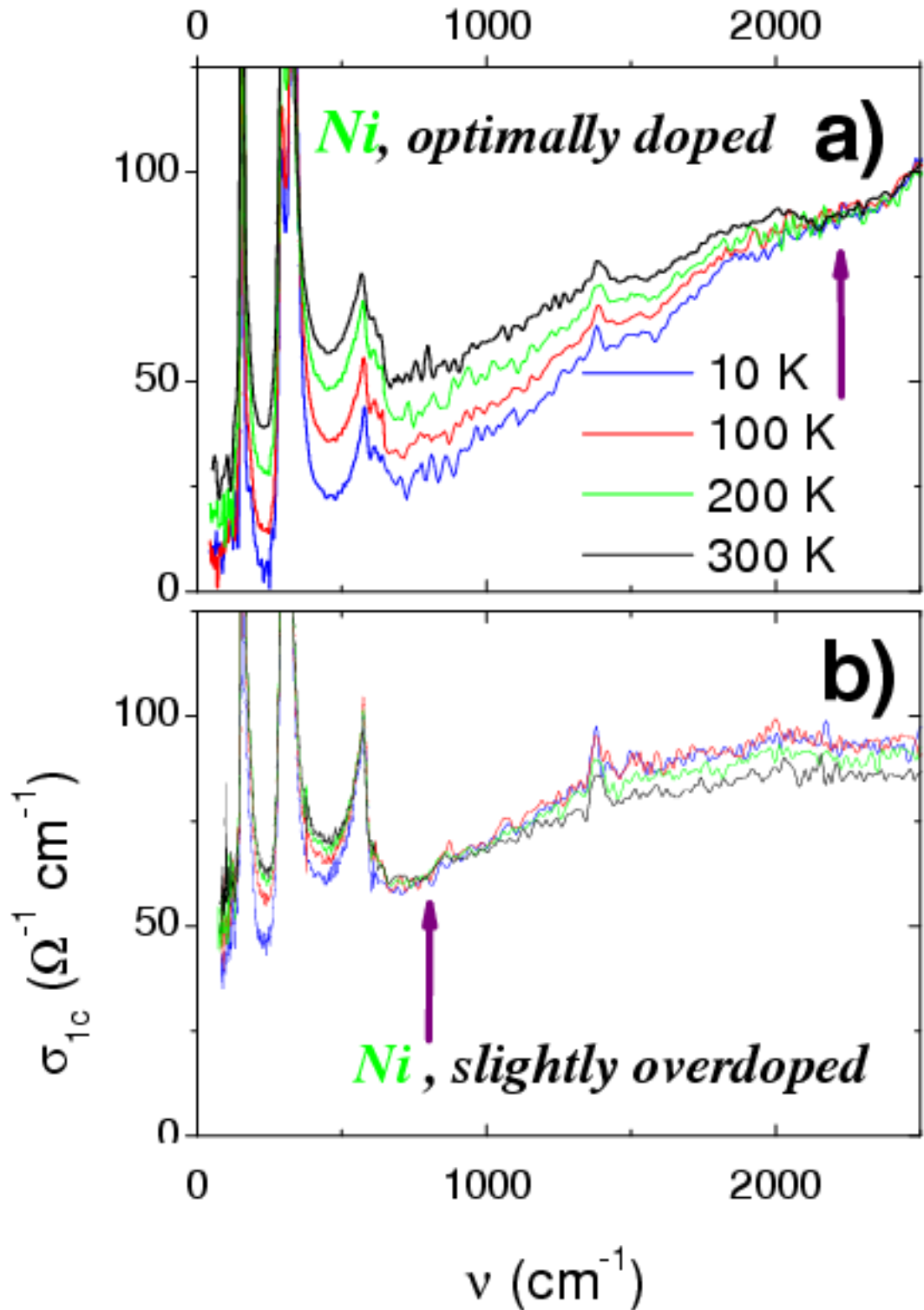


Figure 5.12: Conductivity of optimally doped non-superconductive  $\text{SmBa}_2\text{Cu}_{2.86}\text{Ni}_{0.14}\text{O}_7$  crystal, and slightly over-doped  $\text{SmCa}_{0.14}\text{Ba}_2\text{Cu}_{2.88}\text{Ni}_{0.12}\text{O}_7$  crystal with  $T_c = 25\text{K}$



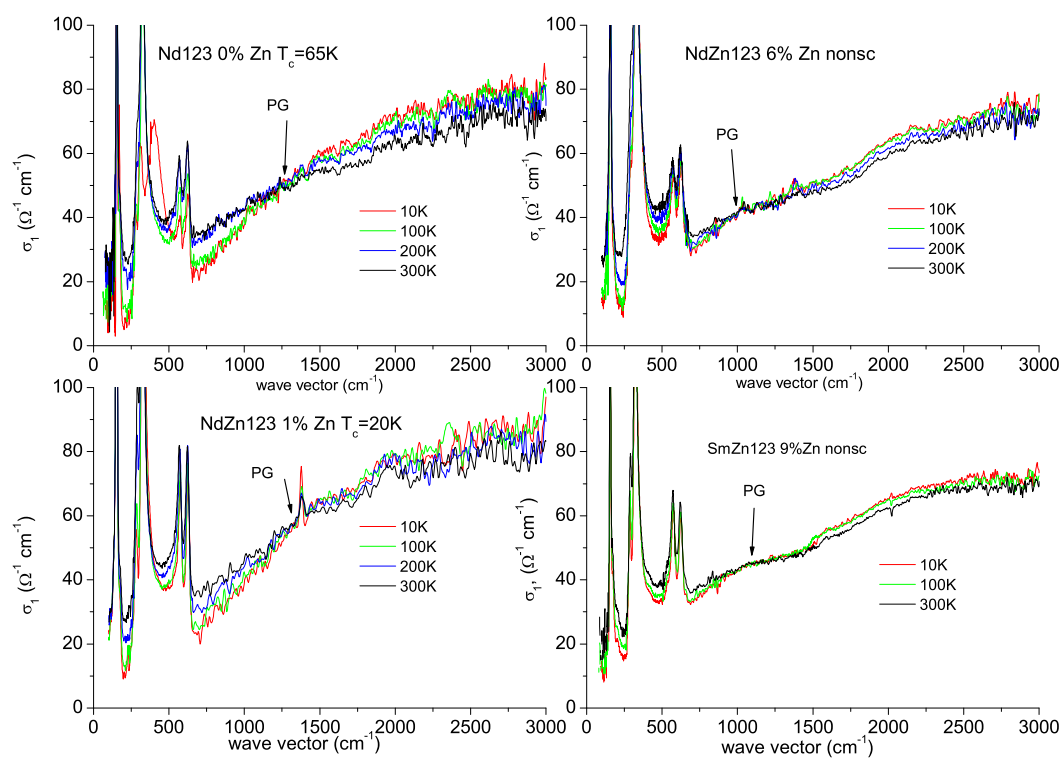


Figure 5.14: Infrared c-axis conductivity spectra of three underdoped  $\text{NdBa}_2\text{Cu}_{3-y}\text{Zn}_y\text{O}_{6.8}$  with 0, 1, 6% Zn and  $\text{SmZn}_{123}$  with 9% Zn

# Bibliography

- [1] P. Drude, Ann Phys. **32**, 584 (1887).
- [2] P. Drude, Ann Phys. **34**, 489 (1888).
- [3] L. Genzel, Far-Infrared FTS, in the book G.Grüner Millimeter and Submillimeter Wave Spectroscopy of Solids, Springer Verlag, Berlin (1998).
- [4] R.H. Norton, R. Beer, J.Opt.Soc.Am, **66**, 259 (1976).
- [5] Web page: <http://mathworld.wolfram.com/ApodizationFunction.html>
- [6] K.L. Barth, D. Böhme, et al., Thin Solid Films, **234**, 314 (1993).
- [7] R. M. A. Azzam and N. M. Bashara 1977 **Ellipsometry and polarized light**, (North Holland, Amsterdam).
- [8] A. Röseler 1990 **Infrared spectroscopic ellipsometry** (Academic-Verlag, Berlin).
- [9] Efficient polarizers for infrared ellipsometry, SPIE, Vol. 1746 Polarization analysis and Measurement (1992).
- [10] C. Bernhard, Habilitation thesis, University of Stuttgart (2002).
- [11] J. Humlíček, C.Bernhard, Thin Solid Film, **455-456**, 177 (2004)
- [12] D. van der Marel, Phys. Rev. B **60**, R765 (1999).
- [13] M. Thinkham, in Introduction to Superconductivity, (McGraw-Hill, New York, 1996).
- [14] M.A. Biondi and M.P. Garfunkel, Phys. Rev. Lett. **2**, 143 (1959).

- [15] J. Nam, R.A. Hughes, A. Dabkowski, and J.S. Preston, *Appl. Phys. Lett.* **82**, 3728. (2003).
- [16] Th. Wolf, V.N. Voronkova and P. Schweiss. *Phys. C* **341348**, 515 (2000).
- [17] C.T. Lin, W. Zhou, W.Y. Liang, et al., *Physica C* **195**, 291 (1992).
- [18] M Vojta, Habilitation thesis, University of Augsburg (2002).
- [19] D.J. Scalapino, *Phys. Rep.* **250**, 329 (1995).
- [20] J.M. Tranquada, J.D. Axe, N. Ichikawa et al., *Phys Rev B* **54**, 7489 (1996).
- [21] A. Mourachkine, *Supercond. Sci. Tech.* **13**, 1378 (2000).
- [22] A.M. Gabovich, *Physics Reports* **367**, 583 (2002).
- [23] J. Orenstein, et al. *Phys. Rev. B.* **42**, 6342 (1990).
- [24] N.L. Wang, S.J. Tajima et.al, *Phys. Rev. B.* **59**, 1953 (1998).
- [25] D.B. Tanner, T. Timusk in "Physical properties of High Temperature Superconductors II", 363, ed. D.M. Ginsberg, (World Scientific, Singapore, 1992).
- [26] D.B. Tanner, T. Timusk "Optical properties of High Temperature Superconductors" in "Physical properties of High Temperature Superconductors II", ed. D.M. Ginsberg, (World Scientific, Singapore, 1992).
- [27] K. Kamaras, S.L. Herr, C.D. Porter, et al., *Phys. Rev. Lett.* **64**, 84 (1990).
- [28] Stojkovic, and D. Pines, *Phys. Rev. B* **56**, 11931 (1997).
- [29] J.C. Phillips, *Philosophical Magazine B* **82**, 1703 (2002).
- [30] A.V. Boris et. al., *Science* **304**, 708 (2004).
- [31] D. Munzar et al., *Phys. Rev. B* **64**, 024523-1 (2001).
- [32] D. van der Marel, A. Tsvetkov, *Czech. J. Phys.* **46**, 3165 (1996). or cond-mat/0102411.
- [33] D. Munzar private correspondence.

- [34] D.J. Scalapino et al. Phys. Rev. Lett. **68**, 2830 (1992).
- [35] A.V.Boris et al., Phys. Rev. Lett. **89**, 277001-1 (2002).
- [36] Li Yu, Master thesis, University of Stuttgart (2004).
- [37] M.R. Norman et al., Phys. Rev. B **57**, 11093 (1998).
- [38] J.W. Loram et al., J. Phys. Chem. Solids **62**, 59 (2001).
- [39] J.W. Loram et al., Phys. Rev. Lett. **71**, 1740 (1993).
- [40] N. Miyakawa et al., Phys. Rev. Lett. **80**, 157 (1998).
- [41] W.A. Atkinson, Phys. Rev. B **59**, 3377 (1999).
- [42] T. Timusk, B. Statt, Rep. Prog. Phys. **62**, 61 (1999).
- [43] C. Dahnken cond-mat/0109036
- [44] J.C. Campuzano, et al., Phys. Rev. Lett. **64** (1990).
- [45] J. Yu, S. Massida, et al., Phys. Lett. A **122**, 203 (1987).
- [46] A. Damascelli et al., J. of Electron Spectr. and Related Phenomena **117118**, 165 (2001).
- [47] T. Takahashi et al, J. of Phys. and Chem. of Solids, **62**, 41 (2001).
- [48] V. Hankevych, cond-mat/0407085 (2004).
- [49] M. Vershinin et at., Science **303**, 1995 (2004).
- [50] Y. Itoh, S. Adachi, et al., Phys. Rev. B **66**, 134511 (2002).
- [51] Th. Wolf, private communication.
- [52] T. Katsufuji, T. Tanabe, et al., Phys. Rev. B **54**, 14230 (1996).
- [53] C.H. Chen, S.W. Cheong, A.S. Copper, Phys. Rev. Lett. **71**, 2461 (1993).
- [54] D. Knight, Phys. Rev. **76**, 1259 (1949).
- [55] Sheffield Hallam University, Division of Chemistry Homepage:  
<http://www.shu.ac.uk/schools/sci/chem/tutorials/molspec/nmr3.htm>

- [56] H. Gunther, Modern pulse methods in high resolution NMR spectroscopy.
- [57] G. Deutscher, Nature **397**, 410 (1999).
- [58] H. Alloul, et al., Phys. Rev. Lett. **63**, 1700 (1989).
- [59] R.E. Walstedt, W.W. Waren, Phys. Rev. B **41**, 9574 (1990).
- [60] M. Takigawa et al., Phys. Rev. B **43**, 247 (1991).
- [61] K. Ishida et al., Phys. Rev. B **58**, R5960 (1998).
- [62] D.N. Basov, T. Timusk, Phys. Rev. B **50**, 3511 (1994).
- [63] D. Pines, Physica C, **282-287**, 273 (1997).
- [64] V.J. Emery and S.A. Kivelson, Nature, **374** 434-437 (1995).
- [65] J. Corson et al., Nature **398**, 221 (1999).
- [66] S Sachdev, Quantum phase transitions, Physics World, April (1999).
- [67] C.M. Varma, Phys. Rev. B, **55**, 14554 (1997).
- [68] G. Blumberg et al., Science, **278**, 1427 (1997).
- [69] C.V. Raman, Ind. J. Phys., **2**, 387 (1928).
- [70] Ch. Renner, B. Revaz, et al., Phys. Rev. Lett. **80**, 3606 (1998).
- [71] Theory of defects in Solids, Clarendon Press, Oxford (1975).
- [72] Yu.A. Izyumov and M.V. Medvedev, Magnetically ordered crystals containing impurities (1973).
- [73] P.W. Anderson, J. Phys. Chem. Solids **11**, 26 (1959).
- [74] A.A. Abrikosov, L.P. Gor'kov, JETP **35**, 1558 (1958).
- [75] R.D. Parks, Magnetic Impurities, in P.R. Wallace, Superconductivity, **2** (1969).
- [76] Davis, Materials today, 24 (April 2002).
- [77] J.E. Hoffman, PhD thesis, University of California (2003).

- [78] V.M. Loktev, et al., Europhys. Lett., **60**, 757 (2002).
- [79] G.M. Zhang, Phys. Rev. Lett., **86**, 704 (2001).
- [80] I. Martin et. al., cond-mat/0012446 (2000).
- [81] M.E. Flotte, Phys. Rev. B, **61**, R14980 (2000).
- [82] A.V. Mahajan et. al., Eur. Phys. J. B, **13**, 457 (2000).
- [83] M.H. Julien et. al., Phys. Rev. Lett., **84**, 3422 (2000).
- [84] P. Mendels et. al., Europhys. Lett., **46**, 678 (1999).
- [85] J. Bobroff et. al., Phys. Rev. Lett., **78**, 2117 (1997).
- [86] Y. Itoh, J. Phys. Soc. Jap., **70**, 1881 (2001).
- [87] C. Bernhard, Phys. Rev. B, **58**, R8937 (1998).
- [88] B.Fisher et al., Phys. Rev. B, **48**, 16056 (1993).
- [89] M.K Yu, J.P. Franck, Phys. Rev. B, **48**, 13939 (1993).
- [90] T. Kawakami et. al., Jap. J. App. Phys., **26**, 2059 (1987).
- [91] B. David, C. Williams, et al., "Transmission Electron Microscopy - A Text-book for Materials Science", Plenum Press New York, 1996
- [92] R.D. Barnard. Thermoelectricity in Metals and Alloys (Taylor & Francis, London: 1972).
- [93] G.U. Sumanasekera, L. Grigorian, and P.C. Eklund. Low-temperature thermoelectrical power measurements using analogue subtraction. Meas. Sci. Technol. 11, 273-277 (2000).
- [94] K. Segawa, Phys. Rev. Lett, **86**, 4910 (2001).
- [95] J.L. Tallon, G.V.M. Williams, N.E. Flower, C. Bernhard, Physica (Amsterdam), **282-287C**, 236 (1997).
- [96] <http://musr.org>

- [97] R. Kubo, T. Toyabe, A stochastic model for low field resonance and relaxation // Magnetic Resonance and Relaxation Ed. R.Blink: North-Holland, Amsterdam, 1967. P.810-819.
- [98] Ch. Niedermayer, et al. Phys. Rev. Lett. **80**, 3843 (1998).
- [99] H. Mertinho, A.A. Martin, cond-mat/0312032v1
- [100] G.W.M. Williams and J.L. Tallon, Phys. Rev. B. **61**, 4319 (2000).
- [101] C.C. Homes, T. Timusk, et.al., Phys. Rev. Lett. **71**, 1645 (1993).
- [102] A.V. Boris, D.Munzar, et. al., Phys. Rev. Lett. **89**, 277001-1 (2002).
- [103] T. Timusk, C.C. Homes cond. mat/0209371.
- [104] N. Jakubowicz et al., Phys. Rev. B **63**, 214511 (2001).
- [105] J. Prade et. al., Phys. Rev. B **39**, 2771 (1989).
- [106] M. Tinkham, Introduction to superconductivity, McGraw-Hill, New York, (1996), Chap. 3.9.3
- [107] D. Munzar et. al., Solid State Comm., **112**, 365 (1999).
- [108] B. Liang, C. Bernhard, Th. Wolf, et al., Supercond. Sci. Technol. **17**, 731-738 (2004).
- [109] H. Chen. Phys. Rev. Lett., **71**, 2304 (1993).
- [110] S.I. Schlachter, K.P. Weiss, et al. J. Low Temp. Physics. **117** (1999).
- [111] S. Adachi et al., Phys. Rev. B **61**, 4314 (2000).
- [112] Y. Itoh et al., Phys. Rev. B **66**, 134511 (2002).
- [113] M. Rauderia et. al, cond-mat/9710233 (1997).
- [114] B.A. Githevskii et al, cond-mat/0312009 (2003).
- [115] C. Howald et al, cond-mat/0201546 (2002).
- [116] M.G. Zacher, Phys. Rev. Lett. **85**, 2585 (2000).
- [117] M. Randeria, cond-mat/9710223 (1997).

- [118] M. Cyrot and D. Pavuna, "Introduction to Superconductivity in High  $T_c$  Materials", World Scientific, Singapore (1992).
- [119] P.A Lee, Physica C 317318 194204 (1999).
- [120] B. Farnworth, T. Timusk, Phys. Rev. B, **10**, 2799 (1974).
- [121] B. Farnworth, T. Timusk, Phys. Rev. B, **14**, 5119 (1976).
- [122] M.R. Presland, J.L. Tallon et al., Physica C **176**, 95 (1991).
- [123] J.L. Tallon, et al., Physica C, **185-189**, 855 (1991).
- [124] H. Zhang et al., Phys. Rev. Lett. **70**, 1697 (1993).
- [125] S.D. Obertelli and J.R. Copper J.L. Tallon, Phys. Rev. B, **44**, 45 (1992).
- [126] Ch. Niedermayer, C. Bernhard, T. Blasius et. al., Phys. Rev. Lett. **80** (1998).
- [127] T. Adachi, S. Yairi, et. al., Phys. Rev. B **69**, 224517 (2004).
- [128] C.Bernhard et al, Phys. Rev. B **59**, 6631 (1999).
- [129] J.L. Tallon et al., Phys. Stat. Solidi **215**, 531 (1999).
- [130] C. Bernhard, J. Humlichek, B. Keimer, Thin Solid Films, **455-456**, 143 (2004).
- [131] J. Humlichek, C. Bernhard, Thin Solid Films, **455-456**, 177 (2004).
- [132] A.V. Chubukov, and J. Schmalian, Phys. Rev. B, **57**, 11085 (1998).
- [133] T. Dahm, D. Manske, and L. Tewordt, Phys. Rev. B, **56**, 11419 (1997).
- [134] P.A. Lee, and X.G. Wen, Phys. Rev. Lett. **76**, 503 (1996).
- [135] U. Löw et. al., Phys. Rev. Lett. **72**, 1918 (1994).
- [136] V.J. Emery, S.A. Kivelson, O. Zachar, Phys. Rev. B **56**, 6120 (1997).
- [137] H.F. Fong et.al., Phys. Rev. Lett. **82**, 1939 (1999).



# Acknowledgements

I am very grateful to...

...Privatdozent Dr. Christian Bernhard, for transferring me his knowledge and expertise in ellipsometry, for his contribution in the work presented in this thesis, for careful reading of the thesis, for discussions and for answering all my questions.

...Dr. Alexander Boris, for his contribution in the work presented in the thesis, for his help in resolving many technical problems during experiments, for useful discussions of different aspects of optical spectroscopy, and for close collaboration.

...Prof. Dr. Bernhard Keimer, for letting me join his department, for supervising me during my work, and for careful reading the thesis.

...Prof. Dr. D. Munzar, for discussions of different aspects of his model.

...Dr. Thomas Wolf for growing crystals which were measured during my experiments.

...Prof. Dr. Clemens Bechinger, for accepting the task reviewing the thesis.

...Yu Li for his help and collaboration in the experiments.

...Engineers Dietrich Böhme, Heiko Uhlig for their job and help in improving and repairing our experimental equipment.

...Dr. Y.L. Mathis, Dr. B. Gasharova, Dr. D. Moss for their help at ANKA Synchrotron source in Karlsruhe.

...all other people who made a contribution in this work Prof. J.L. Tallon, V. Hinkov, A. Golnik, and others whom I might forget to mention here. I am also grateful to all members of Keimer's Department for friendly atmosphere during my work.

# Copyrights and terms of use

(c)Alexei Pimenov, 2005. All rights reserved. The text and the images included in the thesis are for your viewing and enjoyment, but this does not grant you the license to use them in any way you choose. If you want to use a figure or a part of the text which are included in the thesis from an external source the reference to the original first source should be provided.

The use of the thesis and it's parts in the projects aimed at obtaining a commercial profit is prohibited without special authorization from the author.

## **CURRICULUM VITAE**

### **ALEXEI PIMENOV**

April 26<sup>th</sup>, 1978                      born in Sholkovo, Russia

1984-1995                              Sholkovo High School

1995-2001                              Lomonosov Moscow State University

Specialization:                      radiophysics  
Profession:                              physicist  
Master thesis:                      Ultra narrow parametric solitons, Grade A  
Area of specialization:              Nonlinear optics, solitons, programming, and simulations

2001-2005                              Max Planck Institute for Solid State Research  
Ph.D. student

Area of specialization:              Ellipsometry, high temperature superconductors

## **INTERNATIONAL CONFERENCES**

Modern Trends in Computational Physics	July, 2000	Russia
NATO ASI "Soliton Driven Photonics"	October, 2000	Poland
OSA NLGW'01 Topical Meeting	March, 2001	US
Low Energy Electrodynamics in Solids	July, 2004	Germany

## PUBLICATION LIST

9. A.V. Pimenov, A.P. Sukhorukov, "Spatial parametric solitons of small width," Bull. RAS, Phys. 64, 2349-2354 (2000).
10. A.V. Pimenov, A.P. Sukhorukov, L. Torner, "Ultra-narrow optical beams in quadratic nonlinear media," JETP Letters, 72, 495-498 (2000).
11. A.V. Boris, D. Munzar, N.N. Kovaleva, B. Liang, C.T. Lin, A. Dubroka, A.V. Pimenov, T. Holden, B. Keimer, Y.L. Mathis, C. Bernhard, "Josephson plasma resonance and phonon anomalies in trilayer  $\text{Bi}_2\text{Sr}_2\text{Ca}_2\text{Cu}_3\text{O}_{10}$ ," Phys. Rev. Letters, 89, 27001 (2002).
12. A.V. Boris, D. Munzar, N.N. Kovaleva, B. Liang, C.T. Lin, A. Dubroka, A.V. Pimenov, T. Holden, B. Keimer, Y.L. Mathis, C. Bernhard, "Superconductivity induced electronic excitations and phonon anomalies in trilayer  $\text{Bi}_2\text{Sr}_2\text{Ca}_2\text{Cu}_3\text{O}_{10}$ ," NSLS Science Highlights (2003).
13. A. Lebon, P. Adler, C. Bernhard, A. Boris, A.V. Pimenov, A. Malijuk, C.T. Lin, C. Ulrich, B. Keimer, "Magnetism, charge order and giant magnetoresistance in  $\text{SrFeO}_{3-d}$  single crystals," Phys. Rev. Letters, 92, 037202 (2004).
14. C. Bernhard, T. Holden, A.V. Boris, N.N. Kovaleva, A.V. Pimenov, J. Humlicek, C. Ulrich, C.T. Lin, J.L. Tallon, "Anomalous oxygen isotope effect on the in-plane FIR conductivity of detwinned  $\text{YBa}_2\text{Cu}_3\text{O}^{16,18}_{6.9}$ ," Phys. Rev. B, 69, 052502 (2004).
15. T. Holden, H.U. Habermayer, G. Christiany, A. Golnik, A. Boris, A.V. Pimenov, J. Humlicek, O. Lebedev, G. van Tendeloo, B. Keimer, C. Bernhard, "Proximity induced metal/insulator transition in  $\text{YBa}_2\text{Cu}_3\text{O}_7/\text{La}_{2/3}\text{Ca}_{1/3}\text{MnO}_3$  superlattices," Phys. Rev. B, 69, 064505 (2004).
16. C. Bernhard, A.V. Boris, N.N. Kovaleva, G. Khaliulin, A.V. Pimenov, L. Yu, D.P. Chen, C.T. Lin, B. Keimer, "Charge-ordering and magnetic polarons in  $\text{Na}_{0.82}\text{CoO}_2$ ," Phys. Rev. Letters, 93, 167003 (2004).
17. A.V. Pimenov, A.V. Boris, L. Yu, V. Hinkov, T. Wolf, J.L. Tallon, B. Keimer, C. Bernhard, "Ni impurity induced enhancement of the pseudogap in cuprate high  $T_c$  superconductors," Phys. Rev. Letters, 94, 227003 (2005).